PhD program in Computational and Applied Physics

STUDY OF RELAXATION PHENOMENA AND LOCAL STRUCTURE EVOLUTION IN METALLIC GLASSES BY MEANS OF MOSSBAUER AND MECHANICAL SPECTROSCOPY

Doctoral thesis by: Seyedeh Leila Panahi

Thesis advisors: Pere Bruna and Eloi Pineda

Department of Physics, Institute of Energy Technologies

Universitat Politècnica de Catalunya

Barcelona, December 2022

This thesis is dedicated to my mum.

Thank you for always believing in me.

Acknowledgments

I want to start by saying how grateful I am to all people, my heroes, who have given me so much of their time, love and energy and supported me during my Ph.D. studies.

I'd like to express my deep and sincere gratitude to my supervisors, Dr. Pere Bruna and Dr. Eloi Pineda, for their encouragement, guidance and support throughout the duration of this study and opportunity that provide for me to learn more and progress more. I would like to express my special thanks to Dr. Pere Bruna for supporting me to apply for scholarship and always be available for consult during experiment and after experiment for analyzing the data.

In addition, I'd like to thank to Professor Daniel Crespo, The Rector of university who offer me so much of help and good advice during this Ph.D. and experiments. He always followed my activities with enormous patience. I'm so grateful to have opportunity to learn hard working attitude, positive energy and being humble and helper beside of all brilliant knowledge that he has in research, his brilliant way for solving problem is always inspiring me to never give up in any point of life. Also, I would like to thank professor Trinitat Pradell who teachs me how prepare samples for Nanoindentation and other measurements. I want to thank Dr. Trifon Trifonov from Center de Recerca en Nanoenginyeria for X-ray Diffraction and SEM and XPS, Special thanks go to thank Dr. Jordi Sort and Dr. Jordina Fornell from Universitat Autonomia de Barcelona (UAB) for their help and guidance for nano-indentation test.

Im grateful for all brilliant people: Chenyang, Georgy, Mehran, Mahin, Neda, Lucy and David in our office for their friendship, support and kindness. Finally, My deepest gratitude goes to my family without whom I couldn't have achieve my goals, Thank you mum for all your patient, support, and kindness and for seeing ability inside me and let me to show it, for encourage me to be brave and fighter and don't be afraid to take new risk and challenge, I hope you see all and you know all is because of you, I would like to express my eternal love to My Dad , My dearest sister Sami and my affectionate brother Hamed, my partner Anxo Thank you for all support , energy, love and care ,without you it's impossible finish this journey.

Table of Contents

List of figures

temperature T (y axis). Right panel: diffractograms of selected temperatures, from the initial amorphous phase to the highest temperature with phase identification.

Figure 3.9 Crystallization of the AB15Si5 sample ($\eta = 1/3$). Left panel: 2D map of the crystalline peaks showing their intensity (in a color scale) versus the diffraction angle 2θ (x axis) and the temperature T (y axis). Right panel: diffractograms of selected temperatures from the initial amorphous phase to the highest temperature with phase identification.

Figure 3.10 Crystallization of the AB10Si10 sample ($\eta = 1$). Left panel: 2D map of the crystalline peaks showing their intensity (in a color scale) versus the diffraction angle 2θ (x axis) and the temperature T (y axis). Right panel: diffractograms of selected temperatures from the initial amorphous phase to the highest temperature with phase identification.

Figure 3.11 Crystallization of the AB10Si15 sample ($\eta = 3/2$) . Left panel: 2D map of the crystalline peaks showing their intensity (in a color scale) versus the diffraction angle 2θ (x axis) and the temperature T (y axis). Right panel: diffractograms of selected times after reaching the maximum temperature in the hot stage.

Figure 3.12 Crystallization of the AB10Si20 sample ($\eta = 2$). Left panel: 2D map of the crystalline peaks showing their intensity (in a color scale) versus the diffraction angle 2θ (x axis) and the temperature T (y axis). Right panel: diffractograms of selected temperatures from the initial partially crystalline phase to the highest temperature with phase identification.

Figure 3.13 Experimental Mössbauer spectra (blue dots) and their fits (red lines) for the $(FeCoCrNi)_{80}B_{20}$ alloy at six different representative stages of the crystallization process. In colored lines there are the sub-spectra fitted for the different phases (purple for the amorphous phase, blue and cyan for the FCC phase and orange and dark red for the borides). The insets show the distribution of quadrupole splittings (for the as-quenched samples) or hyperfine magnetic fields (for the annealed ones) needed for the fitting.

Figure 3.14 Mössbauer spectrum of the as-quenched FeCoCrNi HEA in ribbon form (blue dots) together with the best fitting (red line) to the experimental data. The inset shows the distribution of quadrupole splittings.

Figure 3.15 Variation of the at% (with an error of ±0.5 %, smaller than the symbol) of the different phases of the $(FeCoCrNi)_{80}B_{20}$ alloy as a function of the annealed temperature calculated from the analysis of the Mössbauer spectra. The inset shows in blue (red) the atomic percentage of the total paramagnetic (ferromagnetic) phases as a function of the annealed temperature.

Figure 3.16 Experimental Mössbauer spectra (blue dots) and their fits (red lines) for the $(FeCoCrNi)_{80}B_{10}Si_{10}$ alloy at all the stages of the crystallization process except the fully crystalline one. In colored lines there are the sub-spectra fitted for the different phases (purple for the amorphous phase, blue and cyan for the FCC phase and orange and dark red for the BCC and borides). The insets show the distribution of quadrupole splittings (from 673 to 773K) or hyperfine magnetic fields (from 823 to 923 K) needed for the fitting.

Figure 3.17 Variation of the at% (with an error of ±0.5 %, smaller than the symbol) of the different phases of the $(FeCoCrNi)_{80}B_{10}Si_{10}$ alloy as a function of the annealed temperature calculated from the analysis of the Mössbauer spectra. The inset shows in blue (red) the atomic percentage of the total paramagnetic (ferromagnetic) phases as a function of the annealed temperature.

Figure 3.18 SEM images of the HEMGs alloys $(FeCoCrNi)_{80}B_{20}$ (left column) and $(FeCoCrNi)_{80}B_{10}Si_{10}$ (right column) in their as-quenched state (first row) and after annealing at 823, 873 and 973 K.

Figure 3.19 Distribution of grain sizes in $(FeCoCrNi)_{80}B_{20}$ (top) and $(FeCoCrNi)_{80}B_{10}Si_{10}$ (bottom) after annealing at different temperatures.

Figure 4.1 Load-displacement of nanoindentation curves (left) and variation of hardness (H) and reduced Young's modulus (E_r) (right) for as quenched ribbons at room temperature.

Figure 4.2 Comparison of Young modulus and hardness for several compositions. The circle indicates the compositions investigated in this study.

Figure 4.3 Variation of hardness (H) and reduced elastic modulus (E_r) as a function of annealing temperature for AB20 (left) and AB10Si10 (right).

List of tables

List of academic publications, activities and grants

Grants:

- ➢ PhD grant: FI AGAUR (2018FI-B-00502), Duration (1May 2018- 30April 2021).

- ➢ PhD grant extension: Becas Santander PIF 2n semestre 2021 – UPC.

Publications:

- ➢ **Panahi, S.L.**, Fornell, J., Popescu, C., Pineda, E., Sort, J., Bruna, P., 2022. *Structure, mechanical properties and nanocrystallization of (FeCoCrNi)-(B,Si) high-entropy metallic glasses*. Intermetallics 141, 107432. doi:10.1016/j.intermet.2021.107432.

- ➢ **Panahi, S.L.**, Ramasamy, P., Masdeu, F., Stoica, M., Torrens-Serra, J., Bruna, P., 2021. *Evaluation of the Effect of Minor Additions in the Crystallization Path of [(Fe0.5Co0.5)0.75B0.2Si0.05]100-xMx Metallic Glasses by Means of Mössbauer Spectroscopy*. Metals 11, 1293.. doi:10.3390/met11081293.

- ➢ **Panahi, S.L.**, Garcia-Ramón, M., Pineda, E., Bruna, P., 2020. *New (FeCoCrNi)-(B,Si) high-entropy metallic glasses, study of the crystallization processes by X-ray diffraction and Mössbauer spectroscopy*. Journal of Non-Crystalline Solids 547, 120301.. doi:10.1016/j.jnoncrysol.2020.120301.

- ➢ **Panahi, S.L.**; Bruna, P.; Pineda, E. *Effect of Si and B on the Electrochemical Behavior of FeCoNiCr-Based High-Entropy Amorphous Alloys*. Materials 2022, 15, 8897. https://doi.org/10.3390/ ma15248897

International conferences:

- ➢ Oral Presentation in ISMANAM 2018 Rome, Italy: *On the crystallization of a new high-entropy metallic glass studied by Mössbauer spectroscopy*

- ➢ Oral Presentation in EUROMAT 2019 Stockholm, Sweden: *Influence of the alloying element on structural, mechanical, thermal and magnetic properties of a new iron base high-entropy metallic glasses*

- ➢ Oral Presentation in HERCULES European School, March 2020, Grenoble, France: *Study of new high entropy metal glasses*

Other activities:

- ➢ Hercules European Research Course for Users of Large Experimental Systems. Full-time participant (100 hours of lectures and 18 hours tutorials) Grenoble, France.

- ➢ Participation in synchrotron experiment: *Disorder induced resonance in metallic glasses*. DIAMOND, proposal ID: SM18772-1, Spring 2018, Harwell Campus, Oxfordshire.

- ➢ Participation in synchrotron experiment: *Investigation of the glass forming ability and in-situ crystallization of a novel family of high-entropy metallic glasses*. ALBA, proposal ID: 2018022691, Autumn 2018, Cerdanyola del Vallès.

- ➢ Participation in synchrotron experiment: *Low temperature measurement of disordered induced ressonance in metallic glasses*. ALBA, proposal ID: 2019023301, Autumn 2019, Cerdanyola del Vallès.

CHAPTER 1. INTRODUCTION

From ancient times metals have been attractive objects for humankind and with the progress of science the need for using metals for different applications have increased drastically. For many years, researchers used traditional approaches for the discovery of new materials based on slow trial and error techniques. In this traditional way, scientists chose the elements and their proportion randomly, followed the process of production and finally tested the material to observe their properties. They checked if the material properties could be useful for any particular application, otherwise the process started from the beginning but changing the constituent elements or their percentage. In modern times, scientists tried various methods to improve the efficiency of metals and one of the best and more recent examples of this is the advent of the so-called Metallic Glasses (MGs). Metallic glasses are metallic alloys with a disordered structure that are produced when the metallic liquid is rapidly quenched to solid state bypassing crystallization. Thus, the atoms have a local disordered atomic packaging and a lack of the main features of crystalline materials such as atomic planes, crystalline directions, grain boundaries and crystalline defects [1][2]. MGs can be used in plenty of applications such as soft (e.g. transformer core laminations) or hard magnetic materials, wear-resistant light alloys, materials with enhanced catalytic performance for fuel-cell applications and new alloys for medical implants and dental amalgams [3].

On the other side, in the last decades, some groups have focused their research on a new family of alloys which are called high entropy alloys (HEAs). These alloys are attractive because of their unique composition, microstructure and adjustable properties. HEAs contain more than 5 main elements in equal or near equal atomic percentage (at%) and the atomic fraction of each component is greater than 5 at%. Thus, in a multicomponent phase diagram, HEAs are situated in the center of the diagram (see figure 1.1).
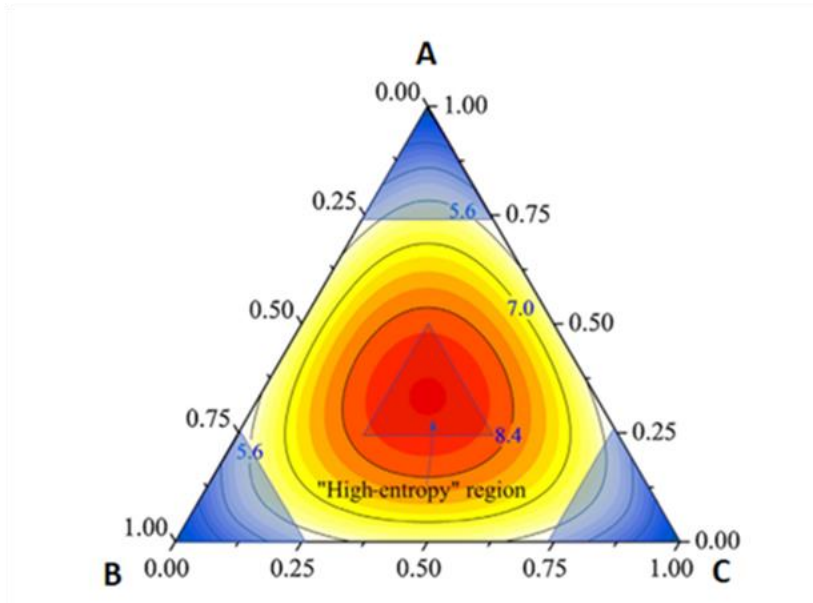
Figure 1.1 Schematic ternary alloy system where the blue corner region indicate the conventional alloys based on one or two principal elements whereas the red center region indicates the 'high-entropy' region (taken from [4]).

Besides of that, if we consider the number of elements which are used for the new alloys we can see that there are some elements which are normally used frequently while there are others scarcely used because of the difficulty during their processing, high prices, toxicity, etc. For high entropy alloys normally five or more principal elements are used and this creates the opportunity to use new elements from the periodic table and to investigate their new properties for different applications.

1.1. Metallic Glasses

Metallic glasses were produced for the first time by Professor Pol Duwez in 1960 in the California Institute of Technology at Pasadena. He synthesized the $Au_{75}Si_{25}$ alloy by rapid solidification [1]. After that, hundreds and thousands of alloys with different compositions have been produced as metallic glasses. In the early 1990s metal-metal systems such as La-, Mg-, and Zr- based alloys were prepared by quenching from the supercooled liquid. The main difference between metallic glasses and normal metallic materials is that metallic materials are crystalline in their nature and the constituent elements are arranged in a periodic manner, while metallic glasses have a disordered atomic structure which is produced by rapid solidification from the liquid state. In many cases the cooling rate is very fast, between 10^5 - 10^6 K s^{-1}. These high cooling rates are needed because metallic melts have a high tendency to crystallize and, therefore, high cooling rates are required to prevent crystallization. If the resultant alloy is fully

amorphous it is characterized by a broad diffuse halo in an X-ray diffraction pattern, instead of the showing the Bragg peaks associated to crystalline planes. In most of the cases, glassy alloys can be produced only as thin ribbons, wires or sheets. However, in 1995, the first Fe-based bulk metallic glasses (BMGs) were successfully developed in the Fe-Al-Ga-P-C-B compositional system [2]. BMGs are non-crystalline metallic alloys that can be produced with lower cooling rates than conventional MGs, between 10 and 100 K s^{-1} depending on the composition of the alloy. Therefore, it is possible to produce BMGs that are several centimeters thick as the cooling rate is inversely proportional to the diameter of the resultant ingot. To obtain a supercooled metallic liquid with enough glass-forming ability (GFA) to form a BMG there are three empirical rules which are known as Inoue's rules [5]: (1) the multicomponent system should consist of three or more elements; (2) there should be a significant difference between the atomic size of such constituent elements (>12%) and (3) the elements should have a negative heat of mixing between them.

During the last 20 years a large variety of metallic glass-forming compositions have been discovered and they can be classified into two big groups: metal-metal and metal-metalloid types [3] Metal-metalloid type contains around 80% of metal atoms and 20% of metalloid atoms (B, C, P, and Si). The metallic content can be of different types of metallic atoms such as, for example, in the well-known cases of $Au_{80}Si_{20}$, $Fe_{80}B_{20}$, $Pd_{80}Si_{20}$, $Pd_{77}Cu_6Si_{17}$ or $Fe_{40}Ni_{40}B_{20}$. In the case of the metal-metal type, they just contain transition metals without any particular restriction regarding the atomic percentage of the elements, such as, for example, the $Fe_{90}Zr_{10}$, $Ni_{60}Nb_{40}$, $Mg_{70}Zn_{30}$ or $Cu_{57}Zr_{43}$ binary systems. In the present work we will take as a starting point a well-known alloy of the metal-metalloid type with 20 at% of B and 80 at% of Fe that shows good soft magnetic properties, high abrasive resistance, prominent corrosion resistance and high strength. However, these Fe-based metallic glasses have the limitation of a reduced critical diameter, few millimeters when produced as bulk amorphous alloys, because of their low GFA. Therefore, there is a limitation for the potential use of Fe-based metallic glasses in engineering applications and, nowadays their production is mostly in form of thin ribbons, wires and films [6]. The first Fe-based bulk metallic glass, Fe-(Al,Ga)-(P,C,B,Ge,Si), was produced in a shape of a rod with 1-2 mm diameter in 1995 [7]. The largest thickness achieved for Fe-based metallic glass is around 16 mm whereas Pd-based metallic glasses can reach several centimeters. In many cases, researchers tried to improve the GFA of Fe-based amorphous alloys and to produce bulk Fe-based metallic glasses by adding elements like Al, Mo, Nb, Ga and Y in amounts of 1-30 at%.

3

1.2. Glass forming ability

There are many different methods to produce metallic glasses, like rapid solidification, vapor deposition or electrodeposition. When an alloy is cooled down with sufficient cooling rate from the equilibrium liquid state, the metallic melt become undercooled and bypasses crystallization. However, each alloy has a different critical cooling rate and a parameter is required in order to characterize how easy is for a melt to become an amorphous solid upon cooling. The GFA is the ability of a melted alloy to solidify without crystallization in a completely amorphous structure. It can be estimated directly by the critical cooling rate (R_c), the minimum cooling rate which is required to completely suppress crystallization. R_c can be evaluated by using the Time-Temperature-Transformation (TTT) diagram. Figure 1.2 shows a schematic TTT diagram for a melted alloy which is cooled down from above the liquidus temperature (T_l) to below the glass transition temperature (T_g) with two different cooling rates. The glass transition temperature (T_g), is the temperature at which the transition from supercooled liquid to an amorphous solid takes place.
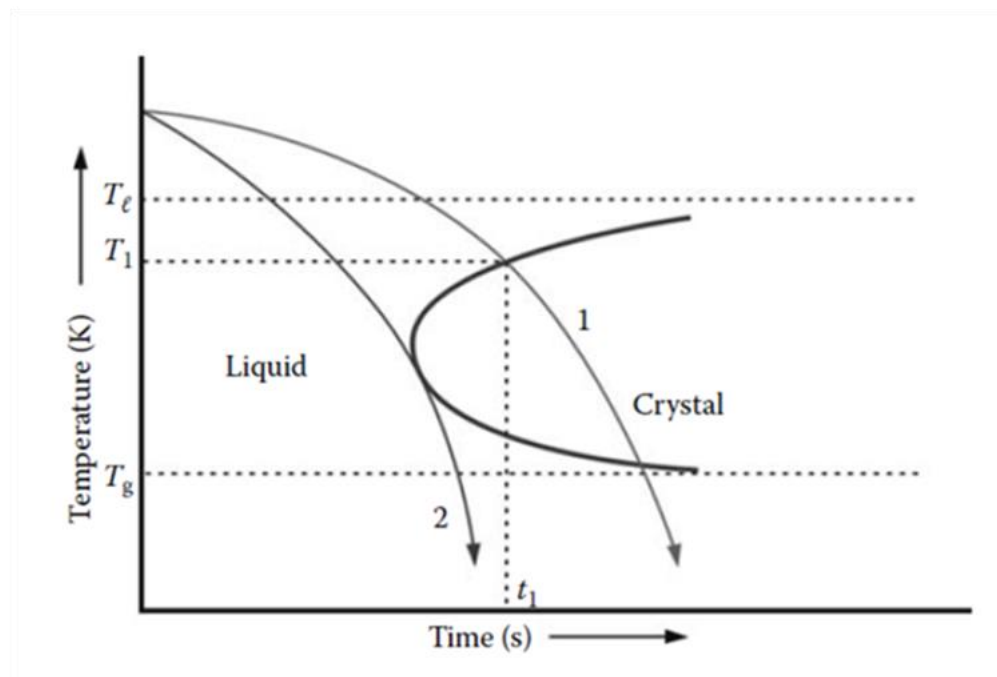
Figure 1.2 Schematic time-temperature-transformation (TTT) diagram (taken from ref. [3]).

According to curve (2) in Figure 1.2, a glass can be produced if the cooling process is fast enough to avoid the crystallization of the melt. However, if the cooling is slower, like the one indicated with curve (1) in the figure, the result will be a crystalline solid. The glass forming

ability of a melt is in direct relation with the maximum thickness (t_{max}) in which the alloy can be produced, being this thickness larger when the GFA is higher.

1.2.1. Parameters to describe the glass forming ability

There are several parameters that can be used to describe and characterize the glass forming ability of metallic glasses, being the supercooled liquid region and the reduced glass transition temperature the most used ones.

A) Supercooled liquid region (ΔT_x)

As the temperature of a molten alloy decreases, the specific volume and the enthalpy also decrease becoming more and more viscous until it forms a glass. By convention, it is considered that a glass is formed when the viscosity reaches a value of 10^{12} Pa s, therefore this region is considered as the glass transition region. Figure 1.3 shows the change in volume with temperature and the glass transition temperature. The value of T_g is usually determined upon heating by means of a differential scanning calorimetry (DSC) or differential thermal analysis (DTA) with heating rates of 10-20 K min^{-1} from the increase in the heat capacity of the alloy. A proper choice of the alloying system and its composition can reduce the critical cooling rate for glass formation. As a result, the thickness of the glass parts can increase from few micrometers (20-50 μm) in rapid solidification processes to few millimeters or few centimeters using conventional casting techniques [8].

According to Figure 1.3, in the heating process from a glassy state the alloy crosses different regions until reaching the melting point. The increase in temperature decreases the viscosity of the alloy and increases its volume until it reaches the glass transition temperature where the disordered material enters in the supercooled liquid region. A further increase in temperature leads to the melting point, T_m, above it the liquid is the stable thermodynamic phase. In the supercooled liquid region, the material can crystallize transforming to the stable thermodynamic ordered phase. As it can be observed in the figure there is not a uniquely defined T_g but rather a glass transition range of temperatures, since the transition from a glassy state to supercooled liquid depends on the kinetics. The region between T_g and the crystallization temperature (T_x) is known as the supercooled liquid region (SLR), $\Delta T_x = T_x - T_g$. ΔT_x is a parameter that indicates the thermal stability of the liquid phase and its resistance to crystallization. A larger value of ΔT_x means that the supercooled liquid can exist in a wide

5

temperature range without crystallization and that it has a high resistance to nucleation and growth of the crystalline phases [5].
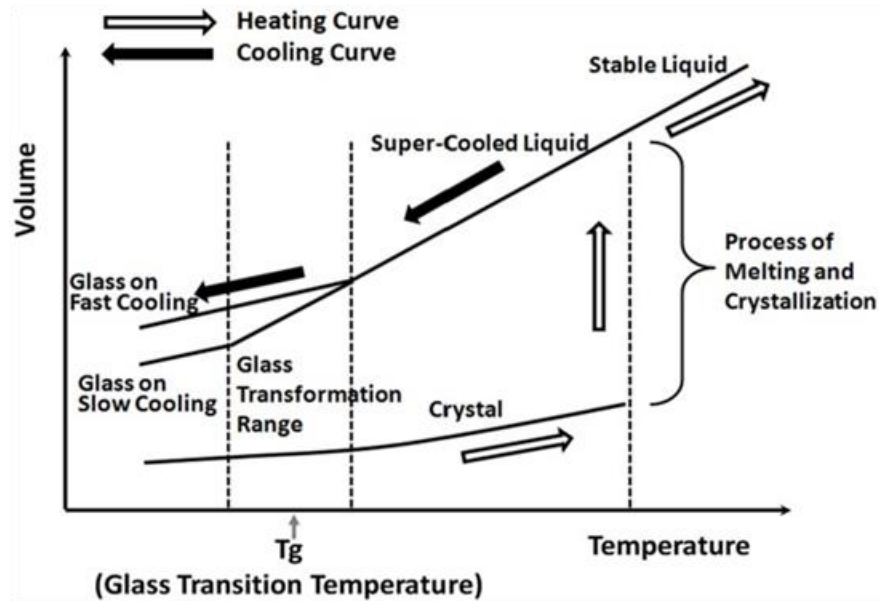
Figure 1.3 Change of volume of a molten alloy as a function of the temperature (taken from ref. [9]).

B) Reduced glass transition temperature (T_{rg})

In 1969 Turnbull, for the first time, used the reduced glass transition temperature (T_{rg}) as a parameter to assess the GFA of glass formers and now it has become widely used. The reduced glass transition temperature is defined as [10]

$$T_{rg} = \frac{T_g}{T_l} \tag{1.1}$$

where T_g is the glass transition temperature and T_l is the liquidus temperature of the alloy. Thus, the higher T_g and lower T_l, the higher the tendency to form glass and, therefore, a large value of T_{rg} means a high GFA. The GFA of a system is not just related to the cooling rate but it also depends on the alloy composition. The T_{rg} tends to be higher for large number of alloying elements and, therefore, it is more easy to produce glassy multicomponent alloys than simple binary or monoatomic systems [11].

1.3. High entropy alloys

For many years, researchers focused on the corner of the phase diagrams to develop new alloys. However, as illustrated in Figure 1.4, the shifting of the focus to the center of the diagram gave rise to the appearance of the so-called high-entropy alloys (HEAs).

6
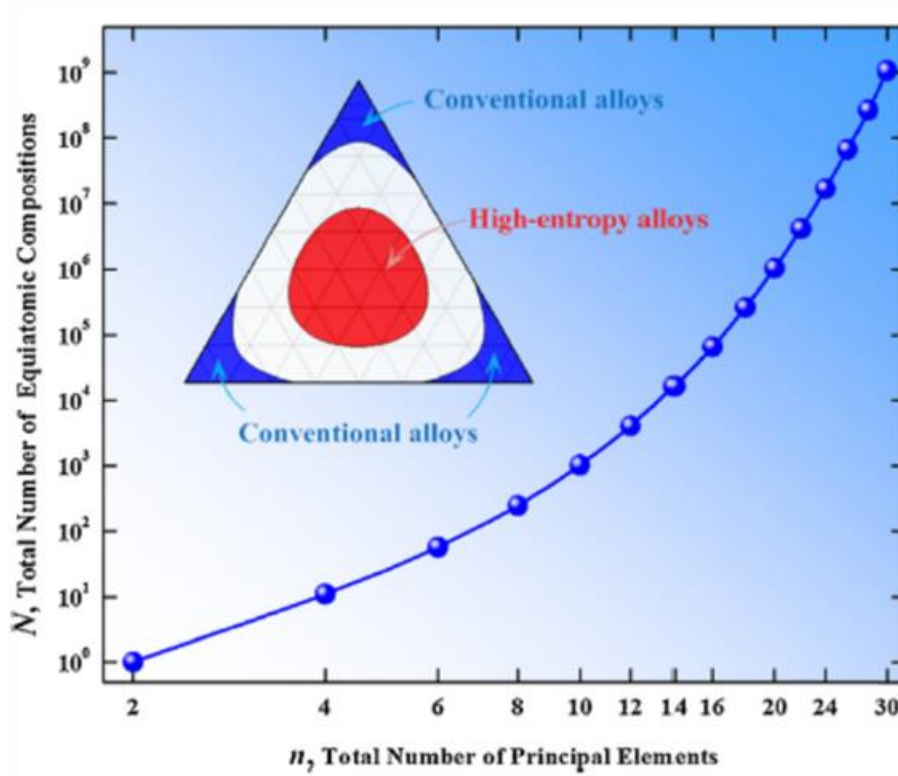
Figure 1.4 Number of equiatomic compositions as a function of the constituent elements together with a sketch of the location in a phase diagram of the high-entropy and conventional alloys (taken from ref. [4]).

High entropy alloys were for the first time introduced by Jien-Wei Yeh and coworkers. They defined them as multicomponent solid solution alloys that contain more than five constituent elements in equiatomic, or close to equiatomic, ratios. Such condition increases the configurational entropy of mixing by an amount enough to overcome the enthalpies of compound formation [12]. The configurational entropy, S, of a random mix of N elements is defined by the following equation

$$\Delta S = -R \sum_{1}^{N} x_i \ln x_i \tag{1.2}$$

where R is the gas constant, x_i is the mole fraction of the element i in the alloy and $\sum_{1}^{N} x_i = 1$. Also, the entropy of mixing for N elements is

$$\Delta S_m = R \ln N \tag{1.3}$$

According to equation (1.3) by increasing the number of alloying elements the entropy of mixing increases quickly. High entropy alloys can form crystalline structures like simple, single phase solid solutions with different crystallographic arrangements, e.g., face centered cubic (FCC), body centered cubic (BCC) or hexagonal close-packed (HCP) and in some cases can

be also arranged in an amorphous structure forming the so-called high-entropy metallic glasses (HEMGs).

The structure of HEAs can be predicted mainly by two parameters [13]: the atomic size difference (δ) and the mixing enthalpy (ΔH_{mix}). The atomic size difference is defined as

$$\delta = \sqrt{\sum_{i=1}^{n} c_i \left(1 - \frac{r_i}{\bar{r}}\right)^2} \tag{1.4}$$

where r is the average atomic radius and c_i and r_i are the atomic percentage and atomic radius of the i-th component [14]. The mixing enthalpy is defined as

$$\Delta H_{mix} = \sum_{i=1, i \neq j}^{n} 4\Omega_{ij} c_i c_j \tag{1.5}$$

Here $\Omega_{ij} = \Delta H_{mix-ij}$ is a regular solution interaction parameter between the i-th and j-th elements, representing the enthalpy of mixing for binary equal atomic alloys composed of these two components. The values of δ and ΔH_{mix} determine if a solid solution or an amorphous phase is formed (see figure 1.5). In particular, a solid solution can be produced if δ is small ($\delta < \sim 0.066$) and ΔH_{mix} is either slightly positive or significantly negative ($-11.6 < \Delta H_{mix} < 3.2$ kJ mol^{-1}) whereas an amorphous phase can be produced if δ is large ($\delta > 0.064$), and ΔH_{mix} is negative ($\Delta H_{mix} < -12.2$ kJ mol^{-1}) [8].

8
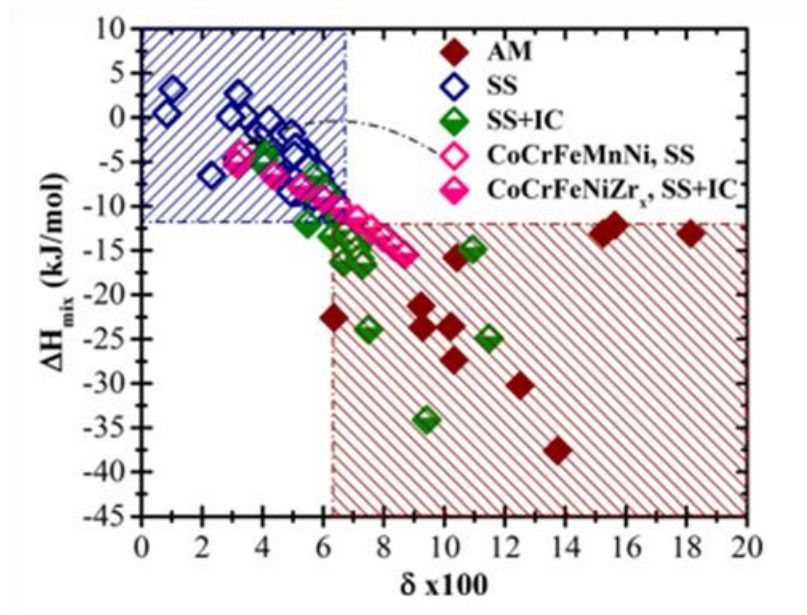
Figure 1.5 A typical two-dimensional $\delta - \Delta H_{mix}$ plot showing the phase formation in HEAs, including the regions where solid solutions (SS) or amorphous (AM) structures can be found (taken from ref. [15]).

1.3.1. Properties and applications of High-Entropy Alloys

HEAs have an intensive lattice distortion effect which is related to the different atomic radius of the various elements. This kind of effect can prevent dislocation movements and yield to these materials a high strength and hardness. At the same time the interaction of the different alloying elements is exacerbated, thus, high entropy alloys reflect the comprehensive properties of all kind of alloying elements. High entropy alloys also have a nice corrosion resistance, due to the simplified crystal structure, that can be higher than the one of widely used stainless steels [16].

High entropy alloys can be used as cutting tools. We can compare the friction and wear behavior of high entropy cutting tools with ordinary steels: while external load and rotational speed are fixed, the friction of high entropy alloy coated cutting tools is always lower than the ordinary high-speed steel. High entropy alloys used as coatings on the surface of cutting tools can reduce the friction force in the cutting process, extend the tool life and amend the surface quality of machined surfaces [16]. Moreover, some high entropy alloys have excellent hydrogen storage capacity. Sahlberg et al. demonstrated that a high the entropy alloy TiVZrNbHf can absorb a much higher amount of hydrogen than its constituents due to its distorted BCC-structure which has a large capacity to store hydrogen. In general a simple structure, often BCC or FCC, and the presence of lattice strains in the lattice or at interfaces can be favorable for hydrogen storage due to the variation in atomic size radii of the constituent atoms [17].

1.4. Alloy design

In the present thesis a new composition of a high-entropy metallic glass has been produced and characterized combining a well-known metallic glass system ($Fe_{80}B_{20}$) with a high-entropy alloy ($FeCoCrNi$). On one side, $Fe_{80}B_{20}$ has an amorphous structure at room temperature and it exhibits great soft magnetic properties, high abrasive resistance and good corrosion resistance. On the other side, $FeCoCrNi$ is an equiatomic high entropy alloy with both high tensile strength and ductility with a face-centered cubic (FCC) structure [18]. It is a well-known strategy for improving the glass forming ability of an alloy to add elements with a low atomic weight, such

9

as B or Si, and they are usually introduced into a ferromagnetic metal matrix [19]. The HEA FeCoCrNi has been extensively studied and its strength has been improved through the addition of minor elements that induce the precipitation of a second phase grains [18][20]. This composition was used by Ding et al. as a base composition for developing new HEMGs in which 18 to 22 at.% of B was added [21], thus combining the characteristics of $Fe_{80}B_{20}$ with the HEA design strategy in which the Fe atoms were substituted by equal amounts of Fe, Co, Cr and Ni. These HEMGs show a higher hardness, ductility and improved corrosion resistance as compared with the Fe-B amorphous alloys. On the other hand, Qi et al. produced (FeCoNi)(B,Si) high-entropy bulk metallic glasses with good soft magnetic and mechanical properties [22]. Thus, HEMGs with this set of elements could offer a combination of properties very useful for industrial applications. However, a complete characterization of the microstructural development during annealing is needed in order to be able to tailor their properties by means of thermal treatments and to control the evolution of their properties during working conditions in actual applications.

The present thesis is organized in the following way. In chapter 2 we will introduce all the experimental methods for production and characterization of the alloys. In chapter 3, a complete characterization of the alloys is shown, including structural and thermal characterization with the help of differential scanning calorimetry, conventional and synchrotron X-ray diffraction, scanning electron microscopy and Mössbauer spectrometry. In chapter 4, the results of the mechanical characterization will be presented, measuring the hardness and wear resistances of the samples using the nanoindentation method. In chapter 5 the electrochemical characterization will be shown. Finally, in the last chapter, the conclusions of this thesis will be presented.

CHAPTER 2. EXPERIMENTAL METHODS

2.1. Sample preparation

Multicomponent alloys with composition $(FeCoCrNi)_{100-x-y}B_xSi_y$ (with x= 0, 5, 10, 15, 20 and y=0, 5, 10, 15, 20 at%) were produced. The detail of each composition is shown in Table 2.1, together with the labels assigned to each composition.

Composition	Label	Observations
$(FeCoCrNi)_{80}B_{20}$	A80B20	Objective: Preparation of new high entropy metallic glass alloys and study of their structural, thermal and mechanical properties. Results: Amorphous alloys; characterization results are presented in the different chapters of this work.
$(FeCoCrNi)_{80}B_{10}Si_{10}$	A80B10Si10	
$(FeCoCrNi)_{75}B_{10}Si_{15}$	A75B10Si15	
$(FeCoCrNi)_{70}B_{10}Si_{20}$	A70B10Si20	
$(FeCoCrNi)_{70}B_{15}Si_5$	A70B15Si5	
FeCoCrNi	A100	Objective: Determination of the composition dependence of the glass forming ability of the FeCoCrNi-BSi system. Results: Partially crystalline and crystalline alloys.
$(FeCoCrNi)_{80}Si_{20}$	A80Si20	
$(FeCoCrNi)_{90}B_5Si_5$	A90B5Si5	
$(FeCoCrNi)_{85}B_{10}Si_5$	A85B10Si5	
$(FeCoCrNi)_{80}B_5Si_{15}$	A80B5Si15	
$(FeCoCrNi)_{75}B_{15}Si_{10}$	A75B15Si10	
$(FeCoCrNi)_{70}B_{20}Si_{10}$	A70B20Si10	
$(FeCoCrNi)_{60}B_{20}Si_{20}$	A60B20Si20	
$(FeCoCrNi)_{70}B_{15}Si_{15}$	A70B15Si15	
$(FeCoCrNi)_{85}B_5Si_{10}$	A85B5Si10	
$(FeCoCrNi)_{75}B_{10}Si_{15}$	A75B10Si15	

Table 2.1. List of compositions that has been explored in this work together with a description of their structure.

As a first step, the raw materials are cut and polished and, afterwards they are cleaned with acetone or alcohol to remove possible contamination. Finally, these raw materials are weighted with a high precision Semi-micro Discovery balance (AP110S). The purity and physical form of the used raw elements are the following: 99.95 % for Fe sheet, 99.95% for Chromium lumps, 99.5% for Cobalt lumps, 99% for Boron lumps, 99.98% for Nickel wire and 99.999% for Silicon lumps. In the next step, the master alloy is prepared by using an arc furnace (Edmund

Buhler GmbH model MAM-1, see Figure 2.1a) under 99.999 % inert argon atmosphere. In order to further decrease the content of oxygen, a small ball of Titanium is melted before the melting of the elements. The arc-melter has a water-cooled copper crucible plate to cool down the master alloy rapidly as well as to prevent the copper base from heating. The maximum temperature that can be locally reached is close to 3500 ºC. In all the cases, the master alloy is re-melted twice to assure its homogeneity. After cooling the master alloy, it is transferred to the melt spinning device (SC Edmund Buhler GmbH, see Figure 2.1b).

a)

b)
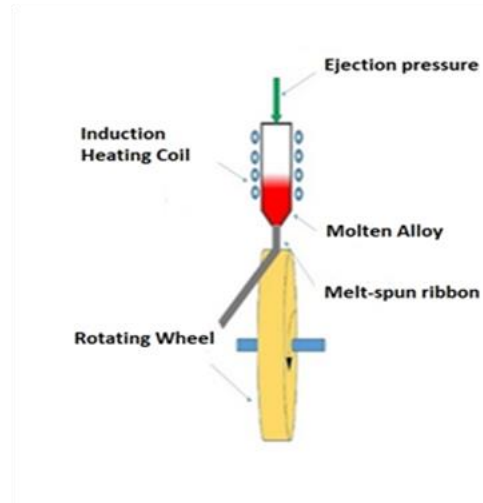
c)

Figure 2.1 (a) Arc melter device, (b) scheme of the melt spinner, (c) ribbons produced by melt spinning.

The master alloy is placed in a quartz crucible and mounted in the chamber so that the end of the crucible is 1mm above the copper spinning wheel. The quartz crucible has a small hole (1 mm in diameter) in the bottom to allow the ejection of the melted alloy. In order to avoid

contamination and oxidation, a vacuum below 10^{-3} Pa is created inside the melt spinner chamber with the help of a turbo-molecular pump. Afterwards, the chamber is filled with argon gas at the desired pressure to assure an inert atmosphere during the process, and the master alloy is melted using an induction coil. The molten alloy is ejected to the rotating copper wheel by applying an overpressure on the top part of the crucible. Due to the high thermal conductivity of the copper, the molten alloy is rapidly solidified in a ribbon shape.

There are several factors which can have an effect on the quality of the ribbons which are produced by melt spinner, such as: 1) the distance between the crucible and the copper wheel; 2) the diameter of the hole in the bottom of crucible; 3) the rotational speed of the copper wheel which can affect the thickness of the ribbons and 4) the pressure which is applied to eject the melted alloys from the crucible.

The parameters used in this work are the following: the distance between the end of the crucible and the wheel is 1 mm, the pressure difference (overpressure) is around 0.4 bar and the tangential speed of the copper wheel is 40 ms^{-1}. These parameters yield ribbons with 20-30 μm in thickness and 2 to 4 mm in width (see Figure 2.1c).

Afterwards, to obtain samples at different degrees of structural evolution, from the amorphous state to the fully crystalline one, some pieces of the as-quenched ribbons of $(FeCoCrNi)_{80}B_{20}$ and $(FeCoCrNi)_{80}B_{10}Si_{10}$ were annealed in a conventional furnace (Muffle furnace Fuji-PXR-4) at various temperatures (673, 723, 773, 823, 873, 923, 973 K) with a heating rate of 6 K min^{-1} under a stream of nitrogen gas. The samples were kept at the highest temperature for 60 min and then cooled down to room temperature with the same heating rate.

2.2. X-Ray Diffraction (XRD)

X-ray diffraction is one of the most important techniques used for phase identification of crystalline materials using electromagnetic radiation with typical wavelengths in the range of 0.5-2.5 Å, which is useful for studying the crystalline structure of materials because the distance between atoms in solids is compatible with the wavelength of the X-ray. The interaction of the X-rays with the electrons of the studied sample results in a process of scattering of the radiation that is distinctive for each material as they have a unique atomic structure. The resulting diffraction pattern of crystalline materials contain multiple peaks

13

known as Bragg diffraction peaks [23] (see Figure 2.2a), that appear at angular positions defined by the Bragg law

$$2d \sin \theta \ = \ n\lambda \qquad\qquad (2.1)$$

where d is the perpendicular distance between a pair of adjacent planes, θ is the angle of incidence or Bragg angle, λ is the wavelength of the beam and n is an integer number which is known as the order of reflection and is the path difference, in terms of wavelength, between waves scattered by adjacent plans of atoms.
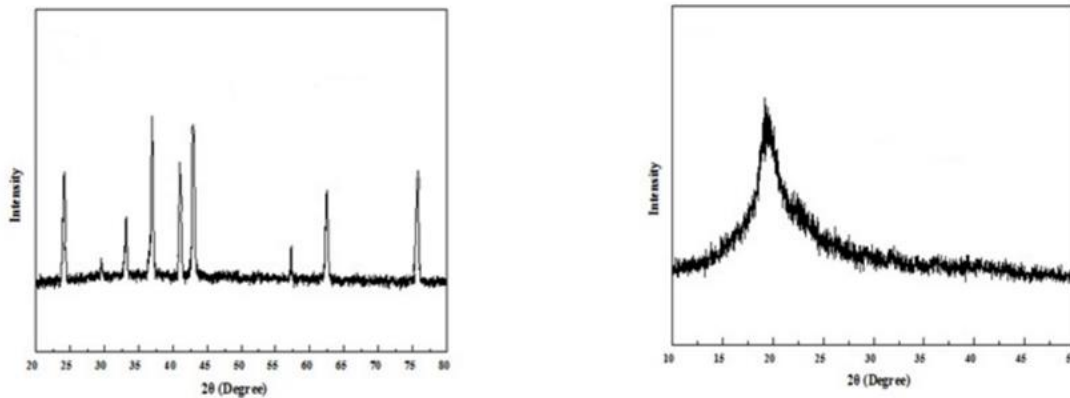
Figure 2.2 (a) XRD pattern of a crystalline alloy and (b) XRD pattern of amorphous samples [24].

For amorphous materials, the diffraction pattern shows a large bump distributed over a wide angle (2θ) instead of high intensity narrow peaks as indicated in Figure 2.2b. This wide peak has its origin in the fact that amorphous materials do not have long periodicity (no long-range order), and atoms are randomly distributed in all directions, so the diffracted X-rays from amorphous materials will be scattered in many directions leading to the large bump in the spectra. In this work, the Bruker D8 Advance X-ray diffractometer has been used with monochromatic X-rays using the Cu-K$_\alpha$ radiation ($\lambda = 0.1541$ nm) over a 2θ range from 20° to 100° with a scanning step of 0.02° both for the as-quenched and annealed samples.

2.3. Synchrotron X-ray diffraction

A synchrotron facility is a particular type of particle accelerator, in which electrons are accelerated by an electric field and are forced to travel around a fixed closed-loop path by magnetic fields. The acceleration produced by the magnetic fields to keep the electron beam into its closed path causes the emission in the tangent direction of electromagnetic waves from the electrons. The radiation thus emitted is called synchrotron radiation and its most important

14

advantage compared to the conventional X-ray laboratory equipment is a highly collimated and almost parallel beam and a photon flux which is several orders of magnitude higher than the one obtained in conventional X-ray sources. Another characteristic of synchrotron radiation is that it can be tuned in energy (at the different beamlines) and radiation with energy from the infrared to the X-rays can be achieved. Therefore, the materials of interest can be studied in many different ways and due to the high photon flux of the radiation better quality information in less time can be obtained compared to the traditional X-ray sources.

In this thesis the structural changes during the crystallization of the amorphous ribbons were measured in-situ while applying a constant heating rate. The measurements were carried out in the beamline BL04 – MSPD (Material Science and Powder Diffraction Beamline) at ALBA (see Figure 2.3a) with an incident energy of about 29.2 keV (the beamline operates between 8 and 50 keV) and a wavelength of $\lambda = 0.4246$ Å with focused micrometer beam size which was about 20×20 μm^2. A special furnace (a Linkam hot stage, Figure 2.3b) to change the temperature of the sample was used while taking spectra every 5 seconds to investigate the phase transformation. The Linkam hot stage can reach a maximum temperature of 873 K while some of our samples crystallize above this temperature, so the samples were kept at 873 K for 120 minutes to complete the crystallization.
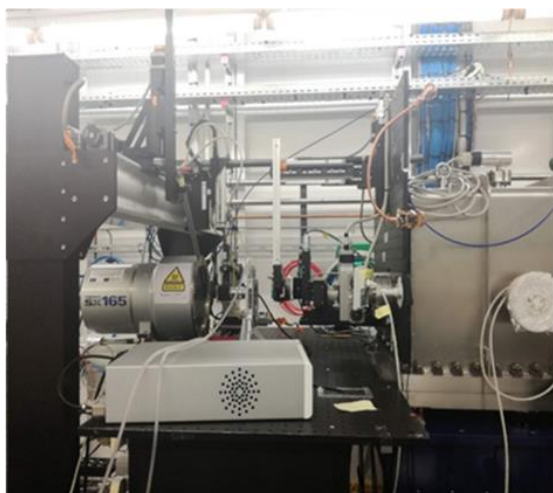
a)   b)

Figure 2.3 (a) BL04-MSPD (Material science and powder diffraction Beamline setup. (b) Linkam holder with the Al disc and the attached ribbons.

The ribbons with a thickness of about 20-30 μm and a width of 2-3 mm were mounted on an Aluminum disc with a 3 mm hole in the middle that is attached to the Linkam. The ribbons were hold in the hot stage with silver paint (see figure 2.3b). The temperature increased from room temperature up to 873 K at a heating rate of 20 K min⁻¹ and a spectra was recorded every 5 seconds. The diffraction pattern of the background was recorded at room temperature and subsequently subtracted from the sample signal after intensity normalization.

2.4. Differential Scanning Calorimetry (DSC)

Differential Scanning calorimetry (DSC) is the most commonly used method for studying the thermal properties of various materials. In DSC, the sample and reference are kept in two places and the temperature rises in both at the same rate, so the instrument begins to measure the difference in heat flow between the sample and reference. In the constant heating mode, the temperature increases linearly with time [25]. DSC is used to measure different material properties such as the glass transition temperature T_g, the crystallization temperature T_x, the melting point T_m, the heat capacity, etc. DSC shows exothermic and endothermic peaks that can be associated with crystallization events and the melting point respectively. with DSC data, the reduced glass transition temperature T_{rg} and the supercooled liquid region ΔT_x can be calculated to study the thermal stability of the system. In this work, the DSC measurements of the alloys were performed using a NETZSCH 404 F3 instrument, shown in figure 2.4. The heating rate used was 20 K min⁻¹ and from room temperature up to 1573 K under a flow of Nitrogen.

Figure 2.4 NETZECH 404 F3 Differential Scanning Calorimetry (DSC).

2.5. Scanning Electron Microscope (SEM)

The Scanning Electron Microscope (SEM) is an important technique that uses a focused ion beam to produce an image of the surface of a sample. It consists essentially of an electron gun that emits electrons to the sample, condenser lenses to control the path of these electrons and detectors that measure the different signals that come from the interaction between the electrons and the sample such as secondary electrons, backscattered electrons and characteristic X-rays. Basically it can produce an image of the sample surface with very high resolution showing details down to 5 nm. In this work, the SEM is mainly used to identify and quantify the chemical composition by energy -dispersive x-ray spectroscopy (EDS) [26]. In the present work, the images of as-quenched samples, annealed samples, and samples after nanoindentation tests were taken by Zeiss NEON 40 device Focused Ion Beam/Scanning electron microscopy (FIB/SEM). Sample surface was analyzed with a SEM with electron beam energy of 15 keV. Since the samples are in ribbon form, for the characterization of the inner parts of the ribbons a trench of 15 µm depth was dug with a Focused Ion Beam of Ga ions. To avoid the damage of the ribbon, a Pt protective coating was previously deposited on the surface. Image J software was used to analyze the images and to measure the size distribution of the grains in the partially crystalline and crystalline samples. The Energy-dispersive X-ray spectroscopy (EDS) was used for qualitatively analyzing the chemical composition.

17

2.6. X-ray Photoelectron Spectroscopy (XPS)

The X-ray photoelectron spectroscopy (XPS) was performed with a SPECS system equipped with a Phoibos 150 MCD-9 detector and an Al anode XR50 source working at 150 W. For the high-resolution spectra, a scan step of 0.1 eV was applied. The sample spot analyzed had a diameter of 1 mm^2 and the Casa XPS program (Casa software Ltd.,Teignmouth, United Kingdom) was used to evaluate the data. The spectra were normalized on the binding energy scale relative to the position of C 1 s peak at 284.8 eV and the intensity of the adventitious carbon signal was not taken into consideration. The shown spectra are not normalized on the intensity scale.

2.7. Mössbauer Spectroscopy

Mössbauer Spectroscopy is a technique which can give us information about chemical, structural and magnetic properties of materials by studying the hyperfine interactions in the nuclei. It works based on the resonant emission and absorption of gamma-rays by an atomic nucleus without recoil [27]. For one nucleus to emit a γ-ray and the second nucleus to absorb it, the atoms containing the two nuclei must be bonded chemically in solid state. With the help of Mössbauer spectroscopy we can measure isomer shifts and nuclear moments (i.e spin, magnetic dipole, and electric quadrupole moments). Mössbauer spectrometry can be performed with different nuclei like ^{57}Fe,^{119}Sn, ^{151}Eu, ^{121} Sb and ^{161}Dy but the nuclei of ^{57}Fe is the most suitable one for achieving recoilless resonance. A basic Mössbauer spectrometer includes three important parts: the radioactive source, the absorber (the material to be studied) and a detector. If the emitting nuclei and absorbing nuclei are not in the same chemical state there would be no resonance, thus the energy of the emitted photon should be changed and this is done by Doppler effect moving the source (or the absorber). Here the radioactive source of ^{57}Co in a Rh matrix produce the γ radiation with an energy of 14.413 keV by the decay of ^{57}Co to excited ^{57}Fe. The energy levels in the Fe nucleus of the sample (absorber) can change due to the presence of magnetic fields, electric field gradients or other factors, thus the energies at which the resonance takes places yield information on the so-called hyperfine parameters that are described in the following.

a) Isomer shift: is a shifting in the energy levels involved in the nuclear transition due to a difference in the radius of the atom between the excited and the ground state. This parameter

18

gives information about the chemical bonding and the crystal chemical environment. b) Quadrupole splitting: if the electrical charge distribution around the Fe nucleus is not symmetric, and electric field gradient appears causing the splitting of the energy levels of the nucleus. Therefore, the quadrupole splitting can give information on the distortion of lattice surrounding the absorbent Fe nucleus.

c) Magnetic splitting: the interaction between the magnetic moment of the nucleus and the magnetic moment of surrounding atoms or an externally applied field causes the separation of the nuclear spin levels, the Zeeman effect. For ^{57}Fe, this splitting gives rise to six possible transitions. This parameter gives information on the magnetism of the sample.

In this work, the Mössbauer spectra were taken in transmission mode at room temperature and pressure using a conventional constant acceleration spectrometer with a 25 mCi source of ^{57}Co in a Rh matrix. The experimental spectra were fitted with Brand's Normos program [28].

2.8. Nanoindentation

Nanoindentation tests are useful for evaluating various mechanical properties such as hardness (H), reduced elastic modulus (E_r), plastic energy (U_P), elastic energy (U_E), wear-resistance and elastic recovery. Modern nanoindentation devices (see Figure 2.5) have an automatic process and are very accurate. Most of the nanoindenters use the Oliver and Pharr method [29] to analyze the force-displacement curves obtained by indentation.
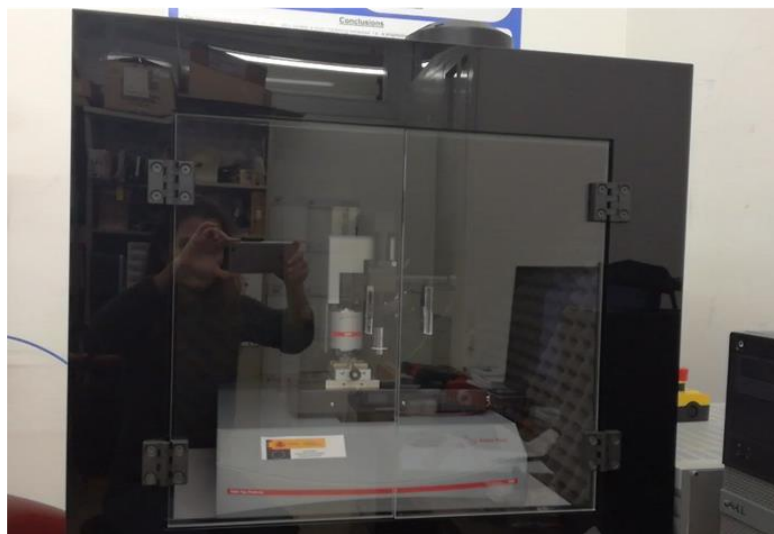
Figure 2.5 Nanoindentation device in Universitat Autònoma de Barcelona with a Berkovich indenter.

In a nanoindentation process the load-displacement curve during loading and unloading is obtained and used to calculate the hardness H and the reduced elastic modulus E_r. The hardness H of the specimen is calculated according to

$$H = \frac{P_{max}}{A_C} \tag{2.2}$$

where P_{max}, is the maximum indentation load and A_c is the contact area under load. For a perfect Berkovich indenter, like the one used in this work, the contact area can be obtained as a function of the contact depth, h_c, with the following equation

$$A_c = \pi . tan^2\psi . h_c^2 = 24.56 . h_c^2 \tag{2.3}$$

where $\psi = 70.32°$ and represents the effective semi-angle of the conical indenter equivalent to the Berkovich one. This is important because in some cases there are phenomena such as pile-up and sink-in that can lead to errors in the estimated contact area. In this study we use continuous stiffness measurement (CSM), which is shown schematically in Figure 2.6, and from the load-displacement curve the slope of the unloading curve is used to calculate the stiffness values S.
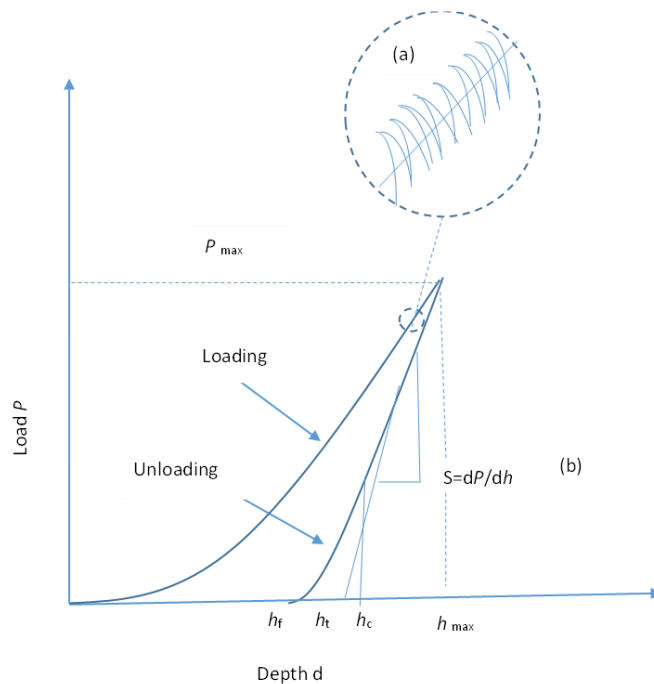
Figure 2.6 Continuous stiffness measurement (CSM) showing: (a) the detail of the loading curve and (b) the calculation of the stiffness by the slope of unloading curve [30].

The stiffness value is calculated by the following equation

$$S = \frac{dp}{dh} = \beta \frac{2}{\sqrt{\pi}} E_r . \sqrt{A} \tag{2.4}$$

20

where the stiffness is calculated by the first derivative of the load along the load-displacement curve during the unloading process and β depends on the geometry of the indenter (for a Berkovich indenter β is 1.034). E_r is the reduced elastic modulus that can be computed from equation

$$\frac{1}{E_r} = \frac{1 - v^2}{E} + \frac{1 - v_i^2}{E_i} \tag{2.5}$$

where v and E are the Poisson ratio and the elastic modulus of the sample and v_i and E_i are the same properties for the material of the indenter tip. The wear resistance of the samples can be calculated by the H/E_r ratio and the elastic recovery can be evaluated as the ratio between the elastic and the total (elastic + plastic) energy during the nanoindentation, U_{el}/U_{tot}. These energies are calculated in a nanoindentation experiment from the area between the unloading curve and the x-axis for the case of U_{el} and from the area between the loading curve and the x-axis for the case of U_{tot} [31].

In this work, the nanoindentation measurement of the as-quenched and annealed samples was obtained employing a NHT2-Anton Paar nanoindenter on the middle of the cross-section area of the samples which were mounted on a resin base and mechanically polished with different sandpapers in a Struers Roto Pol-11 Surface Polisher (Cleveland, OH). In the final step, we used Diamond compound and 1 μm sandpaper. This nanoindenter used a Berkovich pyramidal-shaped diamond tip under load control mode, the maximum applied load was 10 mN with a loading segment of 30 s followed by a load holding segment of 5 s and by an unloading segment of 30 s with a thermal drift below 0.005 nm s^{-1}. It used continuous stiffness measurement to collect material properties information as a function of displacement.

2.9. Corrosion

Corrosion is an electrochemical process in which electrons are transferred between the material (mostly metal) and the environment, the corrosion reaction is basically divided in to a cathodic and an anodic reaction. In the anodic reaction, the material (metal) is oxidized and release electrons

$$M \rightarrow M^{n+} + ne^-$$
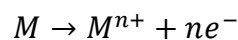
In the cathodic reaction, the reduction proceeds as follows

1. $O_2 + 2H_2O + 4e^- \rightarrow 4OH^-$ Neutral and alkaline solutions

2. $2H^+ + 2e^- \rightarrow H_2 \uparrow$ Hydrogen evolution (in acidic conditions)

For measuring the corrosion resistance of various materials, we usually need an electrochemical cell containing a metal electrode and an electrolyte. In an electrochemical cell, a continuous electrochemical reaction take place, so chemical energy is converted in to electrochemical energy, therefore the change in energy can be calculated using

$$\Delta G = -nFE \tag{2.6}$$

where n is the number of electrons involved, F is the Faraday constant (9.648×10^4 C mol^{-1}) and E is the cell potential which is the potential difference between the two half cells. The negative sign in this equation indicates that the cell serves as an energy source. Here in the first step all the electrodes in the solution are connected together and remain for some time without being connected to an external electrical connection. By this way we can measure the potential in the circuit when it is stable, which is called the open circuit potential E_{oc}. There are several ways of measuring the electrochemical properties of a sample, being two of the most important the linear polarization resistance and the electrochemical impedance spectroscopy.

Linear polarization resistance.

To measure the linear polarization resistance (LPR) we apply a potential above and below the open circuit potential E_{oc} and then record the current using a potentiostat. The resulting curve is called a Tafel plot, an example shown in Figure 2.7
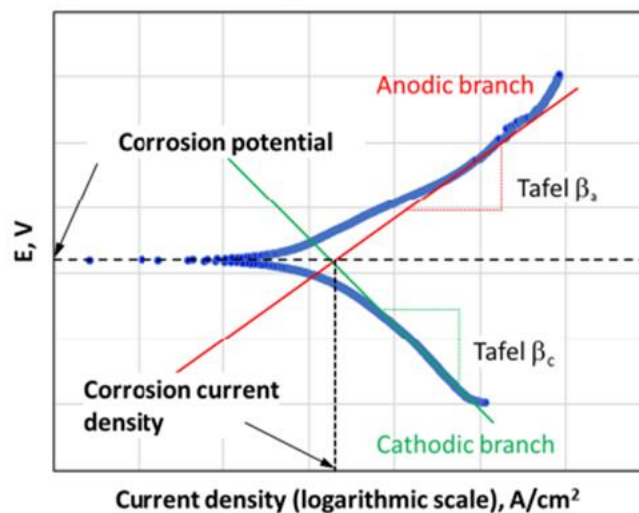
Figure 2.7 Schematic corrosion process illustrating the anodic and cathodic current components [32]

22

In this work the potential is always measured with respect to the Ag/AgCl (3.5M in KCl) electrode that act as a reference potential. The measurement starts with a potential scan from below the open circuit potential; the potential at which the current becomes zero is called the corrosion potential E_{corr}, signaling the point at which the rate of oxidation is equal to the rate of reduction. For calculating the I_{corr} we can use the Tafel slope of the anodic reaction β_a, which is the slope of the linear region in the anodic branch, and the Tafel slope of the cathodic reaction β_c which is the slope of the linear region in the cathodic branch. The intersection of these two slopes give us the I_{corr} (see Figure 2.7)

Electrochemical Impedance Spectroscopy.

In an electrochemical impedance spectroscopy (EIS) experiment an alternating potential or current is applied to the sample and the response of the electrochemical system is measured. There are two ways of showing the data, the Nyquist plot or the Bode plot. In the Nyquist plot, for each excitation frequency, the real part of the impedance is plotted on the x-axis and the imaginary part is plotted on the y-axis (Figure 2.8(a)), whereas in the Bode plot the data is plotted with the logarithm of the frequency on the x-axis and the logarithm of the absolute value of the impedance ($|Z|$) and the phase-shift (θ) on the y-axis (Figure 2.8(b)).

a)   b)
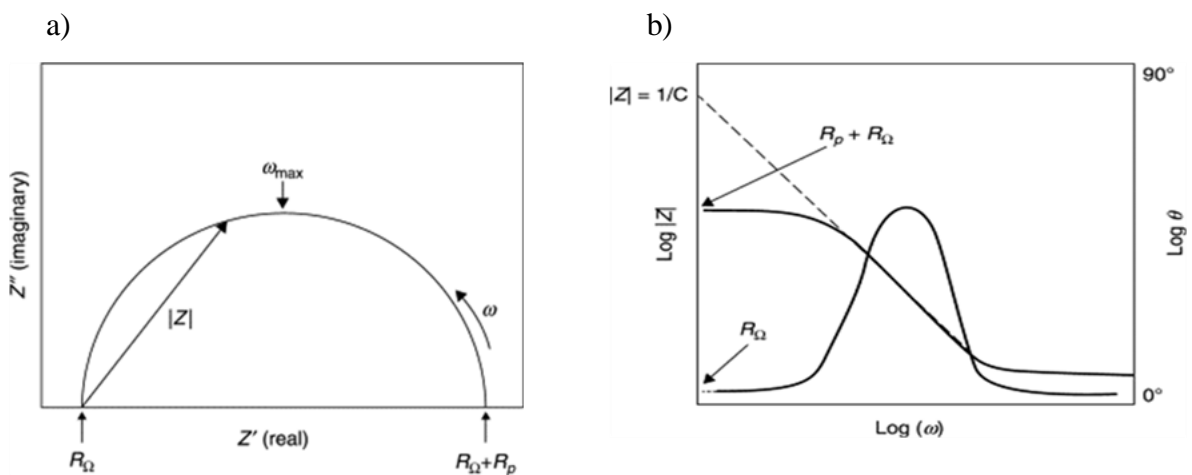
Figure 2.8 (a) Nyquist plot (b) Bode plot [33].
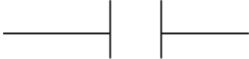
To simplify and better understand the EIS data, we can use the equivalent circuit diagram which contains various components such as resistors, capacitors, constant phase elements and diffusion elements that are able to model the processes taking place during the electrochemical reaction. Each of these elements are briefly explained in the following:

23

Resistors. We can use resistors in the equivalent circuit for the condition of electron transfer from the electrode surface to the solution or vice versa, or even to describe the movement of charges through solids and liquid phases. The impedance of a resistor is simply equal to its resistance in units of ohms (Ω), $Z_R = R$, and is shown in the following figure

$$Z_R = R \tag{2.7}$$

Capacitors. When non-Faradic charges accumulate at the solid/solid and solid/liquid interfaces, we can use the capacitance model. These interfaces contain contacts between adjacent metal oxide particles or nanocrystal particles, the contacts between metal oxide and a conductive substrate or the double-layer formed at the solid/solution interface. We use the following equation (2.8) and the figure in the circuit. In this equation Z_c is the impedance of a capacitor.

$$Z_C = \frac{1}{j\omega C} = \frac{-j}{\omega C} \tag{2.8}$$

Constant Phase Elements (CPEs). In the electrochemical cell, which has inhomogeneities on the surface of the metal oxide electrode, such surface can be considered as a non-ideal capacitance in a double-layer at the solid/electrolyte interface. This model is mostly used for a non-ideal behavior that may be caused by surface roughness, irregularities or porosity, and it is presented by the following equation (2.9) and the figure in the circuit. Here Q is a non-ideal capacitance and has units of F and β is an ideality factor ranging from 0 to 1.

$$Z_{CPE} = \frac{1}{(j\omega)^\beta Q} \tag{2.9}$$

Warburg Diffusion. An important factor in EIS data analysis is the diffusion of mobile charges through metal oxide electrodes and in solution, this diffusion impedance (Z_w) is called Warburg diffusion and it is described by the following equation

$$Z_w = \frac{\sigma\sqrt{2}}{(\omega)^{1/2}} \tag{2.10}$$

where the σ term describes the resistance associated with diffusion as function of the concentration of charge carriers and their diffusion coefficients.

2.9.2. Experimental details

In this thesis, the effects of B and Si on the corrosion resistance of three selected samples of HEA (A) and HEMG (AB20 and AB10Si10) are evaluated. In section 2.1. it was explained that samples were prepared by a rapid solidification technique from high purity materials in ribbon shape, thus, they have a uniform homogeneous surface with a width of 1-2 mm and thickness of 20-30 µm. The corrosion tests for all the samples were performed on the air side of the ribbons (the side of the ribbon which is in contact with air during the process of solidification in the melt spinner) which acted as the working electrode in the electrochemical cell. For preparing the ribbons for the measurements, the ribbon was connected to a pure copper (99.9%) strip by a PTFE (Polytetrafluoroethylene) tape, which has a high temperature and corrosion resistance and good stability, to get an electrical connection. The copper strip and the wheel side of the ribbon were covered completely by the PTFE tape (Figure 2.9a) in order to assure that only the sample to study is in contact with the solution. This contact was measured with ImageJ software to be able to compute the corrosion intensity density.

Figure 2.9 a) Preparation method of ribbon samples for corrosion testing. b) Sketch of the electrochemical cell with three electrodes.

The electrochemical tests were performed in a three-electrode corrosion cell (figure 2.9b) and carried out in 3 wt% (0.51M) NaCl solution. The reference electrode was a Ag/AgCl (3.5M in KCl) (+0.205 V vs. saturated hydrogen electrode at 25 °C) and a spiral platinum wire (with an area of ~3.6 cm^2) was used as a counter electrode. The surface of the specimens exposed to the solution was around 0.08~1.31 cm^2. The measurements were performed with a SP-200 Bio-

logic potentiometer (Bio-Logic Science Instrument, France), shown in Figure 2.10 and controlled by the EC-Lab software. In the first step, the specimens were stabilized under open circuit condition for 1h. In this step, the potentiostat measures the open circuit potential as a function of time. At the end the of stabilization period, a quasi-steady state potential is attained which is defined as the open circuit potential. For avoiding the influence of external electromagnetic radiation, both electrochemical tests and immersion tests were done in a Faraday cage [34].
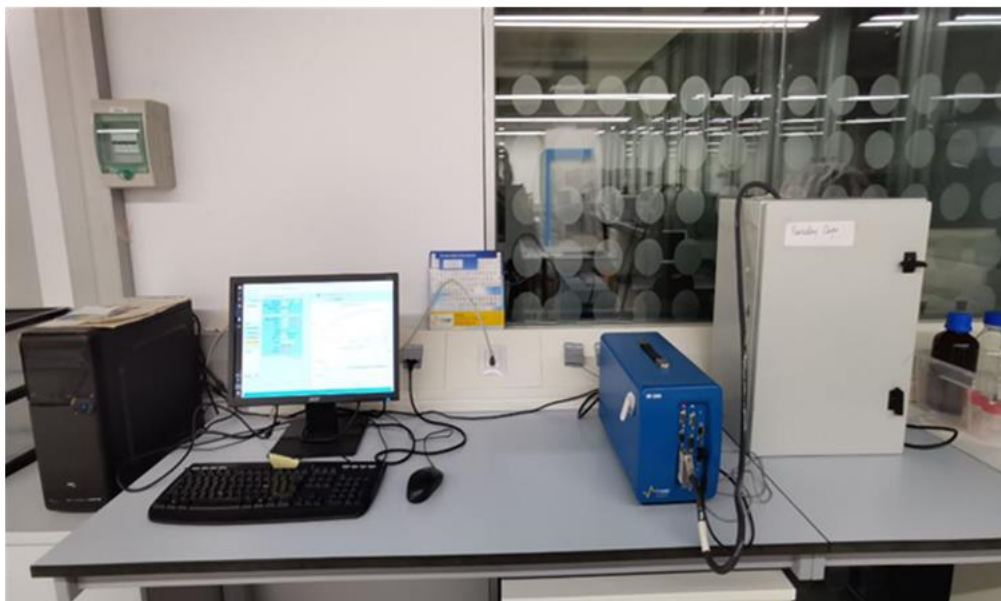
Figure 2.10 photo of electrochemical measurement system: Computer (left), Bio-Logic SP-200 potentiostat/Galvanostat (middle), and Faraday cage (right).

The linear potentiodynamic polarization curves were recorded starting at -100 mV relative to the OCP, and rising the potential in the anodic direction to 100 mV with a scan rate of 0.1 mV s^{-1}. The measurements were repeated at least three times with fresh samples. Before starting the scan, the sample remained in the solution for 1h to stabilize the open circuit potential (OCP). Finally, the EIS tests were performed by applying a sinusoidal potential of 10 mV of amplitude and a variable frequency in the range from 100 kHz to 100 mHz. The EIS spectra were recorded after 1h at the OCP.

CHAPTER3. MICROSTRUCTURAL CHARACTERIZATION

In this chapter, the process of casting the alloys by melt spinning and the characterization of the as–prepared and annealed HEMG ribbons are presented. Moreover, we will focus on the study of the crystallization process of the alloys. The thermal stability of the amorphous ribbons will be examined by differential scanning calorimetry (DSC) that helps us to find out the glass transition temperature (T_g) and the crystallization temperature (T_x) and we will characterize the changes in these two parameters by changing the percentage of the elements which are present in the alloy's composition. The microstructural characterization will be performed using X-ray diffraction (XRD) and Transmission Mössbauer spectroscopy (TMS). Finally, the distribution of particle sizes during the heat treatments will be obtained with the help of data from Scanning electron microscope (SEM).

3.1 Production of (FeCoCrNi) based alloys

During recent years the HEA $Fe_{25}Co_{25}Cr_{25}Ni_{25}$ has been extensively studied and its strength has been improved through the addition of minor elements such as Al, Mn, Cu, Pd, Ti or V. This composition was used by Ding et al. as a base composition for developing new HEMGs in which 18 to 22 at% of B was added. These HEMGs show a higher hardness, ductility and improved corrosion resistance as compared with the Fe-B amorphous alloys. Qi et al. produced (FeCoNi)(B,Si) high-entropy bulk metallic glasses with good soft magnetic and mechanical properties[22]. Thus, HEMGs with this set of elements could offer a combination of properties very useful for industrial applications. In this thesis we report the production of new HEMGs within the $(FeCoCrNi)_{100-x-y}B_xSi_y$ compositional system with x=0,5,10,15,20 and y =0,5, 10,15,20 in atomic percentages. The EDS analysis of the AB20 alloy was done in order to check the homogeneity of the produced samples taking this composition as representative of all the produced ribbons. The results are shown in Figure 3.1, where the SEM image is observed together with the compositional maps of an inner part of the ribbon. In the upper central part of the Figure, the atomic percentage of Fe, Co, Cr and Ni normalized to 100 are shown (the B cannot be detected by EDS) indicating a that the production process we followed is able to

generate the expected equiatomic composition. The rest of the panels show the concentration distribution of Fe, Co, Cr and Ni clearly demonstrating the homogeneity of the produced alloys.
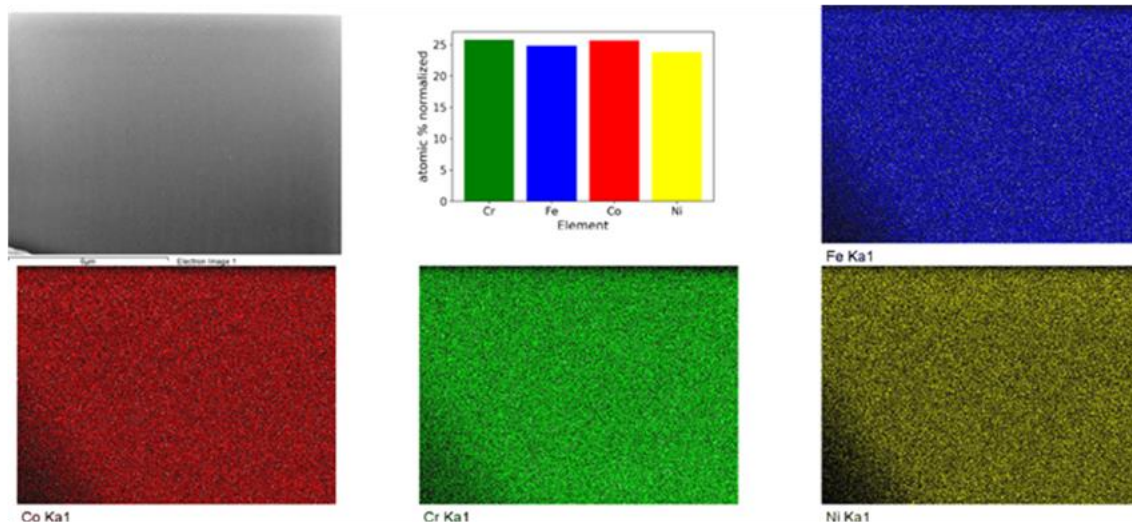
Figure 3.1 EDS maps of element distribution in the AB20 alloy.

High entropy alloys can be produced in crystalline structures (simple FCC, BCC or HCP solid solution structures) or, in some cases, in amorphous arrangements (metallic glass). As explained in the previous chapter, the master alloys were prepared by arc melting under argon atmosphere from high purity materials Fe, Co, Cr, Ni, B and Si. Amorphous ribbons were produced by melt spinning with a single Cu –roller. The thickness and width of the resulting ribbons were 20-30 μm and 4 mm, respectively.

3.2. Structural characterization

The X-ray patterns of the as quenched ribbons shown in Figure 3.2 (top) illustrate only one broad peak in the 2θ range between 11° to 14° and no diffraction peaks corresponding to crystalline phases are observed, while the $(FeCoCrNi)_{70}B_{15}Si_{15}$ alloy shows crystalline peaks over the amorphous halo, indicating that this composition is only partially amorphous. The large amplitude of the crystalline reflections, as compared to usual Bragg reflections, indicate the crystalline phase is possibly in the form of nanocrystals. Figure 3.2 (bottom) shows the diffraction pattern of the FeCoCrNi alloy clearly containing a single FCC structure, in accordance with previous work [35]. The figure also shows the crystalline patterns of the remaining compositions that are composed by single FCC or BCC structures or by multiple phases in some compositions. It is worth to mention that the XRD patterns of compositions

$(FeCoCrNi)_{90}B_{10}$ and $(FeCoCrNi)_{70}B_{20}Si_{10}$ can be compatible with a mixture of crystalline phases with a certain content of amorphous phase.
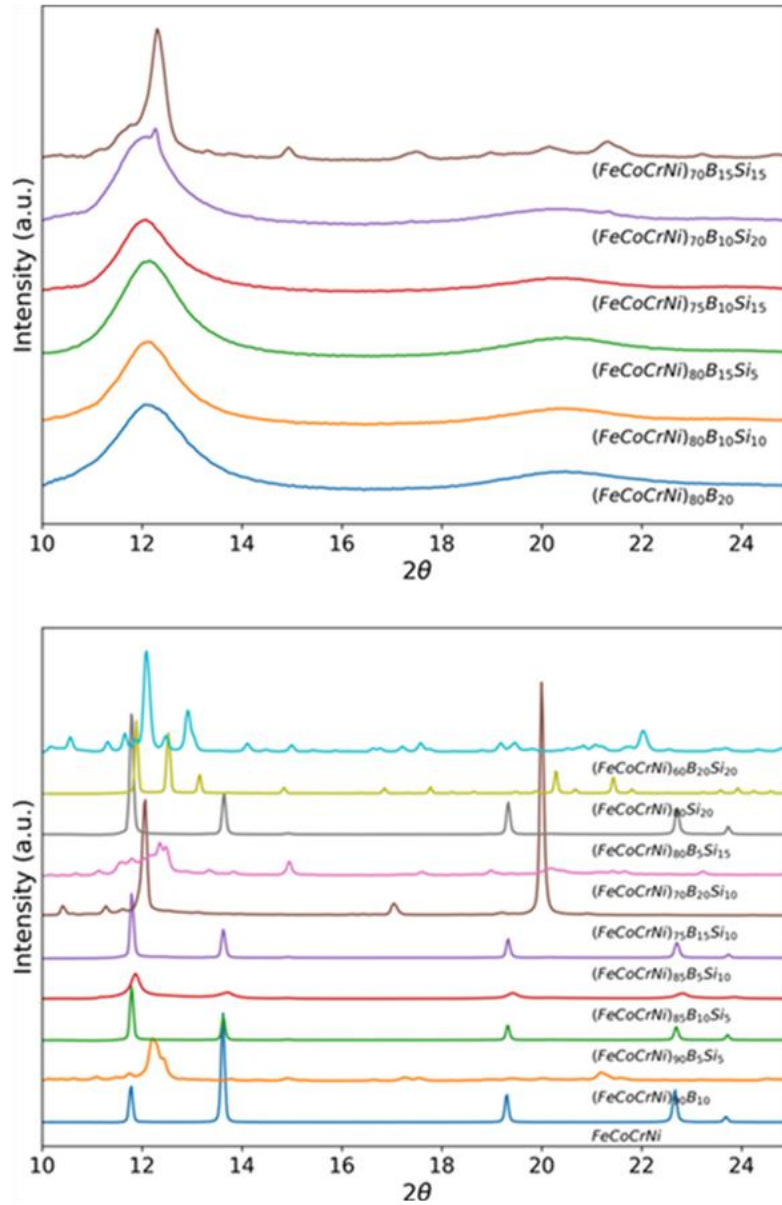
Figure 3.2 XRD patterns of the as-quenched samples. Diffraction spectra were obtained by synchrotron radiation with wavelength 0.425 Å. Amorphous or partially crystalline compositions (top) and crystalline compositions (bottom).

3.3. Glass formation

According to the results of the XRD patterns the different compositions of the $(FeCoCrNi)_{100-x-y}B_xSi_y$ system have been presented in Figure 3.3, indicating the structural state of the as-quenched ribbons. Glass-forming ability is observed for composition

(FeCoCrNi)$_{80}$B$_{20}$, as shown previously [21], as well as for the series of compositions substituting B by Si up to (FeCoCrNi)$_{80}$B$_{10}$Si$_{10}$. Within this range of compositions, the partial substitution of B by Si is not detrimental for the formation of an amorphous structure, thus obtaining a new class of high-entropy metallic glasses with Si content. The further substitution of B by Si results in crystalline samples. The increase of Si content maintaining a constant 10 at% of B produces amorphous samples up to (FeCoCrNi)$_{70}$B$_{10}$Si$_{20}$, the latter being already partially crystalline.
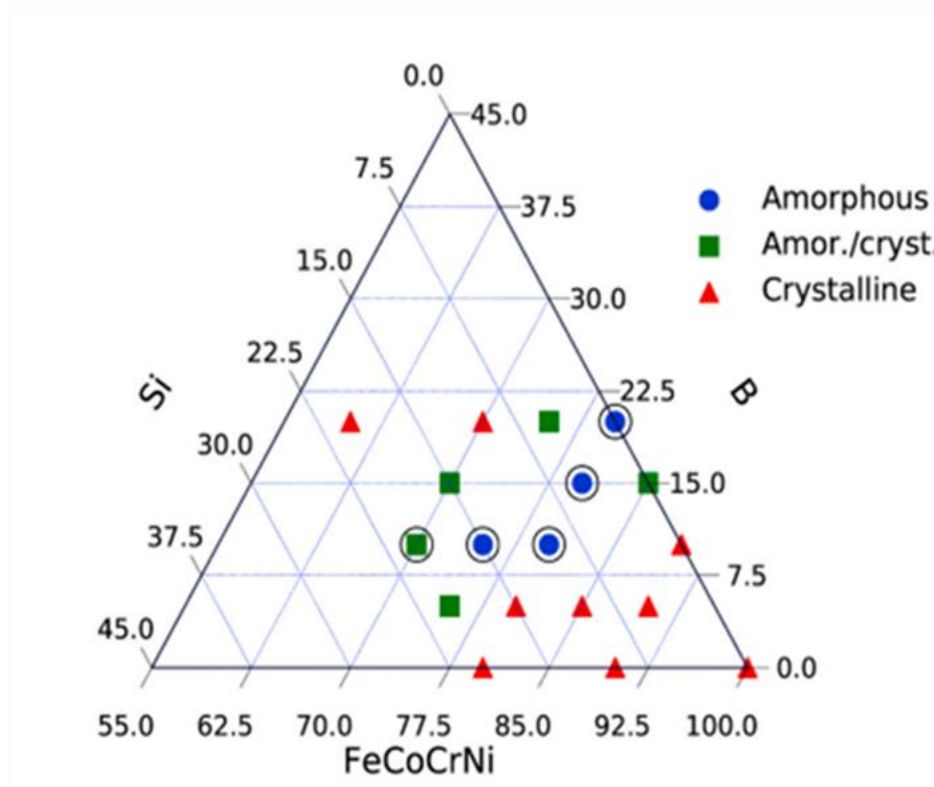
Figure 3.3 Pseudo-ternary phase diagram of the produced compositions reflecting the state of the as-quenched ribbons. Amorphous (blue circles), crystalline (red triangles) or partially crystalline structure (green squares).

As it was explained previously explained in the Introduction chapter of this thesis, it is possible to predict the structure of the alloy with the help of two parameters: the atomic size difference (δ) and the mixing enthalpy (ΔH_{mix}). The values of these parameters determine if a solid solution or an amorphous phase is formed. In particular, a solid solution can be produced if δ is small ($\delta < {\sim}0.066$) and ΔH_{mix} is either slightly positive or significantly negative ($\sim$ -11.6 $< \Delta H_{mix} < 3.2$ kJ mol^{-1}) whereas an amorphous phase can be produced if δ is large ($\delta > 0.064$), and ΔH_{mix} is negative ($\Delta H_{mix} < -12.2$ kJ mol^{-1}) [36]. The regions in the δ-ΔH_{mix} map where solid solutions or amorphous phases are favored following this model are shown in Figure 3.4 as dashed regions. In order to validate this empirical model, we calculated the atomic

size difference and the mixing enthalpy for the compositions produced, given in Table 3.1 and plotted in the δ-ΔH_{mix} map of Figure 3.4.

Alloy	δ	ΔH_{mix} (kJ mol^{-1})	Ref.
$(FeCoCrNi)_{100}$	0.30%	-3.75	[37]
$(FeCoCrNi)_{80}B_{10}Si_{10}$	10.72%	-23.36	This work
$(FeCoCrNi)_{80}B_{20}$	14.70%	-19.2	This work
$(FeCoCrNi)_{90}B_{10}$	10.64%	-12.48	This work
$(FeCoCrNi)_{75}B_{10}Si_{15}$	10.74%	-27.69	This work
$(FeCoCrNi)_{75}B_{15}Si_{10}$	12.87%	-26.01	This work
$(FecoCrNi)_{60}B_{20}Si_{20}$	14.47%	-34.19	This work
$(FeCoCrNi)_{70}B_{15}Si_{15}$	12.85%	-29.87	This work
$(FeCoCrNi)_{70}B_{20}Si_{10}$	14.61%	-28.15	This work
$(FeCoCrNi)_{80}B_{5}Si_{15}$	7.91%	-25.02	This work
$(FeCoCrNi)_{80}B_{15}Si_{5}$	12.89%	-21.42	This work
$(FeCoCrNi)_{85}B_{10}Si_{5}$	10.68%	-18.28	This work
$(FeCoCrNi)_{90}B_{5}Si_{5}$	7.72%	-14.65	This work
$(FeCoCrNi)_{80}Si_{20}$	3.07%	-26.4	This work
$(FeCoCrNi)_{85}B_{5}Si_{10}$	7.82%	-20.20	This work
$(FeCoCrNi)_{70}B_{10}Si_{20}$	10.74%	-31.30	This work

Table 3.1. Calculated parameters δ and ΔH_{mix} for all the alloys produced.

From the XRD results, we can distinguish between three cases in terms of the structural state: 1) Compositions with an amorphous as-quenched state; 2) Compositions with a crystalline state composed of borides, silicides and intermetallic phases (labeled as multiphase alloys), and compositions containing only FCC or BCC phases. For the latter ones, it is not known at this moment if the B and Si atoms could be inside the FCC or BCC structures, as substitutional or interstitial atoms, or accumulated in a small fraction of inter-granular amorphous phase in the grain boundaries and not detectable by X-ray diffraction.
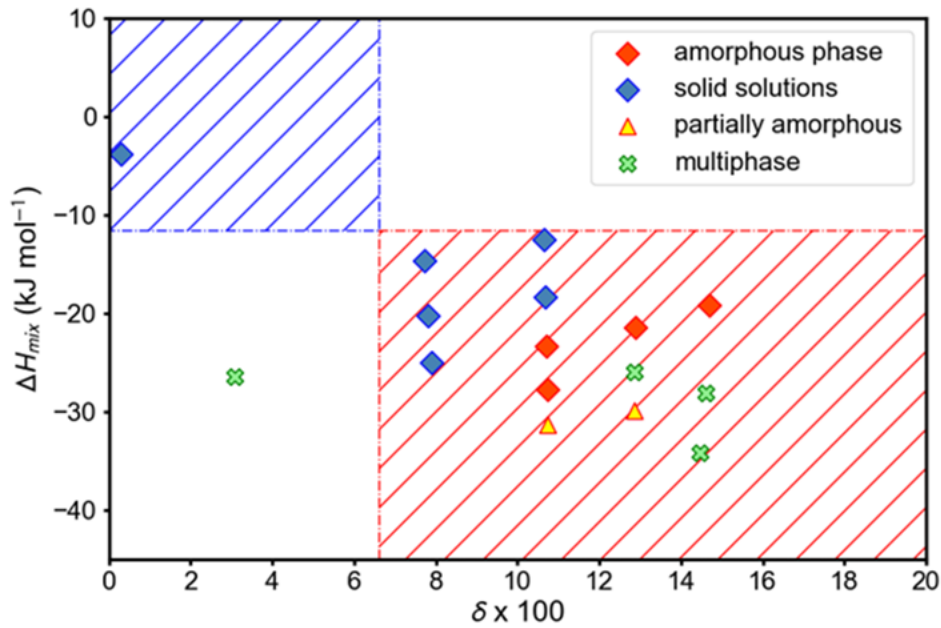
Figure 3.4 ΔH_{mix} versus δ map for as-cast high entropy alloys showing the regions favorable for obtaining crystalline solid solutions (upper left, blue dashed region) or amorphous alloys (lower right, red dashed region).

The results confirm the general criteria in the case of the FeCoCrNi alloy, as reported previously [4]. The alloys with B and/or Si that show crystalline FCC or BCC solid solutions in their as-quenched states fall in the amorphous region although close to the border with the solid solution region. The multiphase compositions do not follow any clear trend as they appear mostly in the amorphous region but also outside the expected ranges for either amorphous, intermetallic or solid solution formation. Therefore, the general criteria to distinguish between the tendency to form HEAs and HEMGs is only approximately valid in these compositions, probably due to the presence of large contents of metalloid atoms. Other factors, in addition to the values of ΔH_{mix} and δ, clearly play a role in determining the GFA in this compositional system.

3.4. Thermal characterization

The thermal stability of the ribbons was investigated by DSC in a continuous heating measurement up to 1500 K. The analysis of the DSC curves (Figure 3.5) shows a different crystallization behavior depending on the B and Si contents. AB20 shows a fast crystallization process and a second exothermic reaction at much higher temperatures. AB15Si5 and AB10Si10 show a crystallization reaction split in two peaks, while AB10Si15 shows a single

crystallization event at higher temperatures than for lower Si contents. The broad and small exothermic event for the AB10Si20 composition is a consequence of the existence of already formed nanocrystalline particles in the as-quenched ribbons as detected by XRD. Besides the number of crystallization events, the presence of Si in the samples also changes the temperature span between the first and second crystallizations, being maximum in the Si free composition and being the two crystallizations almost overlapped in the AB15Si5 and AB10Si10 samples.
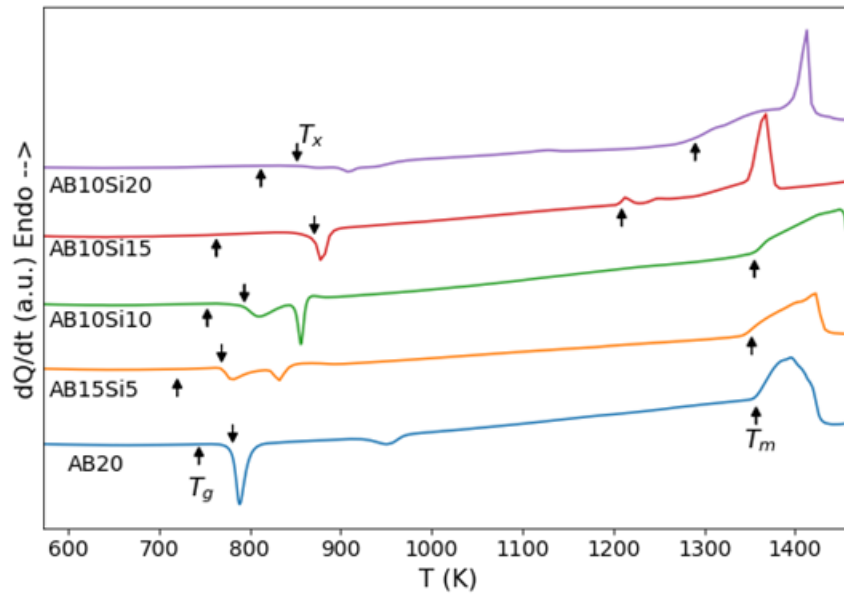
Figure 3.5 DSC of the as quenched samples applying a heating rate of 20 K min^{-1}.

The glass transition (T_g) and onset of the first crystallization event (T_x) temperatures are determined from DSC curves and from these parameters also the GFA of these HEMGs can be assessed from the supercooled liquid region ($\Delta T_x = T_x - T_g$) and the reduced glass transition temperature ($T_{rg} = T_g/T_m$). The values obtained from the DSC curves are shown in Table 3.2.

Alloy	Label	η	T_g (K)	T_{x1} (K)	T_m (K)	ΔT_x (K)	T_{rg}
FeCoCrNi	A	-	-	-	-	-	-
(FeCoCrNi)$_{80}$B$_{20}$	AB20	0	744	788	1353	44	0.55
(FeCoCrNi)$_{80}$B$_{15}$Si$_5$	AB15Si5	1/3	720	769	1337	41	0.54
(FeCoCrNi)$_{80}$B$_{10}$Si$_{10}$	AB10Si10	1	753	810	1349	57	0.56
(FeCoCrNi)$_{75}$B$_{10}$Si$_{15}$	AB10Si15	3/2	763	871	1203	108	0.63
(FeCoCrNi)$_{70}$B$_{10}$Si$_{20}$	AB10Si20	2	812	852	1278	-	-

Table 3.2. The glass transition temperature (T_g), onset of the first crystallization event (T_{x1}), melting temperature (T_m), supercooled liquid region (ΔT_x) and reduced glass transition temperature (T_{rg}) for the completely amorphous samples, indicating also the alloy label and the Si/B ratio (η).

The values of T_{rg} are in the range between 0.5 and 0.6. These relatively low values indicate that these compositions are not likely to be produced as bulk metallic glasses. One exception is the AB10Si15 sample that presents a slightly higher value. This sample is also the one that shows a higher thermal stability with the maximum value of ΔT_x. These results suggest that there might exist a critical amount of Si that maximizes the GFA and thermal stability.

3.5. Structural characterization and effect of annealing on the as-quenched ribbons

In order to study the evolution of the amorphous and crystalline phases during annealing, a series of heat treatments were applied to the as-quenched samples. These treatments were chosen in accordance with the DSC curves in order to shed light on the microstructural evolution and characterize the structure at different stages of their transformation: 1) Before the glass transition temperature; 2) At the beginning and at the end of the first crystallization event; 3) At the end of the second crystallization event. Therefore, the amorphous ribbons were annealed in an Ar atmosphere with a heating rate of 6 K min^{-1} at different temperatures: 673, 723, 773, 823, 873, 923, 973 K. Figure 3.6 shows the XRD diffractograms for the AB20 alloy annealed at the temperatures between 673 and 973 K. Annealing at 673 K, below the glass transition temperature, does not induce any crystallization and the diffractogram still shows the broad halo characteristic of the amorphous structure. However, the diffractograms at 723 and 773 K show the appearance of broad crystalline peaks, i.e. the formation of nanometer-sized crystals, coexisting with an amorphous structure. This crystallization corresponds to the first process with onset at T_{x1} (Figure 3.5). The presence of the crystalline phases is detected by XRD in samples annealed at temperatures below the T_{x1} value determined by DSC at 20 K min^{-1} (Table 3.2); this is because of the temperature shift, expected in glass crystallization, due to the different heating rates as the annealing protocols were performed at 6 K min^{-1}. These nanocrystalline peaks can be identified as a M$_3$B phase, where M stands for metal and could be any combination of Fe, Co or Ni as the phases Fe$_3$B, Ni$_3$B and Co$_3$B show compatible peaks with the observed ones. The JCPDS cards used for the identification are detailed in Table 3.3. It is worth to mention that the Ni and Co borides present an orthorhombic structure while the iron boride is tetragonal, showing the complexity of the crystalline phase that leads us to identify it as M$_3$B. Although the first crystallization products in many Fe-based metallic glasses

are typically BCC-Fe or the $Fe_{23}B_6$ phase, it is not unusual to find the precipitation of Fe_3B in some Fe-Si-B metallic glasses [38][39].

Phase	JCPDS card
Fe_2B	00-036-1332
Co_2B	01-075-1063
Ni_2B	01-082-1697
Fe_3B	00-039-1315
Co_3B	00-012-0443
Ni_3B	01-082-1699
Ni_2Si	01-073-2093

Table 3.3. JCPDS cards used for the identification of the crystalline peaks.

In the diffractograms of the samples annealed at 773 and 823 K an FCC phase begins to grow. Therefore, as a consequence of the first crystallization event, M_3B and FCC phase appear in the AB alloy. The M_3B phase is not stable as it disappears before the second crystallization, as can be seen in the diffractogram above 873 K. At these higher temperatures the main peak corresponds to the FCC structure and the smaller peaks can be clearly identified as M_2B. In a similar way than the M_3B phase, this boride can be identified with a Co_2B, a Fe_2B and a Ni_2B phase, all with tetragonal structure. Thus, the second crystallization event induces the formation of a M_2B phase while the FCC phase continues to grow.
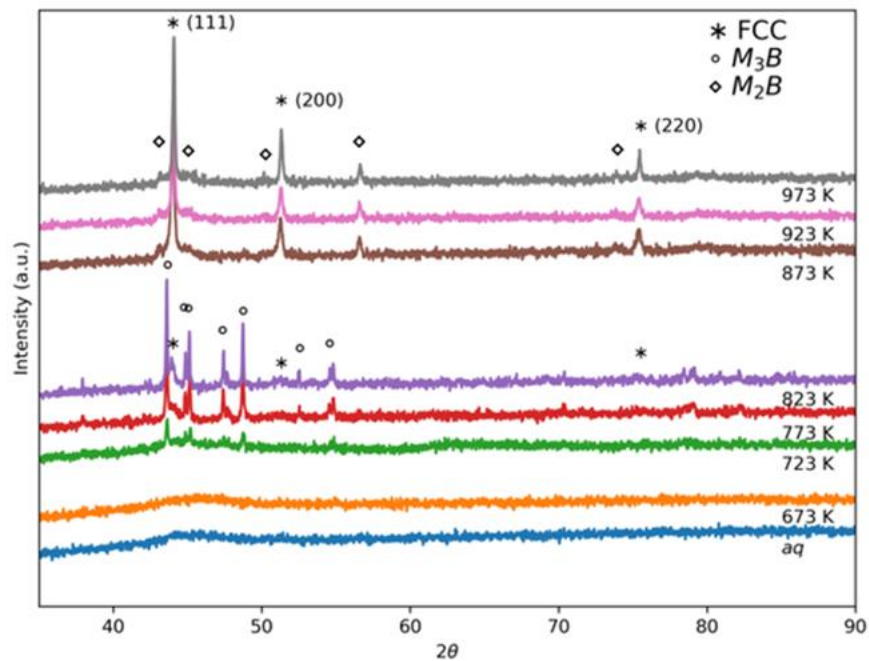
Figure 3.6 XRD patterns of $(FeCoCrNi)_{80}B_{20}$ alloy after annealing at different temperatures. The crystalline peaks are identified and correspond to an FCC phase and two borides.

The XRD diffractogram of AB10Si10 alloy annealed at the same temperatures is shown in figure 3.7. Below 773 K, the diffractogram shows completely amorphous samples and at 773 K some nanocrystals begin to form that can be assigned to a BCC phase together with a peak that can be ascribed to a $M_2(B,Si)$ phase, that remains visible at higher annealing temperatures including the fully crystallized sample. In this case, the Si can be incorporated in the structure of the boride but can also be present in a Ni_2Si phase. Annealing at 823 K yields the formation of an FCC phase together with a new boride, the $M_2(B,Si)$ phase that continues to grow at higher temperatures. At this temperature the peaks corresponding to the BCC phase are still present. Further annealing induces the disappearance of the BCC phase and the growth of the FCC and $M_2(B,Si)$ phases.
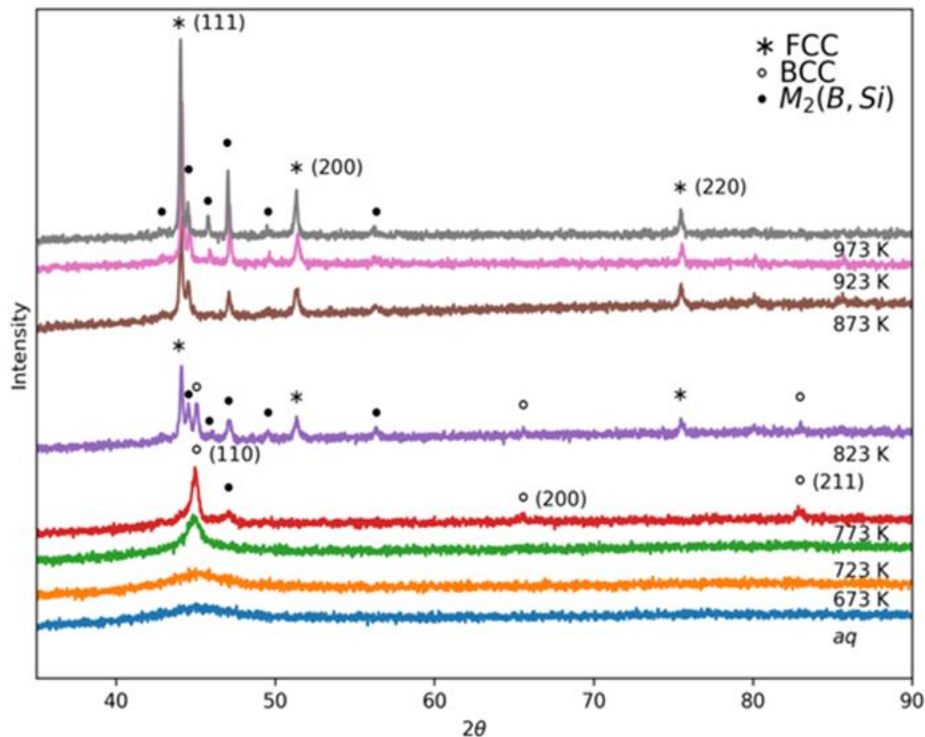
Figure 3.7 XRD patterns of $(FeCoCrNi)_{80}B_{10}Si_{10}$ alloy after annealing at different temperatures. The crystalline peaks are identified and correspond to an FCC, BCC and $M_2(B,Si)$ phase.

3.6. In-situ characterization of the crystallization

In the previous sections we presented the XRD patterns for the AB20 and AB10Si10 in the as-quenched state and annealed at different temperatures. The conventional laboratory XRD

technique is useful to give information about the phases that appear during each crystallization but give little information about the microstructural change with time. Thus, the structural properties of the ribbons were investigated by Synchrotron XRD at the MSPD beamline of ALBA Synchrotron. The X-ray synchrotron experiments were performed to measure in situ the crystallization process. The ribbon was irradiated with monochromatic radiation of λ= 0.4246 Å during a heating up from room temperature to 793 K at 20 K min^{-1} and held at this temperature for 2h and cooled down to room temperature at 100 K min^{-1}. Patterns were collected with a time acquisition of 1 s every 5 s using a Rayonix CCD detector. A diffraction without sample was taken at room temperature to have the background signal. The diffraction pattern at each temperature and the one of the backgrounds has been subtracted after intensity normalization. The diffraction was performed on the as-quenched ribbons; this may introduce some artefacts in the detected intensities of the Bragg reflections due to possible texture of the growing crystalline phases. However, the production of powder for the XRD analysis was discarded in order to avoid structural changes originated due to the milling process. The crystallization of the samples was analyzed in order to assess the role of Si and B on the crystallization path and characterize the emerging phases. According to the value of the ratio η = Si/B, and the DSC signal (Figure 3.5) we can distinguish two different regions. For $\eta \leq 1$, there are two crystallization events before 873 K, except for $\eta = 0$, where the second crystallization occurs above 873 K. For values of η larger than 1, there is only one crystallization event and, for $\eta = 2$ the crystals are already present in the as-quenched sample.

Figure 3.8 shows the crystallization for the case $\eta = 0$. The left panel shows the evolution of the intensity of the diffraction peaks with the temperature. The amorphous character of the as-quenched state is clearly seen by the low intensity of the broad peak between 10$^{\text{o}}$ and 15$^{\text{o}}$. This broad peak is replaced by sharp lines at temperatures close to 790 K signaling the nucleation and growth of the crystalline phases. The continuity of the lines indicates the existence of only one crystallization event while the increase in brightness of the lines shows the increase in volume fraction of the crystalline phases as the holding time at the maximum temperature increases. Therefore, with a holding time of 120 minutes at 793 K the second crystallization event detected by DSC is not reached in the X-ray diffractograms. The right panel of Fig. 3.8 shows the intensity versus the diffraction angle for selected temperatures from the initial amorphous state up to the final crystallized state.

37
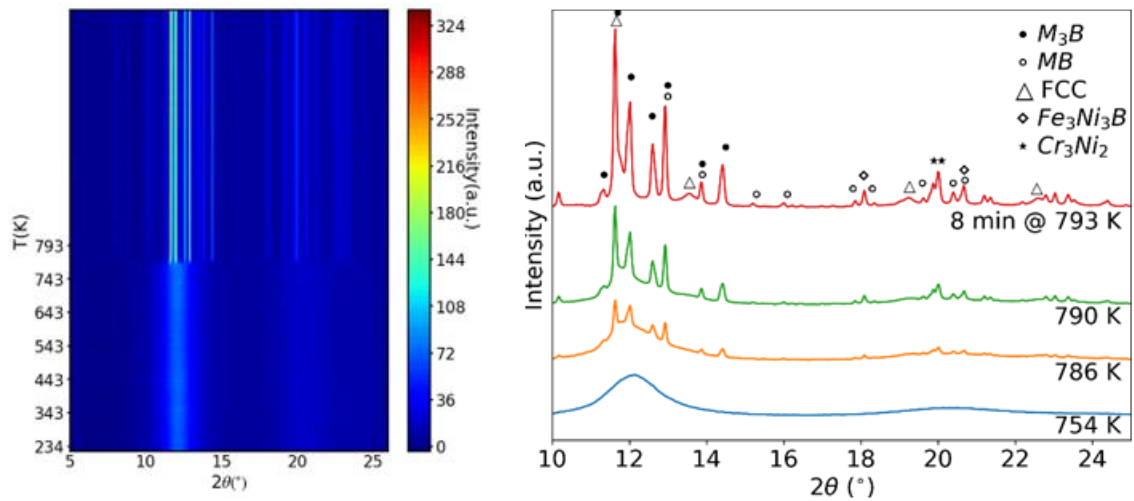
Figure 3.8 Crystallization of the AB20 sample ($\eta = 0$). Left panel: 2D map of the crystalline peaks showing their intensity (in a color scale) versus the diffraction angle 2θ (x axis) and the temperature T (y axis). Right panel: diffractograms of selected temperatures, from the initial amorphous phase to the highest temperature with phase identification.

The crystallization pattern is complex with multiple low intensity peaks. The main phases that can be identified are a solid solution with an FCC structure, the observed peaks correspond to (111), (200), (220) and (311) reflections, and two borides: Fe_3B and CoB. However, the intrinsic chemical disorder characteristic of high-entropy alloys tends to produce crystalline phases with a mixture of the main elements, thus it can be expected that the Fe_3B and CoB phase will contain other metal elements. This complexity of the crystalline phases is analyzed in detail by Mössbauer spectroscopy in the next section, showing that the Mössbauer spectra of the boride phases presented hyperfine parameters that differed from the ones corresponding to a pure Fe-boride phase, thus confirming the presence of other elements (Cr, Co or Ni) in the structure. The overall structure of the phases can be identified but, similarly to other works in this type of materials [38][39], the exact distribution of metal atoms inside the borides (or silicides, in the case of Si containing samples below) cannot be determined by the techniques used in this study. Besides the two identified borides, the three more intense peaks between 18 and 20° can be attributed to a more complex boride close to the Fe_3Ni_3B structure and to the intermetallic phase Cr_3Ni_2 although the identification of this latter phase is ambiguous. As explained before, in this experiment the second crystallization event observed by DSC cannot be reached, although in the previous section it was shown that increasing the temperature induces the formation of an M_2B phase and the disappearance of the M_3B phase. Thus, the first crystallization can be summarized in the following way:

$\eta = 0$: Amorphous $\rightarrow$ FCC + MB + M_3B + M_6B,

38

where M stands for metallic atoms.

The crystallization for the case $\eta = 1/3$ can be seen in figure 3.9. The 2D map clearly shows that two crystallizations processes take place in this composition. Firstly, the amorphous phase crystallizes in a BCC structure, likely a solid solution, with the peaks at 12°, 17° and 21° corresponding to the reflections (110), (200) and (211), respectively. After reaching the maximum temperature in the furnace, the second crystallization takes place with the nucleation and growth of an FCC structure together with two borides, CrFeB and FeB. There is no clear set of peaks that can be ascribed to a silicide phase, thus it is reasonable to assume that the small amount of Si atoms is present in the other crystalline phases or in a residual amorphous fraction. However, the small shoulder at around 11° together with the two more intense peaks could also be compatible with an $Fe_{4.9}Si_2B$ phase. The crystallization path for this case is, thus:

$\eta = 1/3$: Amorphous $\rightarrow$ BCC $\rightarrow$ BCC + FCC + MB(Si) + M_2B(Si),

where (Si) means the possible presence of this element in the structure, although not confirmed.
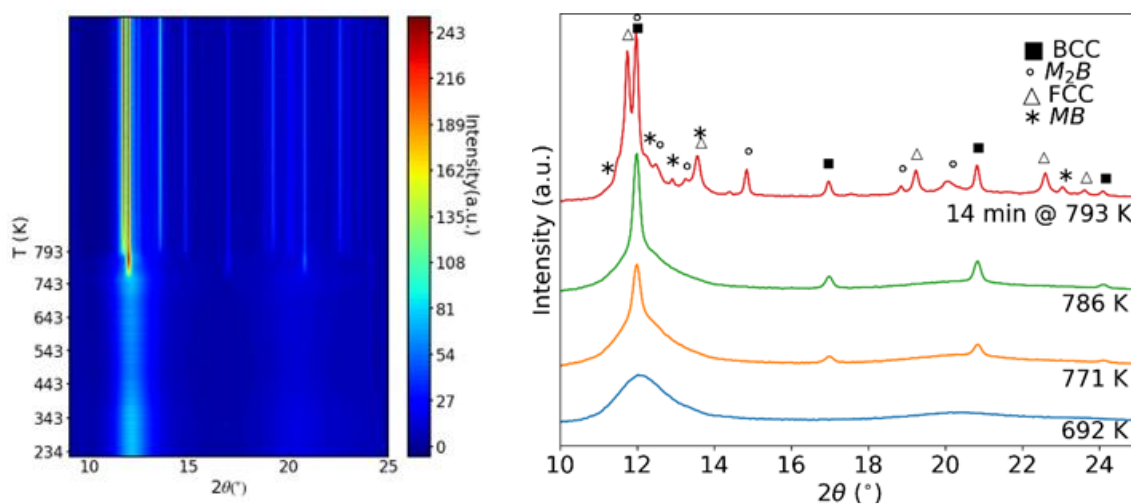
Figure 3.9 Crystallization of the AB15Si5 sample ($\eta = 1/3$). Left panel: 2D map of the crystalline peaks showing their intensity (in a color scale) versus the diffraction angle 2θ (x axis) and the temperature T (y axis). Right panel: diffractograms of selected temperatures from the initial amorphous phase to the highest temperature with phase identification.

The composition with $\eta = 1$ also presents a double crystallization reaction (see Figure 3.10). The first one takes places below 793 K and, like the previous composition, it can be ascribed to a solid solution with a BCC structure. However, contrary to $\eta = 1/3$, in the case of $\eta = 1$ there is a simultaneous crystallization of boride and silicide phases. In particular, peaks corresponding to Fe_2B, Ni_2Si and $Cr_{1.64}Fe_{0.35}B_{0.96}$ can be globally identified as phases with an $M_2(B,Si)$ structure, although some of the peaks can also be ascribed to a Co_2B phase. The second crystallization event maintains the previous phases and it induces the nucleation and

39

growth of a solid solution with an FCC structure, resulting in the following global crystallization path:
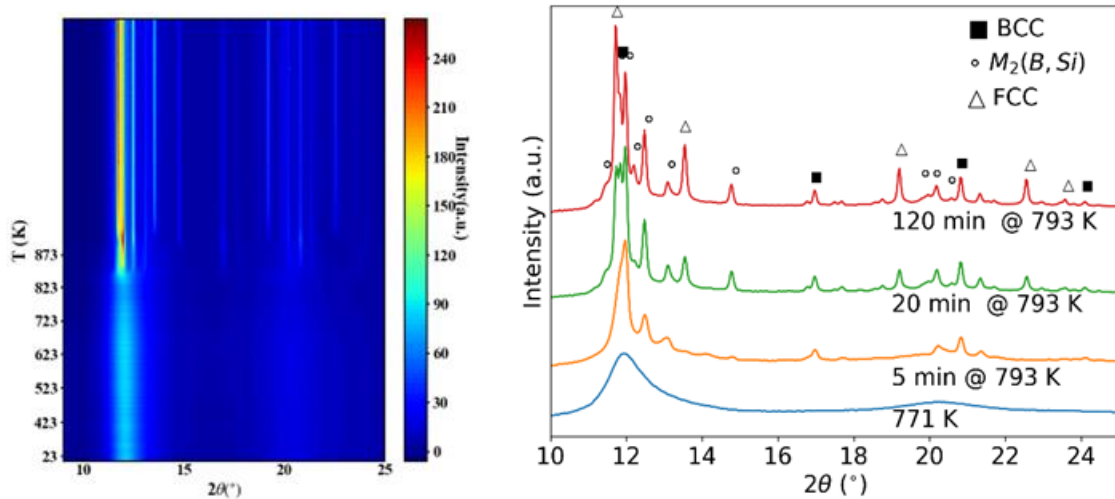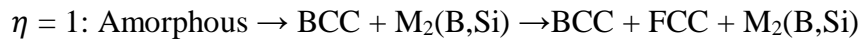
$\eta = 1$: Amorphous $\rightarrow$ BCC + M$_2$(B,Si) $\rightarrow$ BCC + FCC + M$_2$(B,Si)
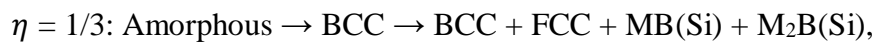

Figure3.10 Crystallization of the AB10Si10 sample ($\eta = 1$). Left panel: 2D map of the crystalline peaks showing their intensity (in a color scale) versus the diffraction angle 2θ (x axis) and the temperature T (y axis). Right panel: diffractograms of selected temperatures from the initial amorphous phase to the highest temperature with phase identification.

The last of the studied compositions with a completely amorphous structure in the as-quenched state corresponds to the case $\eta = 3/2$ and, contrary to the previous cases, it only presents one crystallization event in Figure 3.4. From the 2D map of figure 3.11 it could be seen that there are two different crystallization stages, however, looking at the selected diffractograms in the right-side panel it can be seen that all the peaks are already present at the beginning of the crystallization, although some of them are masked by the halo corresponding to the amorphous matrix in which the crystalline phases grow. In a similar way than in the case $\eta = 1$, the main existing crystalline phase is a solid solution with a BCC structure that grows simultaneously with borides and silicides. In particular, the peaks can be identified with Ni$_2$Si and Cr$_2$B phases. The peaks at around 11° and 17° are not identified but can be compatible with Fe$_5$Si$_3$ or Ni$_3$Si phases if some texture is assumed. Unlike the other compositions with less Si, in this case there is no growth of an FCC structure. What it can be observed, however, is that after a relatively short time at 793 K (approximately 30 minutes) the peaks corresponding to the BCC solid solution begin to decrease in intensity at the expenses of borides and silicides. Therefore, in this composition the crystallization path is more simple and can be summarized as follows:
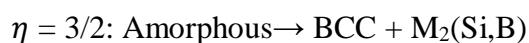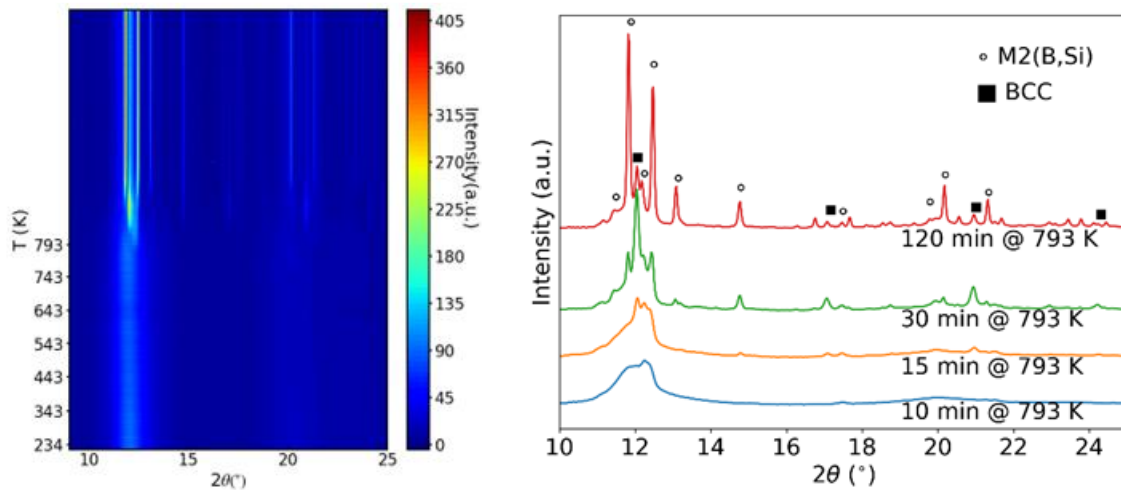
$\eta = 3/2$: Amorphous$\rightarrow$ BCC + M$_2$(Si,B)

Figure3.11 Crystallization of the AB10Si15 sample (η = 3/2). Left panel: 2D map of the crystalline peaks showing their intensity (in a color scale) versus the diffraction angle 2θ (x axis) and the temperature T (y axis). Right panel: diffractograms of selected times after reaching the maximum temperature in the hot stage.

The last of the studied compositions corresponds to the case η = 2, which is partially crystalline in the as-quenched state, although the majority of the as-quenched structure remains amorphous (see Figure 3.12). Despite this double character of the structure, the study of the crystalline phases is interesting in order to have a better picture of the effect of Si in the crystallization path of this family of HEMG. The crystals present in the as-quenched state can be identified as a solid solution with a BCC structure that continuously grows when increasing temperature. After the full treatment of the sample (120 minutes at 793 K) besides the BCC phase, several peaks appear that are compatible with a Ni_2Si phase. There are no clear peaks corresponding to borides, although the peaks at 11.4° and 12.2° are consistent with a Ni_2B phase. Thus, the crystallization path is:
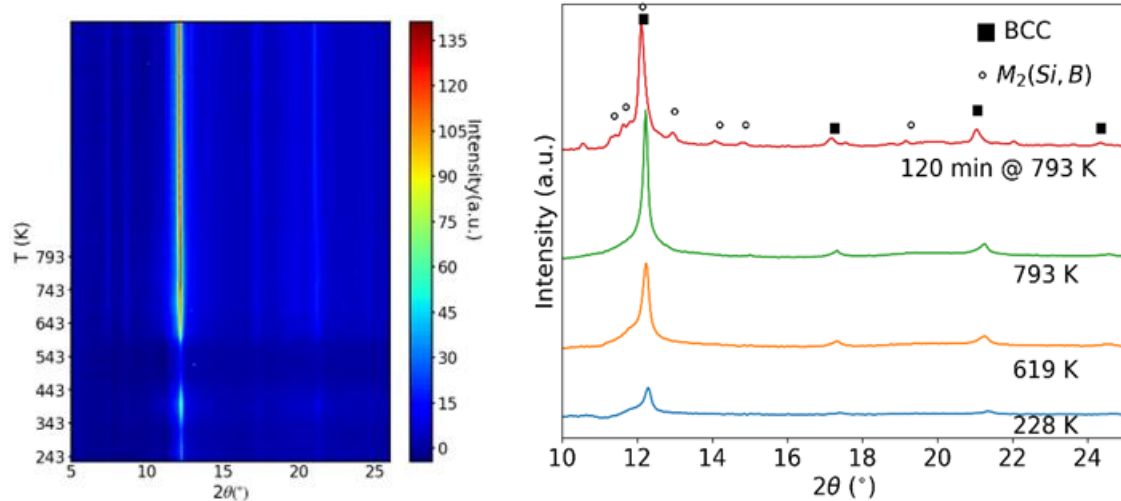
η = 2: Amorphous + BCC → BCC + M_2(Si, B).

41

Figure3.12 Crystallization of the AB10Si20 sample ($\eta = 2$). Left panel: 2D map of the crystalline peaks showing their intensity (in a color scale) versus the diffraction angle 2θ (x axis) and the temperature T (y axis). Right panel: diffractograms of selected temperatures from the initial partially crystalline phase to the highest temperature with phase identification.

Summarizing, the analyzed crystallization paths show a clear trend with the Si content. When there is no Si present in the HEMG ($\eta = 0$) the main phase is an FCC structure with a complex combination of borides, including a metastable M_3B phase together with other borides and some intermetallic phase. Adding Si ($\eta > 0$) changes the structure of the principal crystalline phase, that now is BCC instead of FCC. Moreover, the first borides to crystallize are no longer the metastable M_3B but the stable M_2B. In the compositions with two crystallization events ($\eta \leq 1$), the second crystallization induces the growth of the FCC structure that coexists with the BCC phase. In the compositions with low Si content ($\eta = 1/3$), there is also the formation of some MB phase. Increasing the Si content ($\eta = 1$) implies the crystallization of only M_2B and M_2Si phases. Finally, for the compositions with the highest Si content ($\eta = 3/2$ and $\eta = 2$) the second crystallization disappears obtaining a microstructure composed of a BCC solid solution and $M_2(B, Si)$ crystals.

3.7. Characterization by Mössbauer spectroscopy

The Mössbauer spectra of the studied samples are shown in Figures 3.13 and 3.16 for AB and ABSi alloys respectively. The as-quenched ones and the annealed ones up to 673 K show a typical wide doublet characteristic of paramagnetic amorphous phases. To consider the structural disorder, these spectra have been fitted using a distribution of quadrupole splittings (Δ) plotted in the insets of the figures. At 723 K the crystallization begins being noticed in both

42

samples although, as already said, the crystallization path and products are different. For the AB alloy, a sextet of a ferromagnetic phase appears with a value of the hyperfine magnetic field (BHF) of 24.4 T. This phase grows in the sample annealed at 773 K, diminishes at 823 K and completely disappears at 873 K.
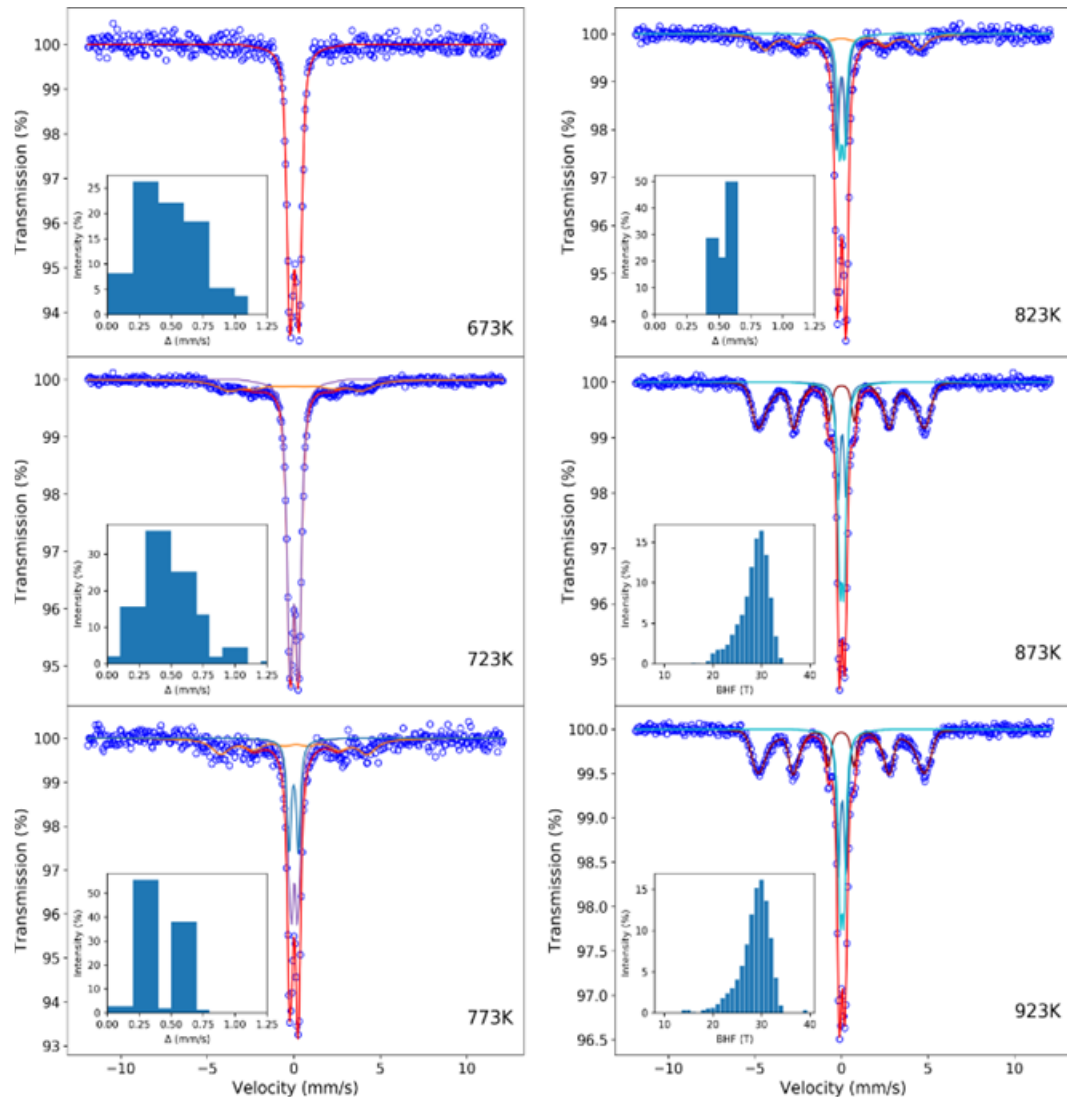
Figure 3.13 Experimental Mössbauer spectra (blue dots) and their fits (red lines) for the $(FeCoCrNi)_{80}B_{20}$ alloy at six different representative stages of the crystallization process. In colored lines there are the subspectra fitted for the different phases (purple for the amorphous phase, blue and cyan for the FCC phase and orange and dark red for the borides). The insets show the distribution of quadrupole splittings (for the as-quenched samples) or hyperfine magnetic fields (for the annealed ones) needed for the fitting.

Therefore, taking into account the XRD results and the hyperfine values (with $\Delta = 0.09(8)$ mm s^{-1} and isomer shift $\delta = 0.03(4)$ mm s^{-1}, where the magnitude in parenthesis corresponds to the standard deviation obtained from the fitting software[28] this ferromagnetic phase can be ascribed to a M_3B structure. The sextet corresponding to the M_3B phase has a large width (around 1.2 mm s^{-1}) to take into account the different metals (Fe, Co or Ni) that can enter in

43

the structure and, thus, change the BHF value. We cannot use a distribution of hyperfine fields due to the fact that the available version of the fitting program does not allow using simultaneously a distribution of quadrupole splittings and BHFs. Moreover, at 773 K, besides the amorphous and the boride phase, a new paramagnetic doublet appears that corresponds to the FCC phase (with $\Delta = 0.54(1)$ mm s^{-1} and $\delta = 0.00(3)$ mm s^{-1}). At 823 K there is still a remnant of the amorphous phase fitted with a distribution of quadrupole splittings and the paramagnetic crystalline phase can be fitted using two doublets with very different values of the quadrupole splitting ($\Delta = 0.57$ mm s^{-1} and $\Delta = 0.27(2)$ mm s^{-1}). The first doublet has been fitted with fixed hyperfine parameters in order to disentangle its contribution from the one corresponding to the amorphous phase with similar values of the hyperfine parameters. The two doublets for the crystalline phase are necessary for two different reasons. On the one hand, at 823 K are needed to keep the amount of amorphous phase below its amount at 773 K as it would be unphysical that the amorphous phase grows with the annealing temperature. On the other hand, at higher annealing temperatures, they are necessary to be able to account for the different intensities of the two absorption peaks in the central part of the spectrum. As in the XRD diffractograms only one FCC structure can be identified, this result indicates that the crystalline structure of the FCC phase presents a distribution of different chemical environs surrounding the Fe atoms. This is different than what is observed in the FCC phase of the HEA FeCoCrNi (alloy A in this work) shown in Figure 3.14.
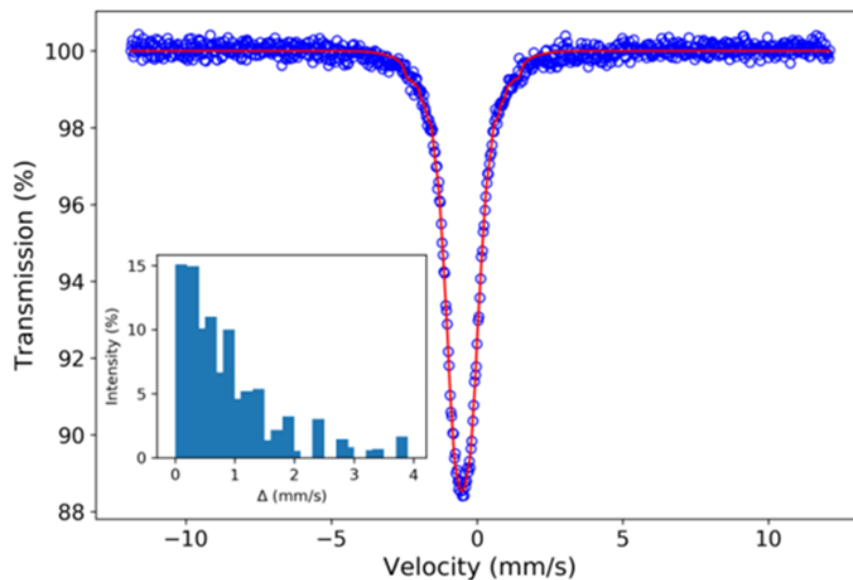
Figure 3.14 Mössbauer spectrum of the as-quenched FeCoCrNi HEA in ribbon form (blue dots) together with the best fitting (red line) to the experimental data. The inset shows the distribution of quadrupole splittings.

44

In this case all the elements are randomly distributed in the structure and the Mössbauer spectrum cannot be fitted with two doublets. It is then necessary to use a distribution of quadrupole splittings to consider the random chemical ordering surrounding the Fe nuclei and characteristic of HEA alloys. The inset of Figure 3.14 shows this spread distribution over a wide range of Δ values, whereas the AB alloy annealed at 823 K only have two main contributions. From 873 K to 973 K the spectra are similar, with two doublets for the FCC phase (with similar hyperfine parameters than the doublets at 823 K) and one BHF distribution for the ferromagnetic phase with an average hyperfine field of 28.6 T and zero quadrupole splitting and isomer shift. According to XRD results, this ferromagnetic phase can be associated to a M_2B phase. Although the M_3B and M_2B phases can present several subspectra according to the different positions that the Fe atoms can occupy in the structure and the number and types of elements surrounding it, such a detailed fitting model has not yielded good results and we opted for a general approach in which we are not able to precisely identify the effect of Co, Cr and Ni on the structure but we can identify and quantify the several phases that appear.

Figure 3.15 shows the evolution of the at% of Fe atoms in each phase obtained from the fitting of the Mössbauer spectra. These at% have an error of $\pm$ 0.5 %, as estimated from the fitting software. It is clearly shown how the amorphous phase firstly decomposes into an FCC plus a M_3B phases that coexist until 873 K, and at this temperature part of the FCC phase and the M_3B phase decomposes into a M_2B phase. The inset of the figure shows the evolution of the total ferromagnetic and paramagnetic phases demonstrating that in the fully crystallized sample there is the same amount of both magnetic orderings.
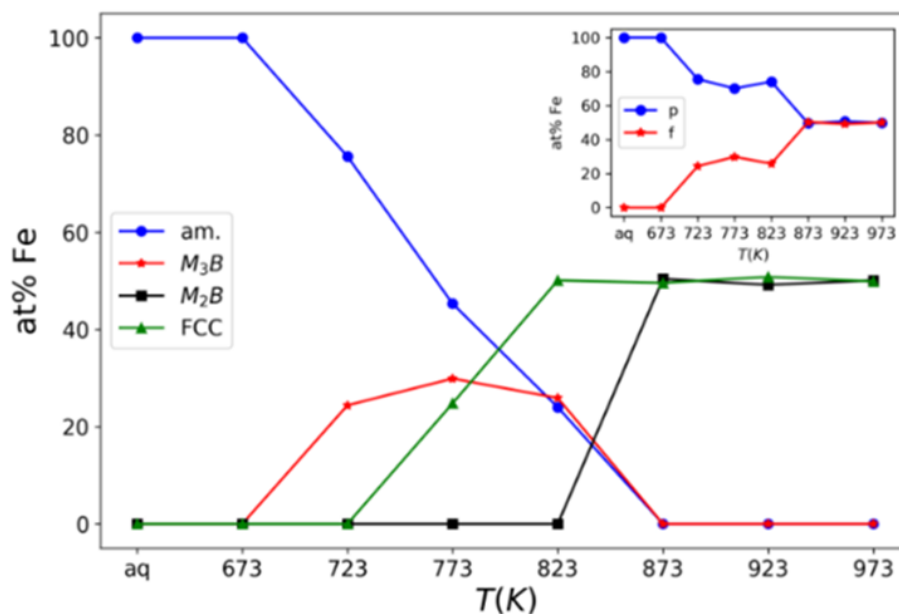
Figure 3.15 Variation of the at% (with an error of ±0.5 %, smaller than the symbol) of the different phases of the $(FeCoCrNi)_{80}B_{20}$ alloy as a function of the annealed temperature calculated from the analysis of the Mössbauer spectra. The inset shows in blue (red) the atomic percentage of the total paramagnetic (ferromagnetic) phases as a function of the annealed temperature.

For the ABSi alloy the fitting of the spectra (Figure 3.16) can be performed similarly as in the previous AB samples, although some of the crystalline phases that appear are different.
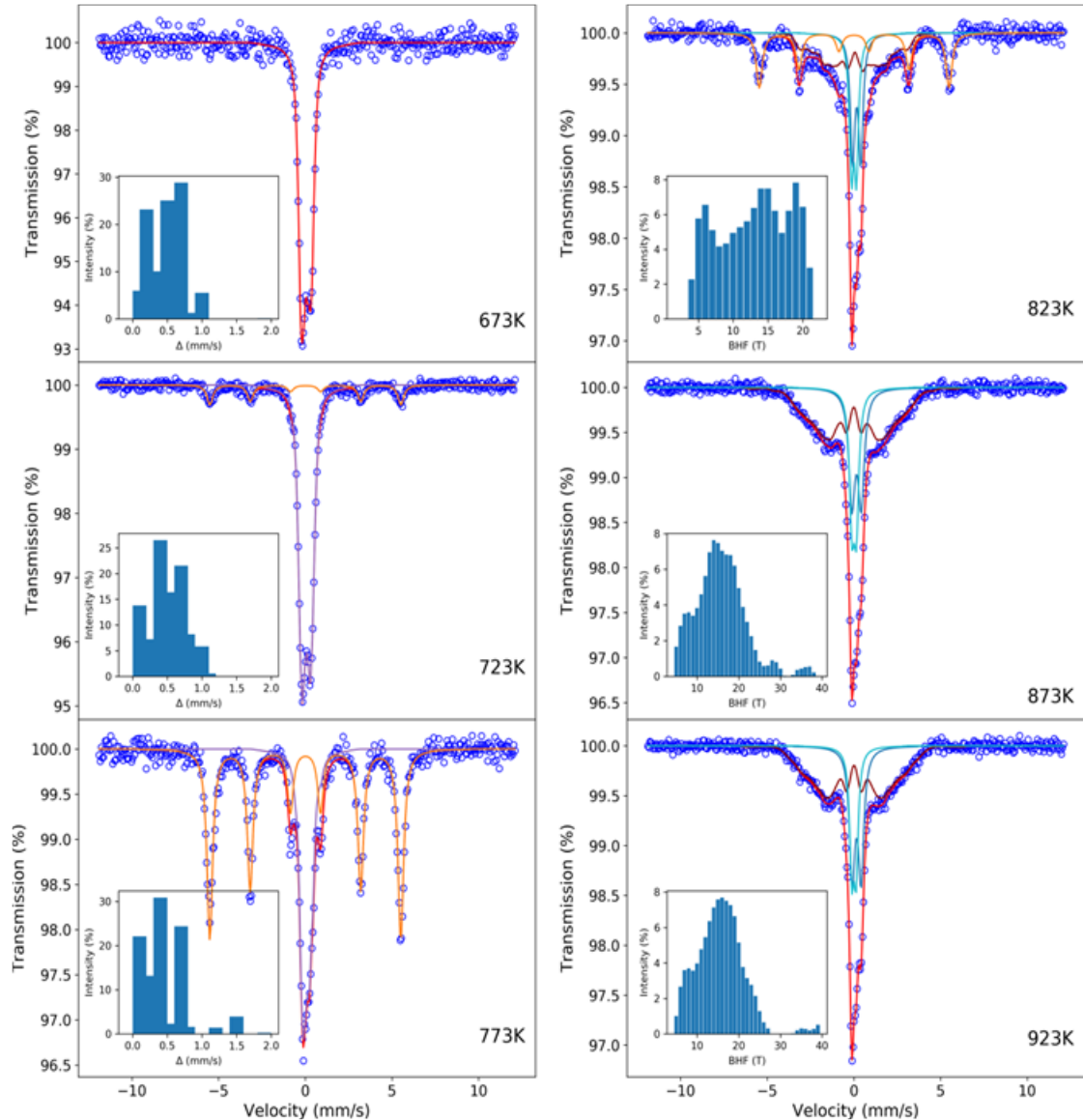
Figure 3.16 Experimental Mössbauer spectra (blue dots) and their fits (red lines) for the $(FeCoCrNi)_{80}B_{10}Si_{10}$ alloy at all the stages of the crystallization process except the fully crystalline one. In colored lines there are the subspectra fitted for the different phases (purple for the amorphous phase, blue and cyan for the FCC phase and orange and dark red for the BCC and borides). The insets show the distribution of quadrupole splittings (from 673 to 773 K) or hyperfine magnetic fields (from 823 to 923 K) needed for the fitting

In this case, the first crystallization at 723 K corresponds to a phase that can be ascribed to a BCC phase close to BCC-Fe (with hyperfine field value of 34.1 T and zero quadrupole splitting and isomer shift) and that disappears at 873 K. The appearance of the FCC phase is

delayed until 823 K, where the two doublets with similar hyperfine parameters than in the AB samples appear together with the formation of a new boride phase that would correspond to $M_2(B,Si)$ (with hyperfine field value around 15 T and zero quadrupole splitting and isomer shift). Thus, in this composition we also have the double distribution of environs in the FCC phase. The boride phase was fitted using a BHF distribution in an analogous way than the M_2B phase in the AB alloy. However, the presence of Si in this phase diminishes the average BHF in the distribution if compared with the M_2B phase. It is worth to mention that at 823 K the BCC phase has been fitted using a discrete wide sextet while the borides have been fitted with a distribution of hyperfine fields. This has been done in this way in order to be able to differentiate between the two ferromagnetic phases and keep track of their atomic percentages during the transformation. The evolution of all the phases is presented in Figure 3.17 with the inset showing that the fully crystalline sample contains more ferromagnetic (~64 at%) than paramagnetic phases (~36 at%).
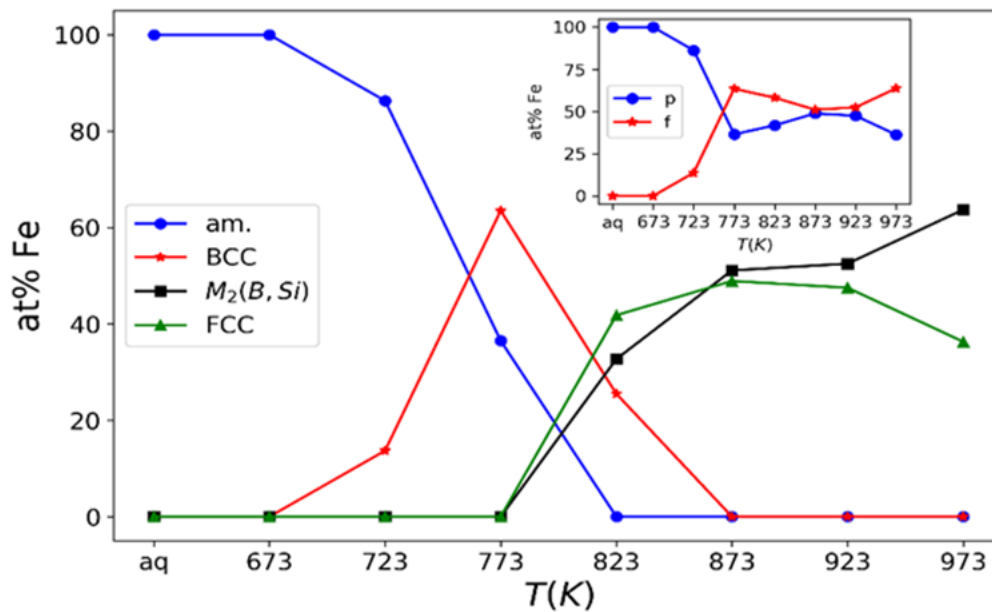
Figure 3.17 Variation of the at% (with an error of ±0.5 %, smaller than the symbol) of the different phases of the $(FeCoCrNi)_{80}B_{10}Si_{10}$ alloy as a function of the annealed temperature calculated from the analysis of the Mössbauer spectra. The inset shows in blue (red) the atomic percentage of the total paramagnetic (ferromagnetic) phases as a function of the annealed temperature.

Therefore, the substitution of B by Si, besides changing the crystallization products, also favors the presence of ferromagnetic components. The crystallization path of both HEMGs can be summarized in the following way:

AB amorphous → M_3B → FCC + M_3B → FCC + M_2B

47

ABSi amorphous $\rightarrow$ BCC + M_2(B,Si) $\rightarrow$ FCC + BCC + M_2(B,Si) $\rightarrow$ FCC + M_2(B,Si)

3.8. Effect of annealing on the particle size distribution

The annealing temperature is shown to have a significant influence on the particle size distribution and morphology of the ribbons. The SEM images of the interior of the AB20 and AB10Si10 ribbons at room temperature and after annealing at different temperature up to 973K are shown in figure 3.18. The first two figures on top show the AB20 and AB10Si10 as-prepared ribbons at room temperature with a smooth and homogeneous cross section characteristic of the amorphous materials. Although, as detected by Mössbauer, the crystallization process begins at 723 K, the formed crystals are too small to be noticed in the SEM images. In samples annealed at 823 K a clear crystalline structure, uniformly distributed, is observed with a typical grain size that continuously grows from 923 K to 973 K. Comparing the last rows of Figure 3.16 it can be concluded that the presence of Si hinders the growth of the grains resulting in a sample with a smaller crystals compared to the AB sample.
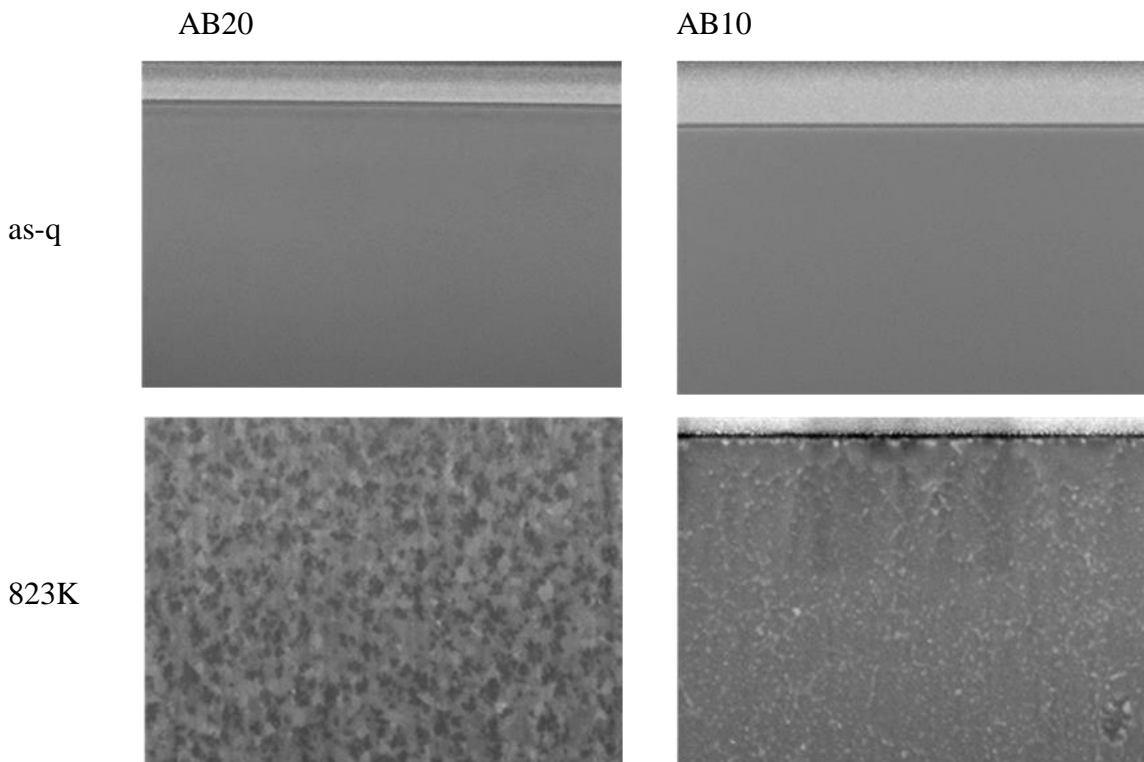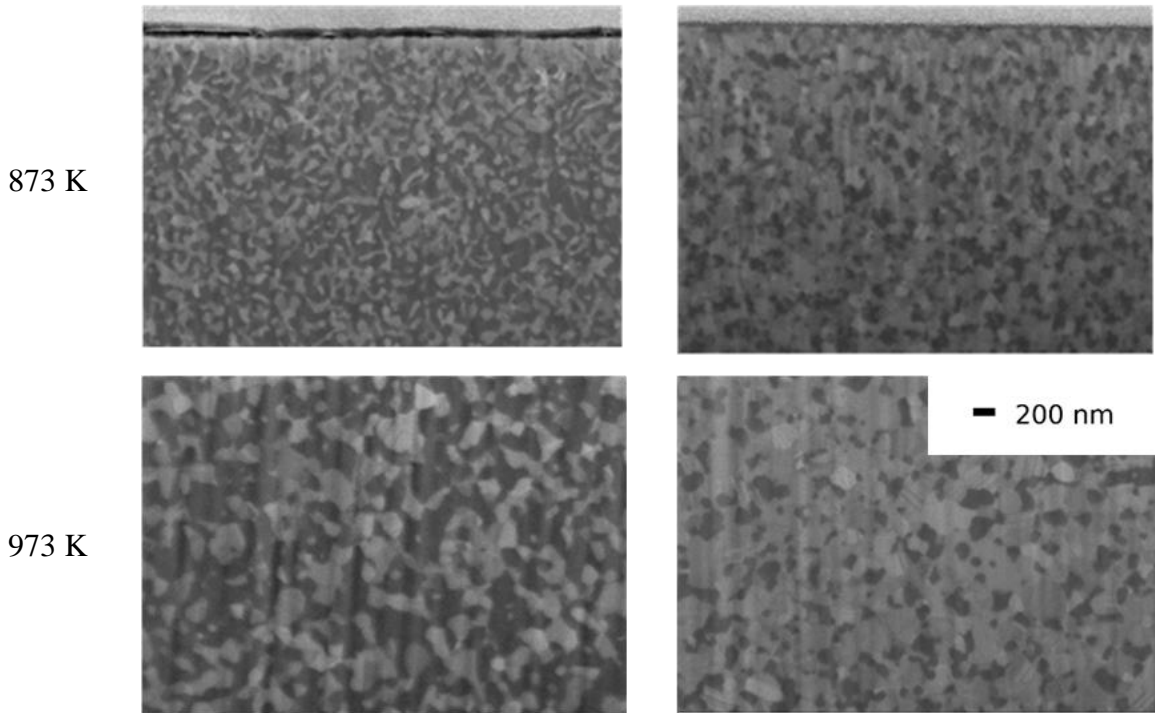
Figure 3.18 SEM images of the HEMGs alloys (FeCoCrNi)80B20 (left column) and (FeCoCrNi)80B10Si10 (right column) in their as-quenched state (first row) and after annealing at 823, 873 and 973 K.

To further study the effect of Si in the microstructure, the grain size distribution of both alloys as a function of the annealing temperature was computed from the SEM images of Figure 3.18. The average grain size was calculated by ImageJ software using the following procedure: i) setting the scale according to scale of the photo; ii) measuring each grain 5 times from different directions and iii) taking average of the length for each grain. The AB alloy (Figure 3.19 top) grows from ~69 nm at 823 K to ~185 nm at 973 K. In all the temperatures the width of the distribution is large, especially after 823 K, indicating a microstructure without a well-defined characteristic length. In contrast, Figure 3.19 bottom shows the grain size distribution for the ABSi alloy, with a lower average grain size that grows from ~37 nm at 823 K to ~135 nm at 973 K and with a narrower width below 973 K. Therefore, the presence of Si instead of B in the microstructure not only reduces almost to a half the average size of the crystals but also produces a more uniform microstructure.
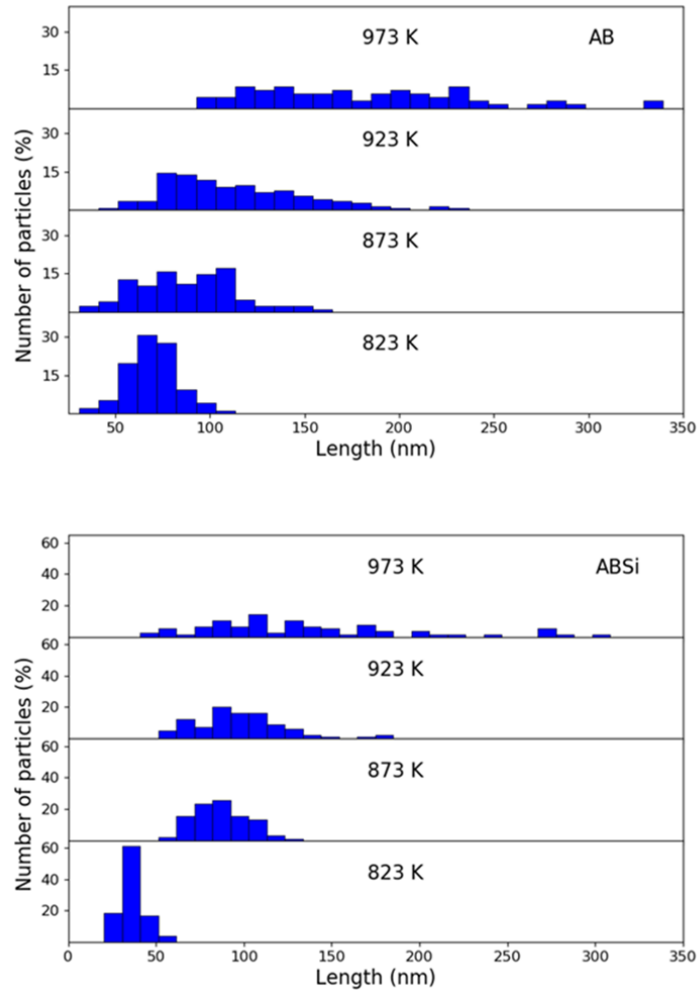
49

Figure 3.19 Distribution of grain sizes in $(FeCoCrNi)_{80}B_{20}$ (top) and $(FeCoCrNi)_{80}B_{10}Si_{10}$ (bottom) after annealing at different temperatures.

3.9. Discussion

In this chapter, we have presented two different alloys and in each section their properties and the effect of the annealing and the elemental composition on them has been discussed. In the first step, $(FeCoCrNi)_{80}B_{20}$ and $(FeCoCrNi)_{80}B_{10}Si_{10}$ were produced and it has been shown that both of them followed similar thermal behavior but the partial substitution of B with Si causes the increase of both the glass transition temperature and the temperature of the first crystallization event while it reduces the temperature of the second crystallization. Moreover, it shows a slight increase in the supercooled liquid region ($\varDelta T_x$) after adding Si, therefore this element increases the thermal stability of the alloy. Regarding the structure of these alloys at room temperature, it has been shown that both, AB and ABSi were amorphous at room temperature. By annealing the AB sample, the FCC and M_3B phases appeared as a first

crystallization product at 823K whereas M_3B was not a stable phase and it disappeared before the second crystallization. After the second crystallization, the FCC phase still grows beside the formation of M_2B and this M could correspond to the different metals (Fe,Co,Ni). On the other side, for the ABSi alloy, the x-ray diffraction pattern showed a completely amorphous phase below 773K and by increasing the temperature the nucleation and growth of some nanocrystals like BCC and $M_2(B,Si)$ begin. By increasing the temperature to above 823K the formation of FCC and some new boride phase started. At higher temperature, the BCC phase is still there and the growth of FCC and $M_2(B,Si)$ continued.

An addition of 10 at% of B and 15 at% of Si to the base composition (equiatomic FeCoCrNi) maximize the glass forming ability and thermal stability of the amorphous phase. Also we studied the crystallization path of other compositions in this new family of high entropy metallic glasses (AB20, AB10Si10, AB10Si20, AB10Si15 and AB15Si5) characterizing their structure by in-situ X-ray diffraction at ALBA synchrotron and we reach the following conclusions. For Si/B ratios lower or equal than one the alloys present two crystallization events while for higher values of this ratio there is only one crystallization peak. Moreover, as the amount of Si increases the main crystalline phase changes from FCC to BCC.

In the last section of the chapter we discussed the microstructure and the effect of the heat treatment on it. From a microstructural point of view there is a change in the size of nanocrystalline particles in both alloys. According to our study, in the AB alloy the average grain size at 823K was ~ 69 nm and by increasing the annealing temperature it will reach to ~185 nm at 973 K while in the ABSi alloy, the average grain size grows from ~ 37 nm at 823K to ~135 nm at 973K. Eventually, the replacement of part of B with Si causes the microstructure to reduce the size as well as to produce a more uniform microstructure.

CHAPTER 4. MECHANICAL CHARACTERIZATION

The aim of this chapter is to study the mechanical properties and the deformation process of the produced alloys by means of nanoindentation. This technique offers many advantages and it requires only a small volume of test material [40]. Several mechanical properties related to the elastic and plastic deformation response can be assessed from the load-displacement (P-h) curve recorded during the nanoindentation process [41] that allow us to determine the hardness (H), the reduced Young's modulus (E_r), the plastic energy (U_p), the elastic energy (U_{el}), the wear resistance (H/E_r) and the elastic recovery (U_{el}/U_{tot}). In this chapter, of all the produced compositions we selected the ones with best glass-forming ability and the base alloy, the latter to serve us as a reference. These compositions are: A, AB20, AB10Si10, AB10Si20, AB15Si5 and AB10Si15, emphasized with a circle in Figure 3.3 of the previous chapter.

4.1. Nanoindentation

The mechanical properties of the as quenched and the annealed samples are obtained by the nanoindentation equipment described in section 2.7. Figure 4.1 (top) shows the load-displacement curves of all the samples in the as-quenched state, including composition A for reference. In addition to the different penetration depths and corresponding hardnesses, the slope of the unloading part of the indentation curves, related to the contact stiffness, indicates a different value of the reduced Young's modulus. From these curves the hardness and E_r can be calculated and the values are shown in Figure 4.1 (bottom) and Table 4.1.

Figure 4.1 (bottom) shows the change of these magnitudes as a function of the composition for all the as-quenched samples. The large increase in hardness from the base composition ($\sim$ 4 GPa) to the B and Si containing alloys ($\sim$14-18 GPa) can be explained by the strong nature of the (B,Si)-M interatomic bonds and the change from an FCC crystalline to an amorphous structure, where the absence of long-range order and crystalline defects increases the resistance to plastic deformation. There is no clear trend in the values of H or E_r as a function of composition, all amorphous samples showing outstandingly high hardness values, three times as hard as stainless steels [42].

53
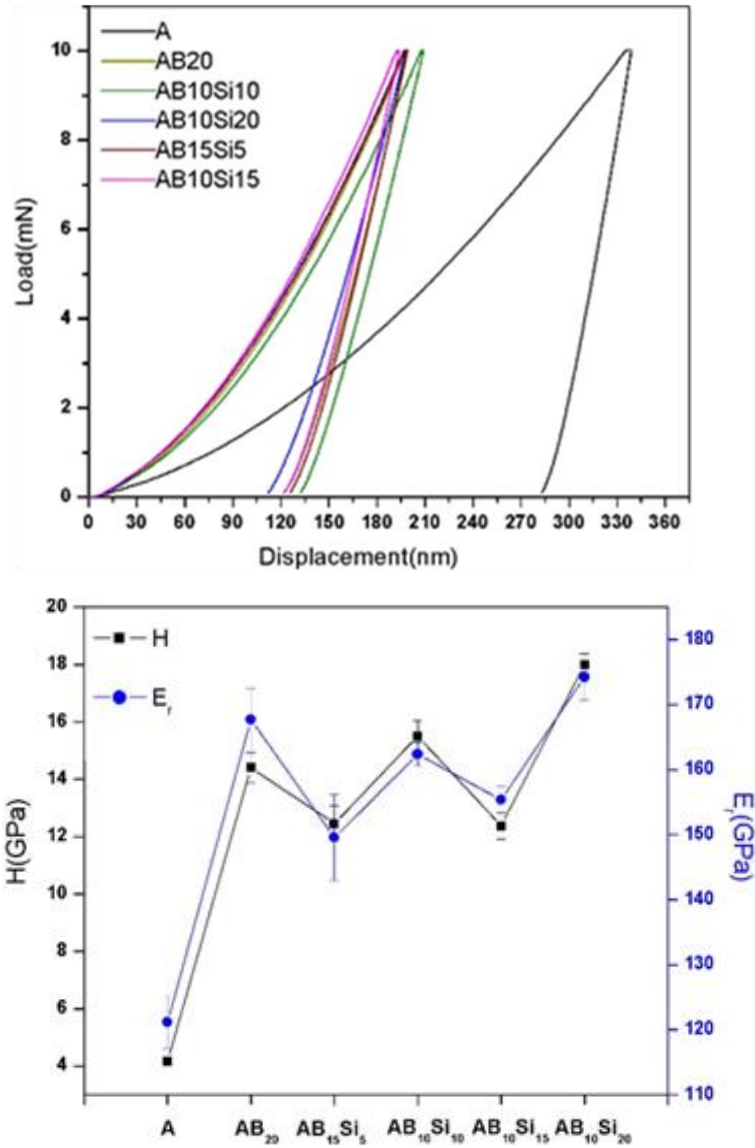
Figure 4.1 Load-displacement nanoindentation curves (top) and variation of hardness (H) and reduced Young's modulus (E_r) (bottom) for as quenched ribbons at room temperature.

However, there is a clear increase of these magnitudes for AB10Si20, i.e. the alloy that has the major content of B and Si and, in addition, contains some nanocrystals embedded in its amorphous structure as discussed in the previous section. It is expected that the elastic properties of a material are related to its atomic bonding in a way that compositions with stronger bonds exhibit higher values of E_r [43]. There are two possible contributions to the maximum values of H and E_r in the AB10Si20 alloy. On the one hand, the large amount of Si creates stronger covalent bonds between this element and the metallic elements. On the other hand, the interplay between the amorphous matrix and the nanocrystalline inclusions can enhance the mechanical properties [35][44].

Samples	H (GPa)	E_r (GPa)	U_p (nJ)	U_{el} (nJ)	U_{tot} (nJ)	H/E_r	U_{el}/U_{tot}
A	4.15 ± 0.12	121.9 ± 4.1	1.04 ± 0.029	0.247 ± 0.008	1.28 ± 0.04	0.034 ± 0.002	0.190 ± 0.011
AB20	14.40 ± 0.53	167.1 ± 4.8	0.353 ± 0.002	0.343 ± 0.002	0.690 ± 0.004	0.086 ± 0.005	0.490 ± 0.005
AB15Si5	12.50 ± 0.46	149.6 ± 6.5	0.405 ± 0.006	0.351 ± 0.002	0.750 ± 0.008	0.084 ± 0.006	0.460 ± 0.007
AB10Si10	15.50 ± 0.54	162.3 ± 1.8	0.367 ± 0.007	0.356 ± 0.003	0.72 ± 0.01	0.09 ± 0.003	0.49 ± 0.01
AB10Si15	12.6 ± 0.4	155.4 ± 2.1	0.401 ± 0.002	0.345 ± 0.001	0.740 ±0.003	0.081 ± 0.003	0.46 ± 0.007
AB10Si20	17.7 ± 0.7	176.3 ± 3.6	0.279 ± 0.020	0.361 ± 0.002	0.64 ± 0.03	0.100 ± 0.005	0.56 ± 0.025

Table 4.1. Hardness (H), reduced Young's modulus (E_r), plastic energy (U_p), elastic energy (U_{el}), wear resistance (H/E_r) and elastic recovery (U_{el}/U_{tot}) measured by nanoindentation.

We can compare the hardness and elastic modulus values of the as-quenched alloys studied here with other high-entropy alloys of similar compositions probed also by nanoindentation [45][46]. In these references the maximum loads were between 10 and 30 mN, similar to the ones applied in the present work, although some differences could be expected due to the measures done at a strain rates of 5×10^{-2} s^{-1} in the case of ref. [45]. Figure 4.2 displays the values of the Young's modulus versus hardness for several alloys that also contain Fe, Co and Cr in the base composition and additions of other elements like, Cu, Si or Al to tailor their properties. From this figure, it is clear that the micro alloying with Al and the incorporation of Mn in the base composition are beneficial for the elastic modulus but it produces only a moderate increase in the hardness. All these compositions present a diversity of structures and microstructures depending on the particular composition and alloying element and comprise FCC, BCC, mixture of BCC and FCC and also a mixture of FCC and HCP phases. The composition with the highest elastic modulus is the Al$_3$(FeCoCrNiCu) that consists of a BCC phase in a dendritic configuration. Accordingly, it could be concluded that more than the particular crystalline configuration of the alloy, the most determinant factor that contributes to its mechanical behavior is the microstructural configuration of the main phase. The use of important amounts of B and/or Si significantly improves (almost doubles) the hardness, while keeping the elastic modulus almost constant. This increase of hardness opens a new route to design new high-entropy alloys with improved properties seeking for a combination of

constituent elements capable to amorphize the structure or induce a change in the microstructure.
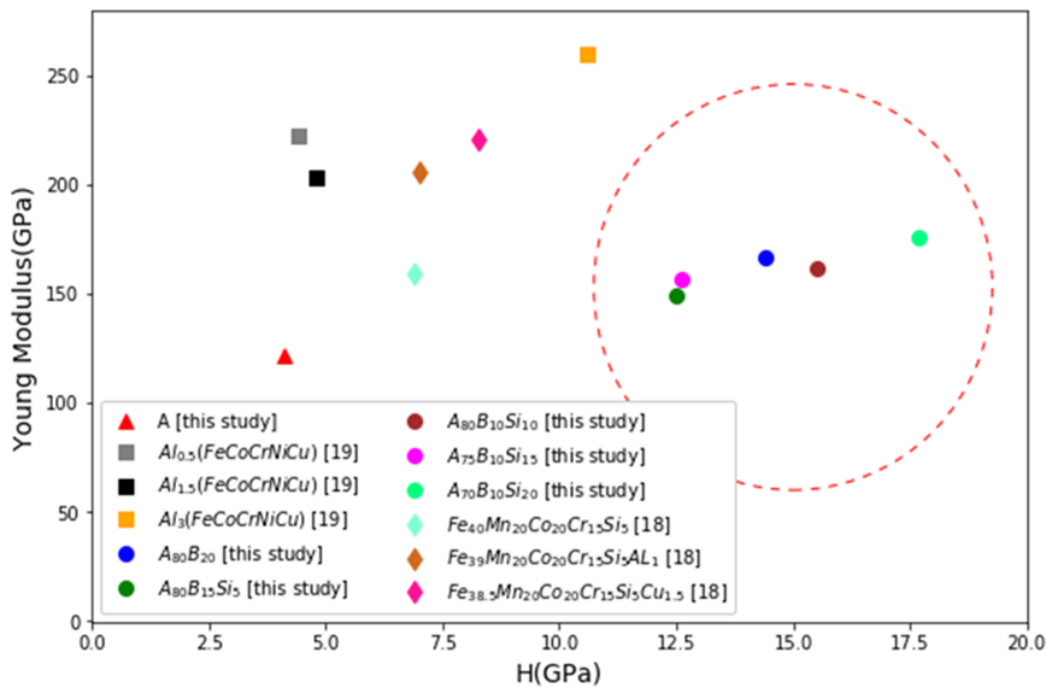
Figure 4.2 Comparison of Young modulus and hardness for several compositions [45][46]. The circle indicates the compositions investigated in this study.

In order to study the effect of nanocrystallization on the mechanical properties, two of the compositions, AB20 and AB10Si10, were selected and nanoindentation experiments were performed at different stages of their crystallization process. These two alloys have the same ratio of metallic and metalloid elements but different crystallization routes, forming FCC or BCC crystals as described in the previous chapter. Specifically, the samples were annealed up to different temperatures to examine their properties as a function of their degree of crystallization. The set of annealing temperatures spans from below the glass transition up to full crystallization. It is well known that below T_g a heat treatment causes changes in the physical and mechanical properties of glasses due to structural relaxation. The decrease of excess free volume during this process usually causes a reduction of atomic mobility an increase of Young's modulus and hardness, and a loss of ductility of metallic glasses [43][40][47][41].
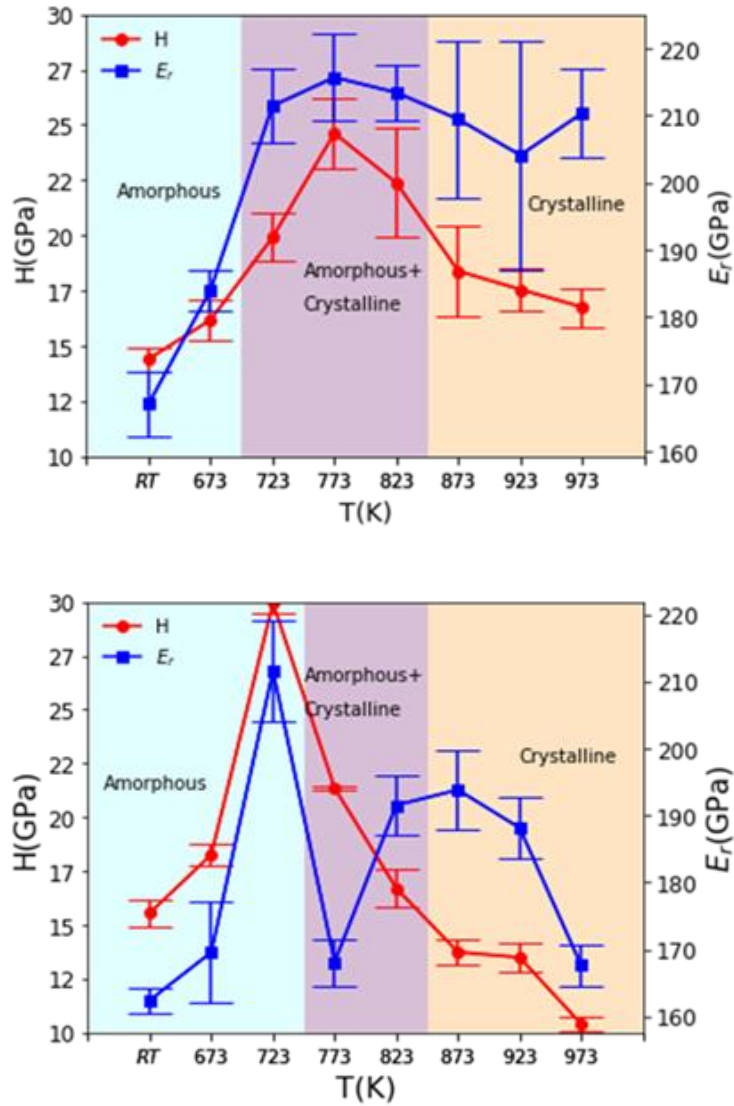
Figure 4.3 Variation of hardness (H) and reduced elastic modulus (E_r) as a function of annealing temperature for AB20 (top) and AB10Si10 (bottom).

The results of H and E_r for the two compositions are shown in Figure 4.3 and are detailed in Table 4.2. Figure 4.3 (top), corresponding to the Si-free material, shows a progressive increase of both H and E_r, up to the sample annealed at 773 K. According to our previous characterization in chapter 3, after an annealing at 773 K the sample is composed of nanocrystals (FCC and M₃B) embedded in an amorphous matrix. At this point, the maximum values of the hardness and reduced Young's modulus are reached, being 24 GPa and 215 GPa, respectively. The increase of the mechanical properties between the as-quenched and the annealed amorphous samples can be attributed to the annihilation of excess free volume associated to the structural relaxation of the glass [47]. At higher annealing temperatures, the crystallization of the hard M₃B phase also contributes to the increase in the strength of the sample [44]. At annealing temperatures higher than 773 K, E_r remains almost constant while

the hardness decreases as crystallization progresses. The final state of the sample is composed by FCC crystals together with the stable boride M_2B. The decrease in hardness can be explained by the growth of the FCC phase which has low hardness compared to the amorphous state. Furthermore, with increasing the annealing temperature, the size of the FCC grains grows and hardness decreases gradually as grain growth occurs [48]. In chapter 3 we studied the evolution of the size distribution of the crystals as a function of the annealing temperature, resulting in an increase of the average size from around 70 nm at 773 K up to 185 nm at 973 K. Thus, the decrease of the hardness can be explained by the conventional Hall-Petch equation [49] that predicts an increase of the strength with decreasing grain size due to dislocation pile-up at grain boundaries. For the Si containing sample (Figure 4.3 bottom) the data shows a more complex behavior, increasing its hardness and reduced elastic modulus up to a clear maximum that occurs when annealing at 723 K, still before the crystallization onset. At higher annealing temperatures, both H and E_r decrease during the first crystallization step where a BCC solid solution together with an $M_2(B,Si)$ phase appear as explained in the previous chapter. In the second crystallization step, in which the BCC phase is replaced by FCC, E_r increases again. The decrease of both hardness and modulus at the final stages of the crystallization can be explained by the appearance of the FCC solid solution and the increase in the average grain size. Therefore, in the AB10Si10 material, the maximum value of the hardness occurs in a fully amorphous although structurally relaxed structure, in contrast with the Si-free AB20 material in which this maximum is found in a composite structure of FCC nanocrystals embedded in an amorphous matrix.

More information can be extracted from the ratio between hardness and reduced elastic modulus (H/E_r), and from the elastic recovery, i.e., the ratio between the elastic energy (U_{el}) and the total energy (elastic plus plastic, U_p) [40][41][48][49][50][51]. The H/E_r ratio is related to the elastic strain to failure and it is a suitable parameter to describe the wear resistance of the sample [22][29][52][53][54][55][56][57][58]. These values for all the analyzed compositions are shown in Table 4.1, while for all the annealing temperatures of samples AB20 and AB10Si10 are shown in Table 4.2. Among all the studied compositions, AB10Si20 shows the highest wear resistance and elastic recovery, showing that the presence of nanocrystals and larger amount of metalloid percentage helps to improve these mechanical properties. For the completely amorphous samples, AB10Si10 is the one with the better wear resistance, while all have similar values of the elastic recovery. Focusing on compositions AB20 and AB10Si10 annealed at different temperatures, the wear resistance shows a similar trend as the hardness,

being maximum at the sample annealed at 773 K in the Si-free sample, consisting of nanocrystals embedded in an amorphous matrix, while for the Si-containing sample the maximum wear resistance is found at the ribbon annealed at 723 K, still completely amorphous but structurally relaxed. However, the elastic recovery is very similar in all the cases and around the 50%, being maximum in the two compositions annealed at 773 K. Thus, the combination of nanocrystals and a relaxed amorphous matrix yields the best performance in terms of energy recovery.

AB20	H (GPa)	E_r (GPa)	U_p (nJ)	U_{el} (nJ)	U_{tot} (nJ)	H/E_r	U_{el}/U_{tot}
aq	14.5 ± 0.6	167.1 ± 4.8	0.353 ± 0.002	0.343 ± 0.002	0.696 ± 0.004	0.086 ± 0.006	0.492 ± 0.005
673 K	16.1 ± 0.1	184 ± 3	0.341 ± 0.008	0.326 ± 0.003	0.667 ± 0.011	0.087 ± 0.001	0.488 ± 0.012
723 K	19.9 ± 1.1	211.4 ± 5.5	0.276 ± 0.005	0.329 ± 0.002	0.605 ± 0.007	0.094 ± 007	0.543 ± 0.009
773 K	24.6 ± 1.6	215.7 ± 6.4	0.198 ± 0.006	0.382 ± 0.003	0.580 ± 0.009	0.114 ± 0.010	0.658 ± 0.015
823 K	22.3 ± 2.5	213.41 ± 4.1	0.247 ± 0.012	0.345 ± 0.003	0.592 ± 0.015	0.104 ± 0.013	0.582 ± 0.019
873 K	18.3 ± 2.1	209.43 ± 11.6	0.307 ± 0.005	0.316 ± 0.002	0.623 ± 0.007	0.087 ± 0.011	0.507 ± 0.008
923 K	17.5 ± 0.1	200.1 ± 17.1	0.301 ± 0.005	0.352 ± 0.003	0.653 ± 0.008	0.085 ± 0.007	0.539 ± 0.011
973 K	16.7 ± 0.1	210.36 ± 6.5	0.327 ± 0.007	0.307 ± 0.002	0.634 ± 0.009	0.079 ± 0.002	0.484 ± 0.009

AB10Si10	H (GPa)	E_r (GPa)	U_p (nJ)	U_{el} (nJ)	U_{tot} (nJ)	H/E_r	U_{el}/U_{tot}
aq	15.55 ± 0.6	162.38 ± 1.9	0.280 ± 0.10	0.435 ± 0.084	0.72 ± 0.19	0.095 ± 0.004	0.6 ± 1.3
673 K	18.3 ± 0.5	169.6 ± 7.6	0.329 ± 0.007	0.372 ± 0.003	0.70 ±0.01	0.107 ± 0.007	0.530 ± 0.011
723 K	29.94 ±0.5	211.55 ± 7.4	0.296±0.006	0.382 ± 0.004	0.678±0.01	0.141 ±0.007	0.563 ±0.014
773 K	21.4 ± 0.1	168.1 ± 3.5	0.198 ± 0.006	0.382 ± 0.003	0.580 ± 0.009	0.126 ± 0.003	0.658 ± 0.015
823 K	16.7	191.5	0.318	0.330	0.648	0.087	0.509

	± 0.9	± 4.5	± 0.004	± 0.002	± 0.006	± 0.006	± 0.007
873 K	13.7 ± 0.6	193.8 ± 5.9	0.384 ± 0.005	0.302 ± 0.003	0.686 ± 0.008	0.069 ± 0.005	0.440 ± 0.009
923 K	13.5 ± 0.7	188.1 ± 4.7	0.394 ± 0.008	0.302 ± 0.006	0.696 ± 0.014	0.071 ± 0.005	0.433 ± 0.017
973 K	10.4 ± 0.3	167.6 ± 3.1	0.472 ± 0.002	0.307 ± 0.005	0.779 ± 0.007	0.062 ± 0.002	0.394 ± 0.009

Table 4.2 Hardness (H), reduced Young's modulus (E_r), plastic energy (U_p), elastic energy (U_{el}), wear resistance (H/E_r) and elastic recovery (U_{el}/U_{tot}) measured by nanoindentation for AB20 and AB10Si10 samples for different annealing temperatures.

The analysis of the SEM images of the indents can yield information on some phenomena such as sink-in and pile-up [59]. Pile-up effect happens when the surface is indented heavily and the localized plastic deformation zone pushes the surrounding material upward around the indent. On the other hand, sink-in happens when the plastic zone tends to shift away from the indent area. In crystalline materials, the formation of pile-up along a specific directional line around the indent can be related to the crystallographic orientation of the crystal and to the crystal symmetry [60]. The method of Oliver and Pharr to compute the hardness does not consider the effect of pile-up and it can induce an overestimation of the calculated hardness [61] and also influences the elastic modulus determination by changing the contact area. In Figure 4.4 the SEM image of a typical indentation of annealed sample AB20 at 873K is shown (a), together with the projected (b) and the pile-up area (c) calculated using the ImageJ software.
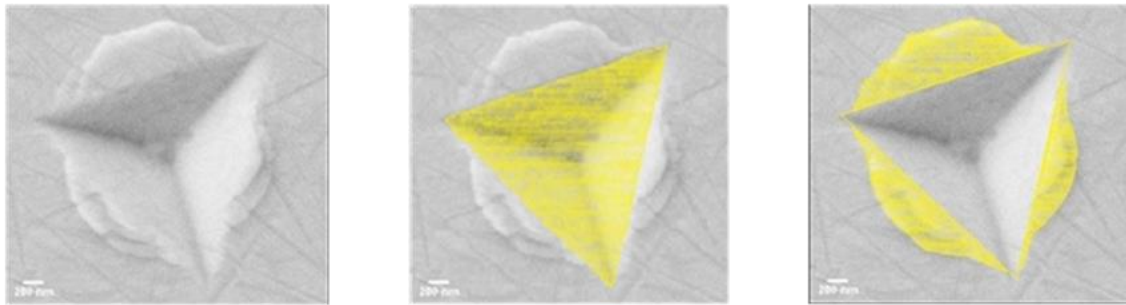
Figure 4.4 SEM image of an indentation (left), definition of the area to compute the projected area (middle) and the pile-up area (right).

Figure 4.5 shows the fluctuation of the pile-up area as a function of the annealing temperature of samples AB20 and AB10Si10. It can be seen that in both samples there is no formation of pile-up until annealing at 723 K. At this temperature, the structure is mainly amorphous although the AB20 sample contains some fraction of nanocrystals. It is important to note that in this case the error bar in the pile-up area is relatively large and is compatible

with a value close to zero. When amorphous metals deform plastically the deformation causes an increase of the internal free volume. At higher annealing temperatures the behavior of the two compositions is different. For the AB20 sample, the pile-up remains close to zero up to the end of the first crystallization (at 823 K) when it reaches its maximum value. At this temperature, the structure consists of an FCC solid solution together with the M_3B phase. As the crystallization progress and this boride is replaced by the M_2B one, the pile-up area steadily decreases. On the contrary, for the AB10Si10 sample, after an increase of the pile-up as the amorphous structure relaxes before crystallization, the pile-up area is reduced to zero during the first crystallization event in which the structure consists mainly of a BCC solid solution together with the $M_2(B,Si)$ phase. As the BCC is replaced by the FCC one, the pile-up area continuously grows until reaching its maximum value in the fully crystallized sample. The effect of the pile-up is higher on the hardness than on the elastic modulus because the hardness is inversely dependent on the area while the elastic modulus depends on the square root of the area. The pile-up effect increases when the strain hardening exponent decreases [62]. Therefore, the fully crystallized samples of the Si-containing composition behave more plastically than the Si-free composition. However, for the samples annealed only to the first crystallization, where the Si-free sample contain the M_3B phase, the behavior is reversed, being more plastic this composition than the Si-containing one. Some overestimation of H could happen due to the formation of the pile-up. In a latter article [63], Oliver and Pharr reviewed the limitations of their original model and noticed that a convenient parameter that illustrates the possible influence of pile-up formation on the mechanical properties is the ratio h_f/h_{max}, which is independent of the indentation depth in self-similar geometries, such as the Berkovich indenter. For conical or Berkovich indenters, when this ratio is smaller than 0.7 like in the present case, the little pile-up observed (regardless of the work hardening behaviour of the tested material) does not have a strong influence on the obtained results. Conversely, their original method becomes more inaccurate for $h_f/h_{max} > 0.7$.
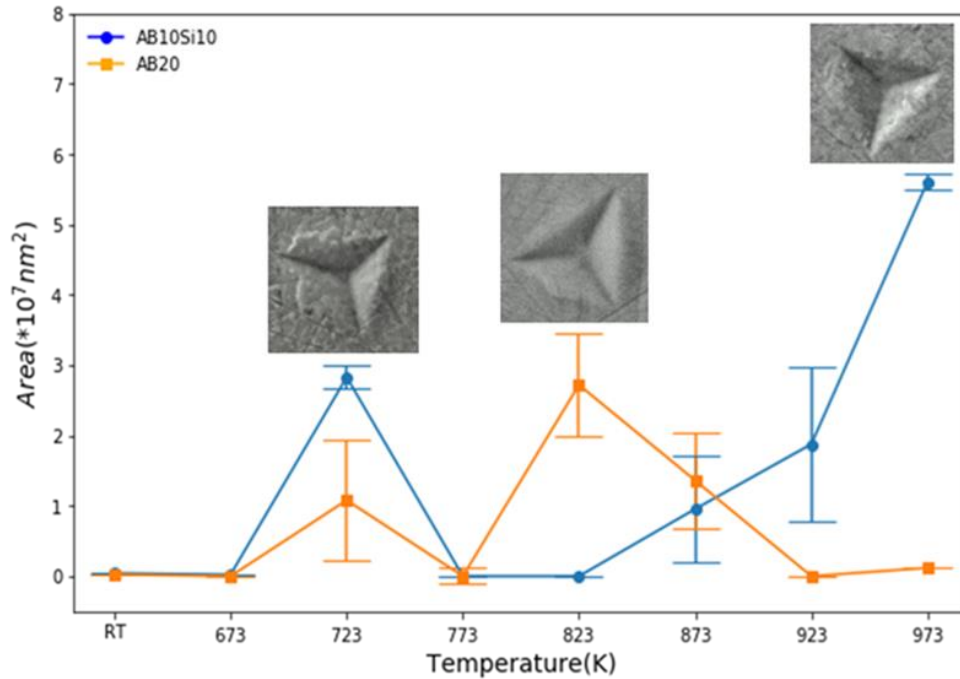
Figure 4.5. Measured pile up area for different annealing temperatures (K).

4.2. Discussion

In chapter 4 we have studied the mechanical properties of a new family of high entropy metallic glasses (AB20, AB10Si10, AB10Si20, AB10Si15 and AB15Si5) by nanoindentation. The main results obtained can be summarized as follows:

1) There is a large increase in hardness in the new amorphous materials, as compared to the base HEA, due to the strong nature of the (B,Si)-M interatomic bonds and the absence of order and crystalline structure. However, the amorphous samples with nanocrystalline inclusions, induced by annealing treatments, show further enhancement of the mechanical properties.

2) The evaluation of the mechanical properties as a function of the annealing temperature reveals that the higher values of hardness are found in a structure composed of nanocrystals embedded in an amorphous matrix in the case of the Si-free alloys and in a fully amorphous structure, although relaxed by annealing, in the Si-containing alloys.

3) The wear resistance and elastic recovery are higher in the partially crystalline samples. These results point towards a particular strategy to design new high-entropy metallic glasses with improved mechanical properties within the $(FeCoCrNi)_{100-x-y}B_xSi_y$ system, i.e, the development of a mixed structure consisting of nanocrystals embedded in an amorphous,

relaxed matrix. As demonstrated in this work, this can be achieved by firstly obtaining an amorphous structure by rapid solidification and posteriorly tuning the microstructure by designing the appropriate annealing treatments.

CHAPTER5.ELECTROCHEMICAL CHARACTERIZATION

Corrosion-related accidents cause major economic loses and are a huge concern for the safety of personnel and property. The direct annual cost of corrosion across the globe was reported to be approximately 3 percent of global gross domestic product (GDP) [64]. In the United States, around US$ 2-4 trilions is lost due to corrosion-related failures each decade. Therefore, it is necessary to study corrosion and its different forms to design and choose suitable materials for specific applications and improve safety standards. Corrosion is the chemical reaction of a material within the environment which causes its degradation. This reaction can be sorted in numerous ways including the nature of the corroding agent of which there are two categories, wet and dry. Wet corrosion refers to the corrosion of a material in aqueous environment with an electrolyte and dry corrosion refers to the corrosion of a material in a gaseous environment. Another way to classify corrosion is the appearance of the corroded metal (uniform or localized). Uniform corrosion take places when the corrosion reaction happens over all the surface of the material while localized corrosion occurs at specific locations [65]. Other mechanisms of corrosion can be categorized under the names of electrochemical and direct chemical. Direct chemical corrosion is an attack resulting from direct exposure of a bare surface to a caustic liquid or gaseous agent occurring simultaneously at the same point while in an electrochemical attack the anodic and cathodic changes may take place a measurable distance apart. Electrochemical is the most common corrosion process and it happens when two or more electrochemical reaction occur, including at the minimum one oxidation and one reduction reactions. In overall there are two main requirements for the reaction: a) there must be an anode and a cathode to provide an area for oxidation and reduction and b) there must be a pathway for electrons to flow from the anode to the cathode. If any of these conditions are removed, the corrosion process stops. The anodic and cathodic sites can be created on the surface of a metal due to heterogeneities (like composition and grain size differences, surface roughness, impurities or inclusions, localized stresses or dislocation arrays) or between two dissimilar metals exposed to the corrosive environment. Metals can have three different responses to an electrochemical reaction according to the environment: it can show immune, active or passive reaction. Immune reaction happens when materials are thermodynamically stable in an environment and, therefore, they will not corrode. Active

metals go through the corrosion reaction with the environment and form corrosion products. In a passive reaction, corrosion at first happens but the resulting product is insoluble and acts as a protective film. This coating layer dramatically reduces the rate of corrosion but if it is broken, the metal turns over to an active reaction.

Corrosion can be avoided by the following methods: alloy additions, coatings and inhibitors or design modification. It was discovered that the strongest influence on the corrosion behavior is caused by the chemical composition and microstructure in the alloys. Proper material selection is one of the most effective strategies to reduce the corrosion rate. Metallic glasses, hold tremendous potential as corrosion-resistance alloys (CRAs) and a series of metallic glasses based on copper, palladium, zirconium, titanium, magnesium and iron have been successfully produced [66]. In the case of a positive influence of alloying on the corrosion properties of alloys, B and Si have been shown as good alloying elements [67],[68]. Therefore, the aim of this chapter is to assess the effects of B and Si against corrosion resistance of some selected HEAMG's compositions produced in this thesis, in particular $(FeCoCrNi)_{80}B_{20}$ and $(FeCoCrNi)_{80}B_{10}Si_{10}$, which were produced by rapid-solidification technique and were labelled in chapter 3 as AB20 and AB10Si10 samples, respectively. The corrosion resistance of these two samples will be compared with the one of the HEA $(FeCoCrNi)_{100}$, labelled A. It is well known that all sources of localized corrosion disappear in the absence of common structural defects such as grain boundaries, dislocations and segregations [68][69],[70],[71],[72]. Moreover, previous research showed the effect of structure, chemical composition and material homogeneity on the electrochemical behavior of amorphous alloys [73]. Considering the remarkable corrosion resistance of Fe, Ni, and Co- based amorphous alloys, it is important to study the effect of metalloid elements (B, Si) as well as other alloying elements (Cr, Mo, ..) that could improve the glass forming ability or the corrosion resistance. The main studies on the subject have shown that the corrosion resistance of Fe, Cu, Ni and Co-based amorphous alloys in sulphate and chloride media is largely affected by alloying with various additional elements such as Cr, Mo, Ni [72],[73].

5.1. Electrochemical measurements in NaCl solution

The potentiodynamic polarization curves for the A, AB20, and AB10Si10 samples in 3% NaCl solution are shown in Figure5.1. The corrosion potential (E_{corr}) and corrosion current density (I_{corr}) were determined by extrapolating the Tafel curves and are summarized in Table5

66

1. The values of E_{corr} and I_{corr} of the as-quenched ribbons change with the amount of B and Si. Here, AB20 has the highest E_{corr} and lowest I_{corr}. With the reduction in B and increase in Si, the E_{corr} decreases while I_{corr} is kept constant. The crystalline ribbon without B and Si, which we take as the reference material, has the lowest E_{corr}. It is well known that corrosion is more likely to occur at grain boundaries, defects, and regions where there is large segregation of elements, thus the amorphous nature of the AB20 and AB10Si10 samples promotes chemical and microstructural homogeneity and improves the corrosion resistance [74]. Moreover, the action of B as a corrosion inhibitor is also reported by several authors [75],[76]. Accordingly, the E_{corr} value of the AB10Si10 is slightly lower than the one of the AB20 alloy, with the same corrosion current density. These electrochemical parameters can be compared with the ones corresponding to other high-entropy alloys. If we compare them with crystalline HEA, the results shown here present a more noble E_{corr} and lower I_{corr} [77],[78],[79],[80] and they also show an improvement with respect to other similar high-entropy bulk metallic glasses that show E_{corr} values between −23 and 77 mV [81].
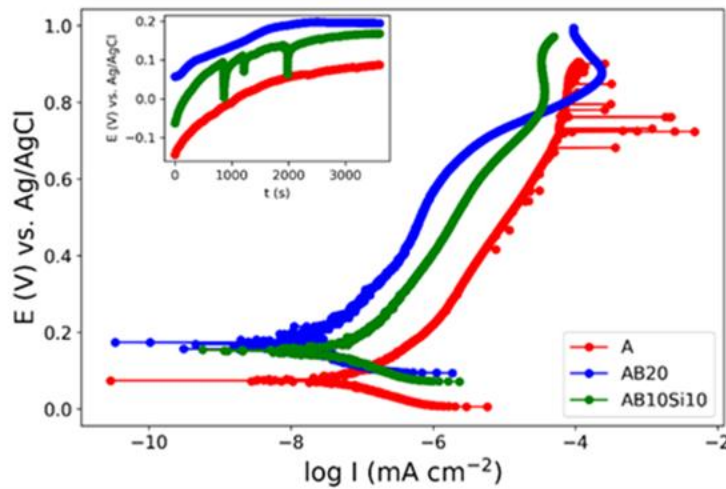
Figure5.1 Potentiodynamic polarization curves of as quenched A, AB20 and AB10Si10 ribbons in 3 wt% NaCl. The inset show the evolution with time of the OCP.

Alloy	E_{corr} (mV)	I_{corr} (nA cm^{-2})
A	70	0.09
AB20	170	0.06
AB10Si10	150	0.06

Table 5.1 Summary of the quantitative analysis of the potentiodynamic polarization test of the A, AB20 and AB10Si10 samples. The estimated error for the corrosion potential is ±10 mV while for the corrosion current is ±0.01 nA cm^{-2}.

67

At this point, a question arise about which factor plays a more important role in corrosion resistance. As commented on previously, some studies explain the improvement in the corrosion resistance because of the high-entropy effect that reduces the mobility of the atoms [82]. We can compute the entropies of these alloys and distinguish between the configurational entropy and the mismatch entropy [83]; the configurational entropy is simply proportional to the ln(N), where N is the number of components, thus we have an increase in this entropy from the A alloy (N = 4) to the AB10Si10 alloy (N = 6). The mismatch entropy has been shown to be proportional to the delta parameter that is a measure of the atomic size difference between the constituent atoms, and this value increase from 0.3% for the A alloy to 14.70% for the AB20 and 10.72% for AB10Si10 [84]. Therefore, from these values and the electrochemical parameters, it would seem that the mismatch entropy is the main factor affecting the corrosion resistance, but this analysis does not consider the fact that AB20 and AB10Si10 are amorphous samples with a disordered structure. Thus, in order to clarify this point, a systematic analysis of several families of HEAs and HEMGs should be performed but this is out of the scope of this paper.

5.2. Electrochemical Impedance Spectroscopy (EIS) measurements

Figure 5.2a,b shows the Nyquist and Bode plots, respectively, of the EIS measurements on the three samples. The absolute value of the impedance (|z|) at very low frequencies ($\omega \rightarrow 0$) represents the polarization resistance (R_p) which is the transition resistance between the electrodes and the electrolyte while the value at very high frequencies ($\omega \rightarrow \infty$) represents the solution resistance, (R_s) [85]. As can be seen in Figure 5.2a, the three samples show similar behavior. The phase angle shown in Figure 5.2b and defined as:

$$\phi = \tan^{-1}\left(\frac{Im(Z)}{Re(Z)}\right) \tag{5.1}$$

presents some differences. The broadened base of the phase angle and its magnitude are a signal of the pseudo-capacitive behavior, which can be modelled by using a constant phase element [85,86]. Here the single local minimum indicates the presence of a capacitance element that can be modelled by a single capacitor or two capacitors of similar magnitude. For all of these three alloys, these capacitors can be passive films or an electrical double layer capacitance. In order to quantitatively assess the differences between the alloys, the Nyquist and Bode plots have been fitted to an equivalent circuit consisting of one resistor in series with a parallel

68

combination of a constant phase element and a Warburg element and also in series with a parallel combination of a resistor and a capacitor as illustrated in Figure 5.3b. The fitting was performed with EC-Lab v11.10 software and the obtained parameters from the fitting are provided in Table 5.2. The left part of the circuit, which contains the resistor R2 and the capacitor C2, is related to the movement of mobile charges trough the solid and liquid phases and the non-faradic charge accumulation at the solid/liquid interface of the electrode.

| | (a) | (b) |
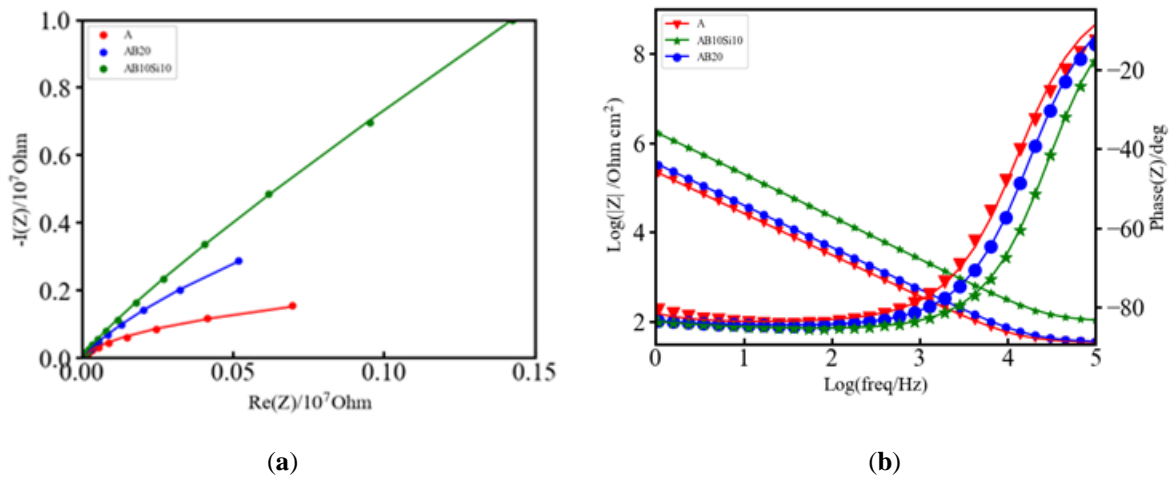
Figure 5.2 (a) Nyquist plot of A, AB20 and AB10Si10 impedance fitted by the inset equivalent circuit model. Raw data are dots and the fitting result is represented by lines of the same color and **(b)** Bode plot of A, AB20 and AB10Si10

This charge accumulation in the interface constitutes what is commonly known as the capacitive double layer (shown in Figure 5.3) where three different regions can be distinguished: a first layer that mainly contains polar water molecules and adsorbed anions, called the inner Helmholtz plane (IHP), a second layer with fully hydrated cations, called the outer Helmholtz plane (OHP) and a final diffuse layer composed of hydrated anions and cations [87]. From the values of Table 5.2, it is evident that the amorphous alloys present higher corrosion resistance as the value of the capacitance is the lowest with respect to the crystalline one. Therefore, it can be stated that in the amorphous alloys, the formation of the double layer capacitance increases the corrosion resistance. However, the overall electrochemical behavior also depends on the inhomogeneities of the electrode surfaces.
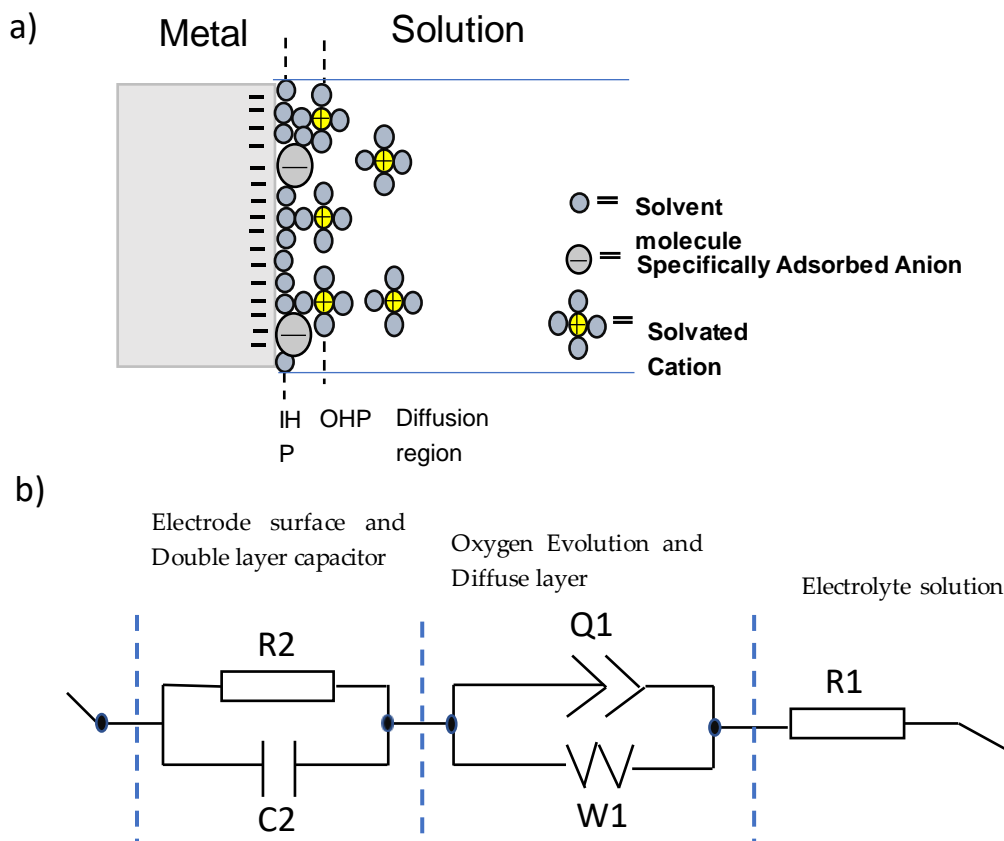
Figure 5.3 (a) Schematic representation of a metal electrode surface in the solution and (b) the equivalent electrical circuit used to fit the impedance data. R1 and R2 are the electrolyte and charge transfer resistance, respectively. Q1 is the constant phase element, W1 is a Warburg element and C2 is a capacitor.

Electrode surface irregularities play a significant role in the electrochemical response. There are several factors which cause these irregularities, such as surface roughness and chemical heterogeneities (that include differences in the constituent elements, chemical impurities, and surface band impurities and coatings). Moreover, solid electrodes are not smooth; they exhibit complex surface morphologies with a varying degree of irregular interfaces (i.e., rough, porous, and partially active interfaces). All these effects are modelled by the middle part of the equivalent circuit, which contains a constant phase element (Q_1) that corresponds to inhomogeneities in the surface on the atomic and nanoscopic scale (roughness) and crystallographic disorder (due to anisotropic surface atomic structure) of the metal oxide electrode, and a Warburg diffusion element (W) that corresponds to the diffusion of mobile charges within the metal oxide electrode in the solution, respectively. The higher values of Q1 for the A alloy reflect the higher inhomogeneity of this alloy and its lower resistance to corrosion. Finally, the right part of the circuit, R1, is related to the resistance of the electrolyte

solution that in this case is higher for the AB10Si10 alloy reflecting better electrochemical behavior.

Alloy	$R_1(\Omega)$	$R_2(k\Omega)$	C_2 (F)	$Q_1(Fs^{(a-1)})$	a	$W_1(\Omega s^{-1/2})$
A	33.45	1149	1.697×10^{-6}	1.335×10^{-6}	0.906	3.219×10^6
AB20	34.41	21310	0.854×10^{-6}	0.991×10^{-6}	0.913	1.844×10^6
AB10Si10	100.4	258800	0.156×10^{-6}	0.200×10^{-6}	0.927	5.543×10^6

Table 5.2 Parameters from the fitting of the Nyquist plot to an equivalent electrical circuit.

5.3. XPS analysis of A, AB20 and AB10Si10 alloys immersed in NaCl

The corrosion resistance of HEMGs in a particular corrosion environment will be determined by how their surface reacts to the corrosion agent and by the composition of the passive film that can be formed on the surface. Therefore, X-ray photoelectron spectroscopy (XPS) is used in this work to evaluate the surface to obtain information about the effect of anode polarization on the surface composition and determine the oxidation state of the different elements [88]. The use of small amounts of Al, Cr, or Si has been shown to improve oxidation resistance in conventional alloys due to the formation of a stable oxide layer on the surface [89]. On the contrary, Fe-based HEAs do not present these restrictions on the amount of other elements and, thus, Al, Cr, or Si may be present in higher concentrations in order to facilitate the formation of the oxide films [90]. The XPS spectra of our samples are shown in Figures 5.4a,5.5a, and5.6a, for the A, AB20, and AB10Si10 samples, respectively. The figures show the survey spectrum (low-resolution measurements in a large energy range) in panel (a) and the high-resolution emission peaks associated with the Fe 2p, Cr 2p, and O 1s core electron levels in panels (b), (c), and (d), respectively. Moreover, Figures5.5 and5.6 also include in panel (e) the B 1s core electron level and the Si 2p core electron level emission peak, respectively. The different dashed lines mark the theoretical energy of different oxidation states of the corresponding element and are used as a reference. The C 1s line is due to the carbon present in the sample holder and is used for the energy calibration. The presence of O in the long-range energy spectra of the three alloys is observed before and after polarization measurements, suggesting that an oxide film is spontaneously formed on the sample surface

before immersion in the NaCl solution. Figure5.4a shows the normalized XPS spectrum of sample A after immersion in a 3 wt.% solution of NaCl, indicating the presence of Fe, Cr, Co, Ni, and O, although the peaks associated to Co and Ni are barely visible. High-resolution spectra at the energy of the Fe 2p peak reveals that Fe is present on the surface as Fe^{3+} with a binding energy of 710.15 eV (Figure5.5b). On the other hand, the Cr 2p peaks are at 573.29 and 575.91 corresponding to metallic Cr and Cr^{3+}, respectively (Figure5.5c). The presence of Cr^{3+} is considered to be crucial to the quality of the passivation film for the A composition. In addition, the binding energy peaks of O 1s represents a M-O compound characteristic peak corresponding to O^{-2} species (529.54 eV) and a M-(O-H)$_n$ compound characteristic peak corresponding to O-H species (532.06 eV) (Figure5.4d).
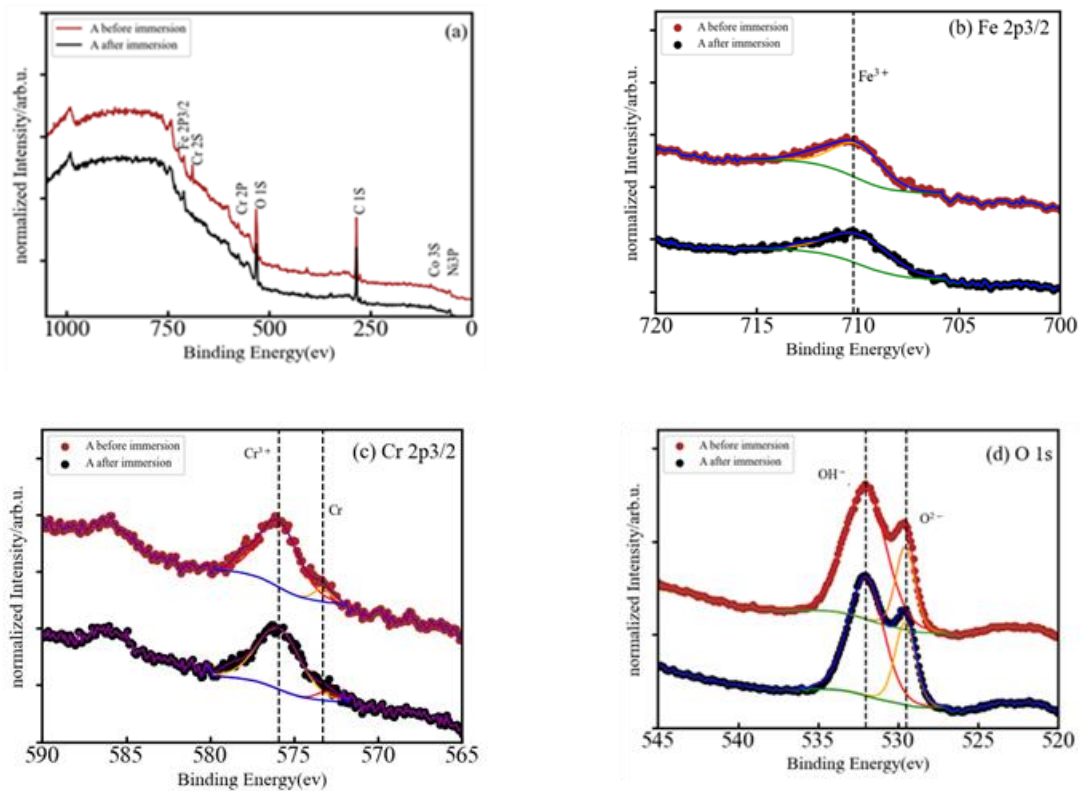
Figure 5.4 (a) Normalised XPS spectrum of A after immersion in 3 wt.% NaCl ((b)-(d)) High-resolution XPS spectra of Fe 2p3/2, Cr 2p3/2 and O 1s.

Figure 5.5(a) presents the normalized XPS spectrum of AB20 high entropy metallic glass alloy before and after immersion in a 3 wt.% NaCl solution. The peaks of Fe 2p, Cr 2p, O 1s and B 1s can be easily seen and the Co 3s and Ni 3p are barely visible. The Fe 2p (Figure 5.5(b)) presents 2 peaks centered at 706.81 and 710.09 eV which correspond to metallic Fe and Fe^{3+}, respectively. In the Cr 2p XPS spectrum (Figure 5.5(c)), the binding energy peaks are centered at 573.53, 575.94, 576.88 eV and can be ascribed to metallic Cr, Cr^{3+} and Cr^{6+}.

72

Deconvolution of the O 1s peak (Figure 5.5(d)) results again in two component peaks with energies of 529.90 eV that represents a M-O compound characteristic peak corresponding to O^{-2} species and a second peak (531.87 eV) that represent a M-$(O-H)_n$ compound characteristic peak corresponding to O-H. B 1s spectra (Figure 5.5(e)) was also deconvoluted in two peaks which were assigned to a boride (189.82 eV) and B^{3+} (191.73 eV) bonds respectively.

Figure 5.5 (a) Normalised XPS spectrum of AB20 after immersion in 3 wt.% NaCl ((b)-(e)) High-resolution XPS spectra of Fe 2p3/2, Cr 2p3/2, O 1s and B 1s.

In Figure 5.6a, the full XPS spectra for sample AB10Si10 clearly shows the coexistence of elemental Fe, Cr, O, and Si, but Co, Ni, and B are indistinguishable from the baseline. The high-resolution XPS spectra of Fe 2p, Cr 2, O 1s, and Si 2p are shown in Figure 5.6b–e. In the

Fe 2p XPS spectrum, the binding energy peaks at 706.42 and 710.02 eV are attributed to metallic Fe and Fe^{3+}, respectively. There are three peaks of Cr 2p after immersion in solution (Figure 5.6c) at 573.23 eV that corresponds to metallic Cr, at 576.25 eV for Cr^{3+}, and at 577.99 eV for Cr^{6+}. Moreover, the high-resolution XPS spectrum of O 1s (Figure 5.6d) comprises a peak at 529.52 eV for M-O and 531.61 eV for M-(O-H)$_n$. The Si 2p spectrum (Figure 5.6e) shows two peaks centered at 98.96 eV and 101.66 eV that correspond to metallic Si and Si^{4+}, respectively.
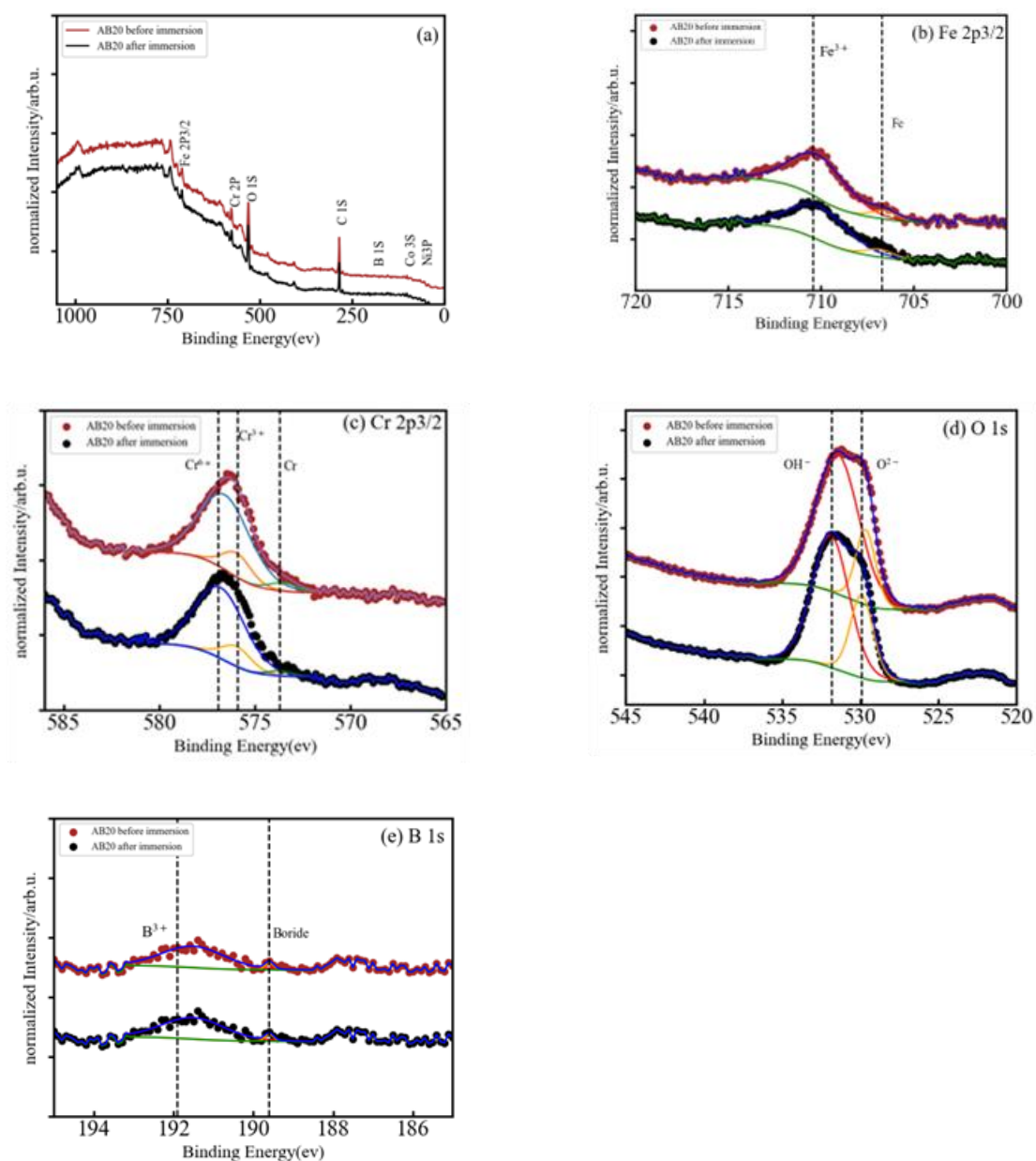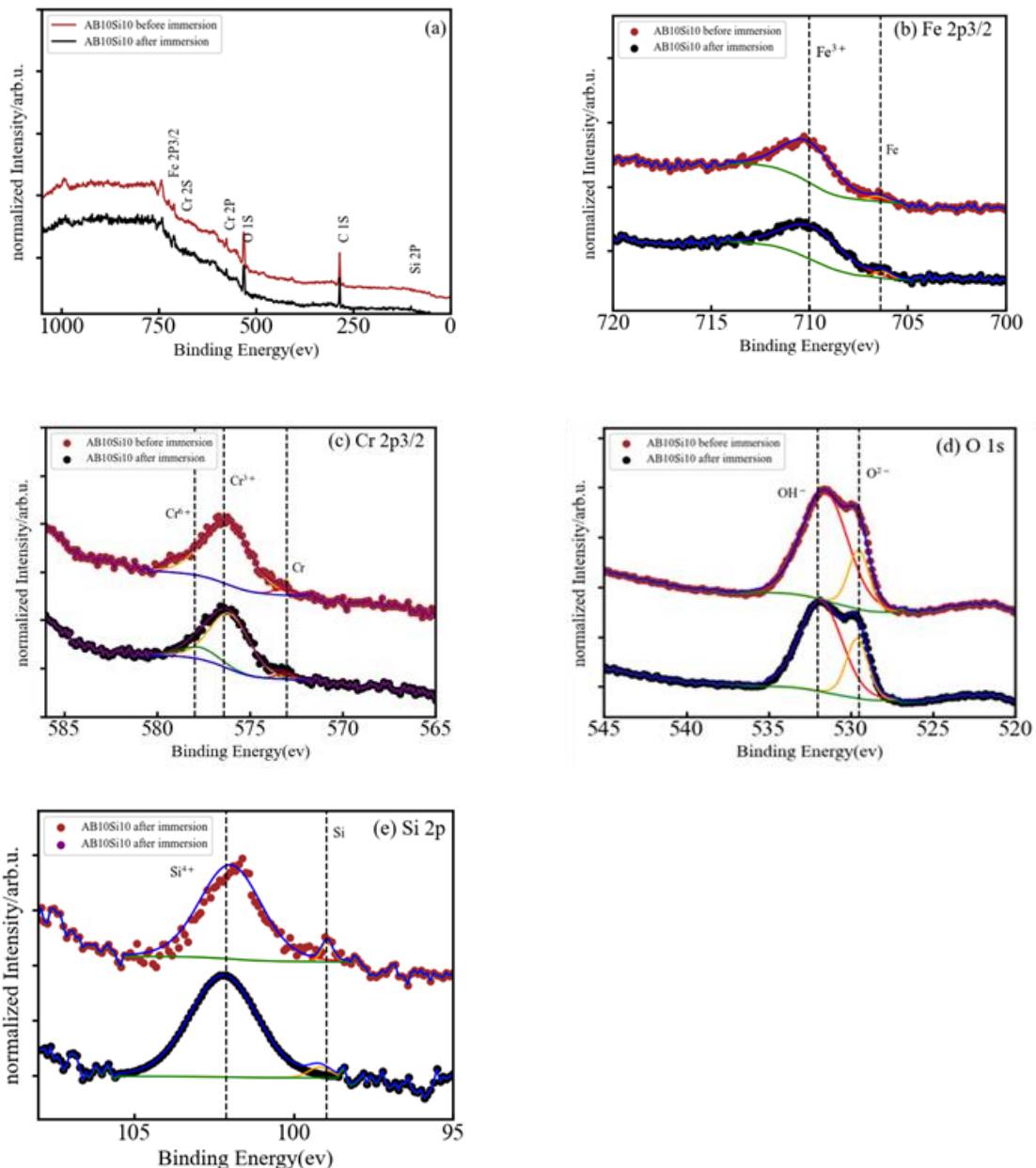

Figure 5.6. (a) Normalised XPS spectrum of ABSi after immersion in 3 wt.% NaCl ((b)-(e))High-resolution XPS spectra of Fe 2p3/2, Cr 2p3/2, O 1s and Si 2p.

In summary, in each of the samples, almost all the elements were detected on the surface, both in form of oxides and unoxidized metal (M^0) species. As the XPS signal can gather information from 5–10 nm in depth [91], the significant absence of Co and Ni in the survey spectra means that these two elements do not play any role in the formation of the oxide layer before immersion. The metal oxides Fe^{3+} and $Cr^{3+}$ were detected on the surface of all samples, and it is well known that these oxides can produce a certain level of protection in corrosive environments [92,93]. These two oxides are the dominant oxide forms on the surface of the A, AB20, and AB10Si10. Nascimento et al. [83] explained the high corrosion resistance of the FeCoCrNi alloy by the high concentration of Cr_2O_3 in the passive film. The addition of B to the A alloy results in the formation of B-O bonds on the surface of the AB20 sample, while the decrease in B and the addition of Si yields the presence of silicates and a small fraction of metallic Si on the surface of the AB10Si10 alloy. Moreover, and without needing to perform a quantitative analysis, it is clear that for each sample, the oxidized form of each constituent element has a higher percentage than the corresponding unoxidized metal (M^0) species. According to Qiu et al. [92], it is expected that the coexistence in the complex surface film of both metallic oxides and unoxidized metal species can increase the passivity of the samples and, thus, increase the corrosion resistance. Moreover, some research shows that boron addition not only improves the GFA of Fe-Cr-B-based alloys but also promotes superior corrosion resistance [94], which is in accordance with the results presented here. On the other hand, replacing the B with Si in AB20, which has the highest E_{corr}, favors the creation of silicates on the surface of AB10Si10, which according to Masumoto et al. [95] decreases the corrosion resistance of the alloy, as has been observed in the above LPR results of these alloys in a 3 wt.% NaCl solution.

5.4. Microstructure characterization after immersion in NaCl

To gain a better understanding of the evolution of the corrosion product layer after the immersion tests, SEM images were taken to analyze the surface morphology of the alloys. After the polarization experiments, the specimens were cleaned with distilled water and dried in nitrogen immediately. The morphology of samples A, AB20, and AB10Si10 before and after immersion in a 3 wt.% NaCl solution and the linear polarization measurements are shown in Figure 5.7. Before immersion, the amorphous samples are completely homogenous. In Figure 7b, which corresponds to the A alloy after immersion, we can see some localized corrosion in

different points (small black points) which have been damaged by the chloride ion attack, presumably in an area with a low Cr content [96]. Moreover, it should be mentioned that within the sensitivity of the method no inhomogeneities in the element distribution were seen in the FeCoCrNi alloy. Therefore, the passive films that are formed are relatively weakly bonded and inadequate to restrict the propagation of the corrosion process in this system [97,98]. As can be seen from Figure 5.7d,f, no pitting corrosion exists on the surface of the amorphous samples, which is mainly due to the homogeneous formation of the passive film produced on the surface by the borides and the possible mixture of oxides and hydroxides phases, as seen by XPS. Moreover, the formation of this homogenous passive film is favored by the homogenous amorphous structure. In order to better understand this passive film, a TEM study should be performed.
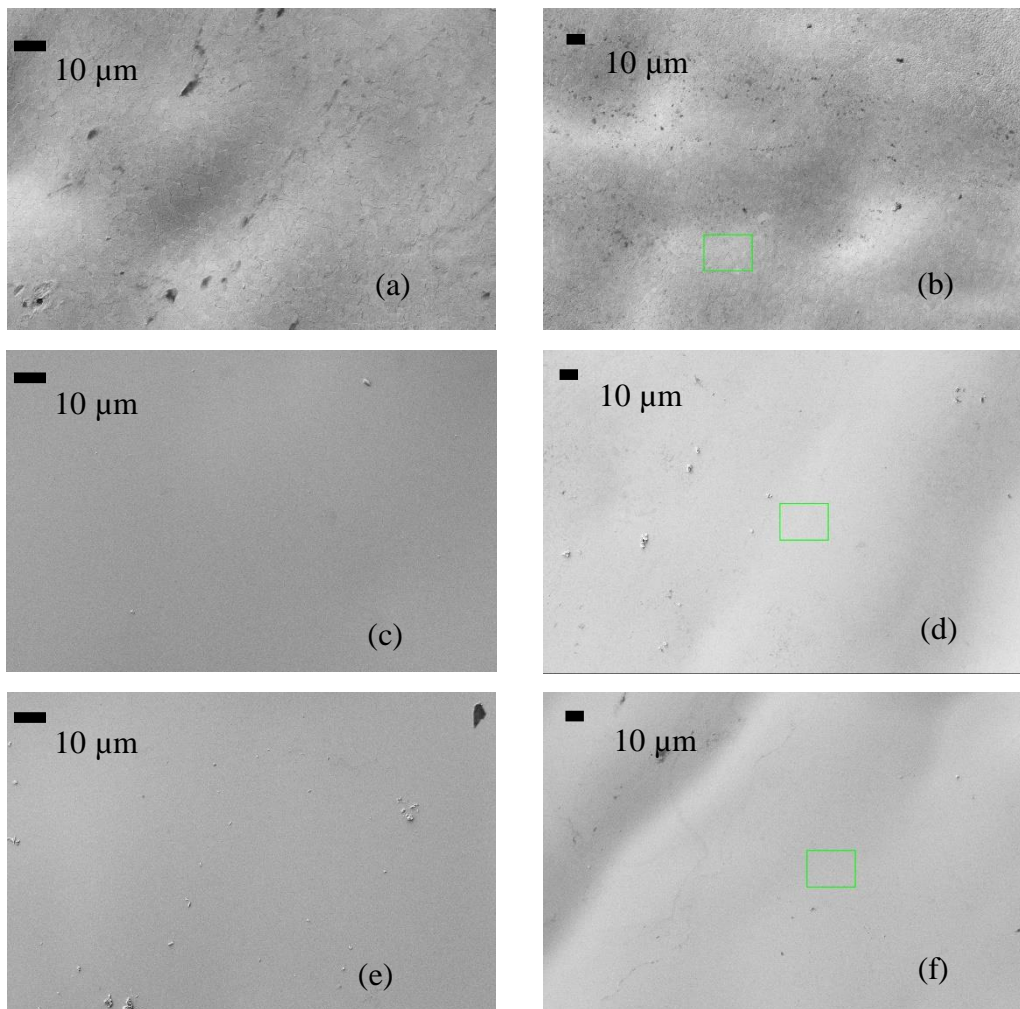
Figure 5.7. (a) (c) (e) BSE images of the surface of samples A, AB20 and AB10Si10, respectively before immersion in 3wt.% NaCl at room temperature. (b) (d) (f) BSE images of the A, AB20 and AB10Si10, respectively, after immersion.

76

CHAPTER6. CONCLUSIONS

The present study about the preparation and properties of a series of new high-entropy alloys $(FeCoCrNi)_{100-x-y}B_xSi_y$ with different percentage of B and Si content leaded us to the following conclusions:

Alloys of nominal composition $(FeCoCrNi)_{100-x-y}B_xSi_y$ with (x=0, 5, 10, 15, 20 and y =0, 5, 10, 15, 20 in atomic percentages) were quenched by melt-spinning at a cooling rate of about 10^6 k s^{-1}. In the first four alloys, $(FeCoCrNi)_{80}B_{20}$, $(FeCoCrNi)_{75}B_{10}Si_{15}$, $(FeCoCrNi)_{80}B_{10}Si_{10}$, $(FeCoCrNi)_{80}B_{15}Si_5$, the partial substitution of B with Si is effective for the formation of an amorphous structure whereas a further increase in the atomic percentage of Si produces crystalline, or partially crystalline in the case of $(FeCoCrNi)_{70}B_{15}Si_{15}$, samples.

According to the ΔH_{mix} versus δ map, the general criteria to distinguish between HEAs and HEMGs are only approximately valid in this family of compositions due to the presence of large contents of metalloid atoms.

The reduced glass transition temperatures, T_{rg} , obtained by Differential Scanning Calorimetry (DSC), which fluctuate between 0.5 and 0.6, indicate that these compositions are unlikely to be produced as bulk metallic glasses. An addition of 10 at% of B and 15 at% of Si to the base equiatomic composition (FeCoCrNi) maximize the glass forming ability and thermal stability of the amorphous phase.

The study of the crystallization of the samples with composition $(FeCoCrNi)_{80}B_{20}$ and $(FeCoCrNi)_{80}B_{10}Si_{10}$ shows that for the first sample the FCC and M$_3$B phases appeared as the first crystallization product at 823 K but M$_3$B was not a stable phase and it disappeared before the second crystallization. After the second crystallization, the FCC phase still grows beside the formation of M$_2$B and this M could correspond to different metals (Fe, Co or Ni). For the second composition, it remained completely amorphous below 773 K and by increasing the temperature the nucleation and growth of a BCC and M$_2$(B,Si) phases slowly started. After the temperature reached 823 K the formation of an FCC and a new boride phase started. Finally, at the end of the process, we have a BCC phase together with an FCC and M$_2$(B,Si) phases.

The results of the size distribution of the crystalline grains from SEM photos show the effect of heat treatment on the average size of the nanocrystalline particles, as it increased from ~ 69 nm at 823 K to ~185 nm at 973 K for $(FeCoCrNi)_{80}B_{20}$ and from ~ 37 nm at 823 K to ~135 nm

at 973K for $(FeCoCrNi)_{80}B_{10}Si_{10}$. These results also show that the replacement of some part of B with Si leads to the reduction of the size of the microstructure.

The results from Mössbauer spectroscopy allow to complement the X-ray diffraction data, confirming that the sample $(FeCoCrNi)_{80}B_{20}$ decomposes into FCC and M_3B phases and that after 873 K some part of the FFC phase and M_3B phase decomposes into M_2B, producing that at the end of the crystallization path there is the same amount of paramagnetic and ferromagnetic phase. In the other sample, $(FeCoCrNi)_{80}B_{10}Si_{10}$, the amorphous phase at the room temperature decomposes in to a BCC phase and $M_2(B,Si)$. With the increase in temperature some part of the BCC phase decomposes to an FCC phase while the fraction of $M_2(B,Si)$ crystals remain constant or even increased. Finally, after 873 K the BCC phase completely vanished and a mixture of FCC and $M_2(B,Si)$ remained. The fully crystalline sample contains more ferromagnetic (~64 at%) than paramagnetic phases (~36 at%). Therefore, the substitution of B by Si, besides changing the crystallization products, also favors the presence of ferromagnetic components.

According to the result regarding the mechanical characterization of the samples there is a large increase in hardness in the amorphous samples with respect to the base HEA alloy because of the strong nature of (B,Si)-M interatomic bonds and the absence of long-range order and crystalline defects. All the amorphous samples exhibit excellent high hardness whereas those amorphous samples with embedded nanocrystalline particles show better mechanical properties.

This study shows that the use of an adequate amount of B and or/Si drastically improve the hardness (close to double) and the value of the reduced elastic modulus. Moreover, the amorphous character of the samples has shown a much higher hardness than other crystalline alloys with a diversity of microstructures and with similar base compositions (Fe, Co, Cr) but different alloying elements (Cu, Si, Al).

A microstructure consisting of a mixture of an amorphous phase with embedded nanocrystals shows higher hardness values in Si–free samples while in the case of Si-containing samples, the completely amorphous phase is the one with higher hardness.

The results of wear resistance and elastic recovery are higher in the samples that are partially crystalline. All these results will enable us to create special strategies to design high-entropy metallic glasses in the $(FeCoCrNi)_{100-x-y}B_xSi_y$ system with enhanced mechanical properties.

The electrochemical properties and the effect of partial substitution of B by Si in the $(FeCoCrNi)_{80}B_{10}Si_{10}$, $(FeCoCrNi)_{80}B_{20}$ and FeCoCrNi alloys were measured by linear polarization resistance and electrochemical impedance spectroscopy techniques. The results show that amorphous samples without Si and an adequate amount of B exhibit a higher corrosion resistance due to the fact that B promotes the stability of the passivation films. The higher corrosion resistance of $(FeCoCrNi)_{80}B_{20}$ may be attributed to the absence of crystallographic defects, uniformity of passive film, as well as the intrinsic higher activity of the amorphous surface. With the reduction of B and the increase of Si, the E_{corr} slightly decreases while I_{corr} keeps constant. The crystalline ribbon without B and Si, that we take as a reference, has a lower E_{corr} than the amorphous ribbons and this can be a consequence of the formation of an FCC phase in the structure. From the XPS results it can be concluded that the formation of different combinations of oxides and hydroxides protect the samples from corrosion events on different points of the surface.

References

1.   Klement, W.; Willens, R.H.; Duwez, P.O.L. Non-Crystalline Structure in Solidified Gold-Silicon Alloys. *Nature* **1960**, *187*, 869–870.

2.   Miller, M.; Liaw, P. *Bulk Metallic Glasses: An Overview*; 2008; ISBN 9780387489209.

3.   Suryanarayana, C. Rapid Solidification Processing. *Encycl. Mater. Sci. Technol.* **2002**, 1–10, doi:10.1016/B0-08-043152-6/01831-3.

4.   Ye, Y.F.; Wang, Q.; Lu, J.; Liu, C.T.; Yang, Y. High-Entropy Alloy: Challenges and Prospects. *Mater. Today* **2016**, *19*, 349–362, doi:10.1016/j.mattod.2015.11.026.

5.   Inoue, A. Stabilization of Metallic Supercooled Liquid and Bulk Amorphous Alloys. *Acta Mater.* **2000**, *48*, 279–306, doi:10.1016/S1359-6454(99)00300-6.

6.   Zhang, M.; Wang, A.; Shen, B. Enhancement of Glass-Forming Ability of Fe-Based Bulk Metallic Glasses with High Saturation Magnetic Flux Density. *AIP Adv.* **2012**, *2*, doi:10.1063/1.4733340.

7.   Akihisa Inoue, Yoshiyuki Shinohara, J.S.G. Thermal and Magnetic Properties of Bulk Fe-Based Glassy Alloys Prepared by Copper Mold Casting. *Mater. Trans. JIM* **1995**, *36*, 1427–1433.

8.   Louzguine-Luzgin, D. V.; Chen, N.; Churymov, A.Y.; Louzguina-Luzgina, L. V.; Polkin, V.I.; Battezzati, L.; Yavari, A.R. Role of Different Factors in the Glass-Forming Ability of Binary Alloys. *J. Mater. Sci.* **2015**, *50*, 1783–1793, doi:10.1007/s10853-014-8741-y.

9.   Fulchiron, R.; Belyamani, I.; Otaigbe, J.U.; Bounor-Legaré, V. A Simple Method for Tuning the Glass Transition Process in Inorganic Phosphate Glasses. *Sci. Rep.* **2015**, *5*, doi:10.1038/srep08369.

10. Turnbull, D. Under What Conditions Can A Glass Be Formed? *Contemp. Phys.* **1969**, *10*, 473–488, doi:10.1080/00107516908204405.

11. Shao, G.; Lu, B.; Liu, Y.Q.; Tsakiropoulos, P. Glass Forming Ability of Multi-Component Metallic Systems. *Intermetallics* **2005**, *13*, 409–414, doi:10.1016/j.intermet.2004.07.030.

12. George, E.P.; Raabe, D.; Ritchie, R.O. High-Entropy Alloys. *Nat. Rev. Mater.* **2019**, *4*, 515–534, doi:10.1038/s41578-019-0121-4.

13. Zhang, Y.; Zhou, Y.J. Solid Solution Formation Criteria for High Entropy Alloys. *Mater. Sci. Forum* **2007**, *561–565*, 1337–1339, doi:10.4028/www.scientific.net/msf.561-565.1337.

14. Guo, S.; Liu, C.T. Phase Stability in High Entropy Alloys: Formation of Solid-Solution Phase or Amorphous Phase. *Prog. Nat. Sci. Mater. Int.* **2011**, *21*, 433–446, doi:10.1016/S1002-0071(12)60080-X.

15. Sheikh, S.; Mao, H.; Guo, S. Predicting Solid Solubility in CoCrFeNiMx (M = 4d Transition Metal) High-Entropy Alloys. *J. Appl. Phys.* **2017**, *121*, 1–8, doi:10.1063/1.4983762.

16. Liang, X.B.; Wei, M.; Cheng, J.B.; Zhang, W.; Xu, B.S. Reaserch Progress in Advanced Materials of High-Entropy Alloys. *Cailiao Gongcheng/Journal Mater. Eng.* **2009**, *12*, 75–79.

17. Sahlberg, M.; Karlsson, D.; Zlotea, C.; Jansson, U. Superior Hydrogen Storage in High Entropy Alloys. *Sci. Rep.* **2016**, *6*, 1–6, doi:10.1038/srep36770.

18. Liu, W.H.; Yang, T.; Liu, C.T. Precipitation Hardening in CoCrFeNi-Based High Entropy Alloys. *Mater. Chem. Phys.* **2018**, *210*, 2–11, doi:10.1016/j.matchemphys.2017.07.037.

19. Kolano-Burian, A.; Wlodarczyk, P.; Hawelek, L.; Kolano, R.; Polak, M.; Zackiewicz, P.; Temleitner, L. Impact of Cobalt Content on the Crystallization Pattern in the Finemet-Type Ribbons. *J. Alloys Compd.* **2014**, *615*, S203–S207, doi:10.1016/j.jallcom.2013.12.066.

20. He, J.Y.; Wang, H.; Wu, Y.; Liu, X.J.; Mao, H.H.; Nieh, T.G.; Lu, Z.P. Precipitation Behavior and Its Effects on Tensile Properties of FeCoNiCr High-Entropy Alloys. *Intermetallics* **2016**, *79*, 41–52, doi:10.1016/j.intermet.2016.09.005.

21. Ding, J.; Inoue, A.; Han, Y.; Kong, F.L.; Zhu, S.L.; Wang, Z.; Shalaan, E.; Al-Marzouki, F. High Entropy Effect on Structure and Properties of (Fe,Co,Ni,Cr)-B Amorphous Alloys. *J. Alloys Compd.* **2017**, *696*, 345–352, doi:10.1016/j.jallcom.2016.11.223.

22. Qi, T.; Li, Y.; Takeuchi, A.; Xie, G.; Miao, H.; Zhang, W. Soft Magnetic

Fe25Co25Ni25(B, Si)25 High Entropy Bulk Metallic Glasses. *Intermetallics* **2015**, *66*, 8–12, doi:10.1016/j.intermet.2015.06.015.

23. B. Cullity *Elements of X-Ray Diffraction*; 3rd ed.; 1967;

24. Nagaraj, S.K.; Shivanna, S.; Subramani, N.K. Revisiting Powder X-Ray Diffraction Technique : A Powerful Tool to Characterize Polymers and Their Composite Films. **2016**, *4*, 1–5, doi:10.4172/2321-6212.1000158.

25. Höhne G W Hemminger and H.-J Flammersheim *Differential Scanning Calorimetry : An Introduction for Practitioners*; Berlin: Springer-Verlag, 1996;

26. W. ZhouZ.L. Wang *Scanning Microscopy for Nanotechnology. Techniques and Applications*; 2007; ISBN 978-1-4419-2209-0.

27. Gütlich, P.; Link, R.; Trautwein, A. *Mössbauer Spectroscopy and Transition Metal Chemistry: Fundamentals and Applications*; 1978; Vol. 3; ISBN 9783540884279.

28. Brand, R. A., Lauer, J. and Herlach, D.M. No Title. *J. Phys. F Met. Phys* **1983**, *13*, 875.

29. Oliver, W.C.; Pharr, G.M. An Improved Technique for Determining Hardness and Elastic Modulus Using Load and Displacement Sensing Indentation Experiments. *J. Mater. Res.* **1992**, *7*, 1564–1583, doi:10.1557/jmr.1992.1564.

30. MariAnne Sullivan Measuring, Evaluating, and Describing Pile-Up and Sink-In During Nanoindentation of Thin Films on Substrates. *J. Chem. Inf. Model.* **2013**, *53*, 1689–1699.

31. Sullivan, M.A.; Prorok, B.C. Newly Discovered Pile up Effects during Nanoindentation. *Conf. Proc. Soc. Exp. Mech. Ser.* **2015**, *8*, 1–5, doi:10.1007/978-3-319-07004-9_1.

32. Zhang, L.; Name, P.; Hora, P.; Name, P.; Jang, J.; Name, P.; Kirkes, L.; Name, P.; Miller, C.; Name, P.; et al. Electrochemical Tests Under TP 06-02 Effective. **2021**, 1–10.

33. Poursaee, A. *Corrosion Sensing for Assessing and Monitoring Civil Infrastructures*; Woodhead Publishing Limited, 2014; Vol. 1; ISBN 9780857094322.

34. Kruger, J. The Oxide Films Formed on Copper Single Crystal Surfaces in Water. *J. Electrochem. Soc.* **1959**, *108*, 503, doi:10.1149/1.2428124.

35. Kong, K.H.; Kim, K.C.; Kim, W.T.; Kim, D.H. Microstructural Features of Multicomponent FeCoCrNiSi x Alloys . *Appl. Microsc.* **2015**, *45*, 32–36, doi:10.9729/am.2015.45.1.32.

36. Xing, Q.W.; Zhang, Y. Amorphous Phase Formation Rules in High-Entropy Alloys. *Chinese Phys. B* **2017**, *26*, doi:10.1088/1674-1056/26/1/018104.

37. Zhang, Y.; Zhou, Y.J.; Lin, J.P.; Chen, G.L.; Liaw, P.K. Solid-Solution Phase Formation Rules for Multi-Component Alloys. *Adv. Eng. Mater.* **2008**, *10*, 534–538, doi:10.1002/adem.200700240.

38. Załuska, A.; Matyja, H. Crystallization Characteristics of Amorphous Fe-Si-B Alloys. *J. Mater. Sci.* **1983**, *18*, 2163–2172, doi:10.1007/BF00555011.

39. Shpak, A.P.; Il'Inskii, A.G.; Marunyak, A. V.; Slukhovskyy, O.I.; Lepeeva, Y. V.; Dekhtyar, A.; Kaban, I.; Mattern, N.; Eckert, J. Crystallization of Fe82Si2B16 and Fe82Si4B14 Metallic Glasses upon Isothermal and Non-Isothermal Annealing. *EPJ Web Conf.* **2011**, *15*, 14–17, doi:10.1051/epjconf/20111501008.

40. Cheng, Y.T.; Cheng, C.M. Relationships between Hardness, Elastic Modulus, and the Work of Indentation. *Appl. Phys. Lett.* **1998**, *73*, 614–616, doi:10.1063/1.121873.

41. Pellicer, E.; Pané, S.; Sivaraman, K.M.; Ergeneman, O.; Suriñach, S.; Baró, M.D.; Nelson, B.J.; Sort, J. Effects of the Anion in Glycine-Containing Electrolytes on the Mechanical Properties of Electrodeposited Co-Ni Films. *Mater. Chem. Phys.* **2011**, *130*, 1380–1386, doi:10.1016/j.matchemphys.2011.09.032.

42. Wang, X.F.; Yang, X.P.; Guo, Z.D.; Zhou, Y.C.; Song, H.W. Nanoindentation Characterization of Mechanical Properties of Ferrite and Austenite in Duplex Stainless Steel. *Adv. Mater. Res.* **2007**, *26–28*, 1165–1170, doi:10.4028/www.scientific.net/amr.26-28.1165.

43. Guo, W.; Choi, P.P.; Seol, J.B. Amorphous Phase Separation in an Fe-Based Bulk Metallic Glass. *Mater. Lett.* **2017**, *190*, 161–164, doi:10.1016/j.matlet.2017.01.012.

44. Szlufarska, I.; Kalia, R.K.; Nakano, A.; Vashishta, P. Atomistic Mechanisms of Amorphization during Nanoindentation of SiC: A Molecular Dynamics Study. *Phys. Rev. B - Condens. Matter Mater. Phys.* **2005**, *71*, 1–11, doi:10.1103/PhysRevB.71.174113.

45. Sinha, S.; Mirshams, R.A.; Wang, T.; Nene, S.S.; Frank, M.; Liu, K.; Mishra, R.S. Nanoindentation Behavior of High Entropy Alloys with Transformation-Induced Plasticity. *Sci. Rep.* **2019**, *9*, 1–11, doi:10.1038/s41598-019-43174-x.

46.   Sun, Y.; Chen, P.; Liu, L.; Yan, M.; Wu, X.; Yu, C.; Liu, Z. Local Mechanical Properties of AlxCoCrCuFeNi High Entropy Alloy Characterized Using Nanoindentation. *Intermetallics* **2018**, *93*, 85–88, doi:10.1016/j.intermet.2017.11.010.

47.   Duan, F.H.; Pan, J.; Lin, Y.; Li, Y. Significant Structural Relaxation in a Mo[Sbnd]O Binary Amorphous Alloy. *J. Non. Cryst. Solids* **2019**, *514*, 10–14, doi:10.1016/j.jnoncrysol.2019.03.038.

48.   Gludovatz, B.; George, E.P.; Ritchie, R.O. Processing, Microstructure and Mechanical Properties of the CrMnFeCoNi High-Entropy Alloy. *Jom* **2015**, *67*, 2262–2270, doi:10.1007/s11837-015-1589-z.

49.   Leitner, A.; Maier-Kiener, V.; Kiener, D. Extraction of Flow Behavior and Hall–Petch Parameters Using a Nanoindentation Multiple Sharp Tip Approach. *Adv. Eng. Mater.* **2017**, *19*, 1–9, doi:10.1002/adem.201600669.

50.   Attaf, M.T. Connection between the Loading Curve Models in Elastoplastic Indentation. *Mater. Lett.* **2004**, *58*, 3491–3498, doi:10.1016/j.matlet.2004.06.049.

51.   Duan, F.H.; Pan, J.; Lin, Y.; Li, Y. Significant Structural Relaxation in a Mo[Sbnd]O Binary Amorphous Alloy. *J. Non. Cryst. Solids* **2019**, *514*, 10–14, doi:10.1016/j.jnoncrysol.2019.03.038.

52.   Aliaga, L.C.R.; Beringues, J.F.; Suriñach, S.; Baró, M.D.; Kiminami, C.S.; Bolfarini, C.; Botta, W.J.; Viñas, J.S. Comparative Study of Nanoindentation on Melt-Spun Ribbon and Bulk Metallic Glass with Ni60Nb37B3 Composition. *J. Mater. Res.* **2013**, *28*, 2740–2746, doi:10.1557/jmr.2013.260.

53.   Zhang, L.S. Preparation of CoCrFeNiCuMnSix High Entropy Alloys and Their Microstructure and Properties. *Adv. Mater. Res.* **2013**, *750–752*, 615–618, doi:10.4028/www.scientific.net/AMR.750-752.615.

54.   Zhang, Z. Elastic Properties of Bulk-Metallic Glasses Studied by Resonant Ultrasound Spectroscopy. **2008**.

55.   Fauth, F.; Peral, I.; Popescu, C.; Knapp, M. The New Material Science Powder Diffraction Beamline at ALBA Synchrotron. *Powder Diffr.* **2013**, *28*, 360–370.

56.   Schneider, C.A.; Rasband, W.S.; Eliceiri, K.W. NIH Image to ImageJ: 25 Years of Image Analysis. *Nat. Methods* **2012**, *9*, 671–675, doi:10.1038/nmeth.2089.

57. Zhang, H.; Zhong, X.C.; He, Y.Z.; Li, W.H.; Wu, W.F.; Chen, G.; Guo, S. Effect of High Configuration Entropy and Rare Earth Addition on Boride Precipitation and Mechanical Properties of Multi-Principal-Element Alloys. *J. Mater. Eng. Perform.* **2017**, *26*, 3750–3755, doi:10.1007/s11665-017-2831-3.

58. Leyland, A.; Matthews, A. On the Significance of the H/E Ratio in Wear Control: A Nanocomposite Coating Approach to Optimised Tribological Behaviour. *Wear* **2000**, *246*, 1–11, doi:10.1016/S0043-1648(00)00488-9.

59. Fallis, A.. Measuring, Evaluating, and Describing Pile-Up and Sink-In During Nanoindentation of Thin Films on Substrates. *J. Chem. Inf. Model.* **2013**, *53*, 1689–1699.

60. Mirshams, R.A.; Srivastava, A.K. Effect of Pile-up on Nanoindentation Measurements of Polycrystalline Bulk Metals. *Adv. Mater. Res.* **2014**, *853*, 143–150, doi:10.4028/www.scientific.net/AMR.853.143.

61. Beegan, D.; Chowdhury, S.; Laugier, M.T. The Nanoindentation Behaviour of Hard and Soft Films on Silicon Substrates. *Thin Solid Films* **2004**, *466*, 167–174, doi:10.1016/j.tsf.2004.03.006.

62. Burik, P.; Pešek, L.; Voleský, L. Effect of Pile-up on the Mechanical Characteristics of Steel with Different Strain History by Depth Sensing Indentation. *Met. 2014 - 23rd Int. Conf. Metall. Mater. Conf. Proc.* **2014**, *2*, 629–633.

63. Oliver, W.C.; Pharr, G.M. Measurement of Hardness and Elastic Modulus by Instrumented Indentation: Advances in Understanding and Refinements to Methodology. *J. Mater. Res.* **2004**, *19*, 3–20, doi:10.1557/jmr.2004.19.1.3.

64. Koch, G.H.; Brongers, M.P.H.; Thompson, N.G.; Virmani, Y.P.; Payer, J.. Corrosion Cost and Preventive Strategies in the United State. *Natl. Tech. Inf. Serv. Rep. No. FHWA-RD-01-156* **2001**.

65. H.H.Liebermann(ed.) *Rapidly Solidified Alloys Processes-Structures-Properties-Applications*; Marcel Dekker, New York, NY, 1993; ISBN 9780824789510.

66. Wang, S. Corrosion Resistance and Electrocatalytic Properties of Metallic Glasses. *Met. Glas. - Form. Prop.* **2016**, doi:10.5772/63677.

67. Brien, V.; Khare, V.; Herbst, F.; Weisbecker, P.; Ledeuil, J.B.; de Weerd, M.C.; Machizaud, F.; Dubois, J.M. Influence of Boron Content on the Microstructure of

Sintered Al62.5-XCu25.3Fe12.2Bx Alloys (x = 0, 3, 5). *J. Mater. Res.* 2004, *19*, 2974–2980.

68. Zhang, J.S.; Xue, Y.J.; Guo, Y.J.; Xu, C.X.; Liang, W. Effect of Si on As-Cast Microstructure in Quasicrystalline Al-Cu -Fe Alloy. *Mater. Sci. Forum* **2007**, *546–549*, 619–622, doi:10.4028/www.scientific.net/msf.546-549.619.

69. Dutta, R.S.; Dey, G.K. Effects of Partial Crystallinity and Quenched-in Defects on Corrosion of a Rapidly Solidified Ti-Cu Alloy. *Bull. Mater. Sci.* **2003**, *26*, 477–482, doi:10.1007/BF02707344.

70. Jayaraj, J.; Kim, Y.C.; Kim, K.B.; Seok, H.K.; Fleury, E. Corrosion Studies on Fe-Based Amorphous Alloys in Simulated PEM Fuel Cell Environment. *Sci. Technol. Adv. Mater.* **2005**, *6*, 282–289, doi:10.1016/j.stam.2005.02.019.

71. Zander, D.; Heisterkamp, B.; Gallino, I. Corrosion Resistance of Cu-Zr-Al-Y and Zr-Cu-Ni-Al-Nb Bulk Metallic Glasses. *J. Alloys Compd.* **2007**, *434–435*, 234–236, doi:10.1016/j.jallcom.2006.08.112.

72. Raicheff, R.; Zaprianova, V. EFFECT OF COBALT AND NICKEL ALLOYING ON CORROSION BEHAVIOUR OF AMORPHOUS Fe-B-Si ALLOYS. *J. Univ. Chem. Technol. Metall.* **2009**, *44*, 61–65.

73. Qin, C.; Zhang, W.; Asami, K.; Ohtsu, N.; Inoue, A. Glass Formation, Corrosion Behavior and Mechanical Properties of Bulk Glassy Cu–Hf–Ti–Nb Alloys. *Acta Mater.* **2005**, *53*, 3903–3911, doi:10.1016/j.actamat.2005.04.037.

74. Li, M.; Chen, Q.; Cui, X.; Peng, X.; Huang, G. Evaluation of Corrosion Resistance of the Single-Phase Light Refractory High Entropy Alloy TiCrVNb0.5Al0.5 in Chloride Environment. *J. Alloys Compd.* **2021**, *857*, doi:10.1016/j.jallcom.2020.158278.

75. Pang, S.J.; Zhang, T.; Asami, K.; Inoue, A. Synthesis of Fe-Cr-Mo-C-B-P Bulk Metallic Glasses with High Corrosion Resistance. *Acta Mater.* **2002**, *50*, doi:10.1016/S1359-6454(01)00366-4.

76. Shang, X.L.; Wang, Z.J.; Wu, Q.F.; Wang, J.C.; Li, J.J.; Yu, J.K. Effect of Mo Addition on Corrosion Behavior of High-Entropy Alloys CoCrFeNiMo x in Aqueous Environments. *Acta Metall. Sin. (English Lett.* **2019**, *32*, 41–51, doi:10.1007/s40195-018-0812-7.

87

77. Bijalwan, P.; Kumar, A.; Nayak, S.K.; Banerjee, A.; Dutta, M.; Laha, T. Microstructure and Corrosion Behavior of Fe-Based Amorphous Composite Coatings Developed by Atmospheric Plasma Spraying. *J. Alloys Compd.* **2019**, *796*, doi:10.1016/j.jallcom.2019.05.046.

78. Guo, W.; Liu, B. Microstructure and Corrosion Behavior of Laser Cladding FeCoNiCrBSi Based High-Entropy Alloy Coatings. *Coatings* **2022**, *12*, 1–18.

79. Huang, F.; Kang, J. jie; Yue, W.; Fu, Z. qiang; Zhu, L. na; She, D. shun; Liang, J.; Wang, C. biao Corrosion Behavior of FeCrMoCBY Amorphous Coating Fabricated by High-Velocity Air Fuel Spraying. *J. Therm. Spray Technol.* **2019**, *28*, 842–850, doi:10.1007/s11666-019-00843-7.

80. Cui, P.; Bao, Z.; Liu, Y.; Zhou, F.; Lai, Z.; Zhou, Y.; Zhu, J. Corrosion Behavior and Mechanism of Dual Phase Fe1.125Ni1.06CrAl High Entropy Alloy. *Corros. Sci.* **2022**, *201*, 110276, doi:10.1016/j.corsci.2022.110276.

81. Li, Y.; Wang, S.; Wang, X.; Yin, M.; Zhang, W. New FeNiCrMo(P, C, B) High-Entropy Bulk Metallic Glasses with Unusual Thermal Stability and Corrosion Resistance. *J. Mater. Sci. Technol.* **2020**, *43*, 32–39, doi:10.1016/j.jmst.2020.01.020.

82. Gong, P.; Wang, D.; Zhang, C.; Wang, Y.; Jamili-Shirvan, Z.; Yao, K.; Wang, X. Corrosion Behavior of TiZrHfBeCu(Ni) High-Entropy Bulk Metallic Glasses in 3.5 Wt. % NaCl. *npj Mater. Degrad.* **2022**, *6*, 1–14, doi:10.1038/s41529-022-00287-5.

83. Takeuchi, A.; Amiya, K.; Wada, T.; Yubuta, K.; Zhang, W.; Makino, A. Entropies in Alloy Design for High-Entropy and Bulk Glassy Alloys. *Entropy* **2013**, *15*, doi:10.3390/e15093810.

84. Panahi, S.L.; Garcia-Ramón, M.; Pineda, E.; Bruna, P. New (FeCoCrNi)-(B,Si) High-Entropy Metallic Glasses, Study of the Crystallization Processes by X-Ray Diffraction and Mössbauer Spectroscopy. *J. Non. Cryst. Solids* **2020**, *547*, 120301, doi:10.1016/J.JNONCRYSOL.2020.120301.

85. Kumar, N.; Fusco, M.; Komarasamy, M.; Mishra, R.S.; Bourham, M.; Murty, K.L. Understanding Effect of 3.5 Wt.% NaCl on the Corrosion of Al0.1CoCrFeNi High-Entropy Alloy. *J. Nucl. Mater.* **2017**, *495*, 154–163, doi:10.1016/j.jnucmat.2017.08.015.

86. Córdoba-Torres, P. Relationship between Constant-Phase Element (CPE) Parameters

and Physical Properties of Films with a Distributed Resistivity. *Electrochim. Acta* **2017**, *225*, doi:10.1016/j.electacta.2016.12.087.

87. Ulum, M.F.; Caesarendra, W.; Alavi, R.; Hermawan, H. In-Vivo Corrosion Characterization and Assessment of Absorbable Metal Implants. *Coatings* 2019, *9*.

88. Sun, Y.P.; Wang, Z.; Yang, H.J.; Lan, A.D.; Qiao, J.W. Effects of the Element La on the Corrosion Properties of CrMnFeNi High Entropy Alloys. *J. Alloys Compd.* **2020**, *842*, doi:10.1016/j.jallcom.2020.155825.

89. Bar-Cohen, Y. *High Temperature Materials and Mechanisms*; CRC Press, Boca Raton, 2017; ISBN 9781466566460.

90. Beke, D.L.; Erdélyi, G. On the Diffusion in High-Entropy Alloys. *Mater. Lett.* **2016**, *164*, doi:10.1016/j.matlet.2015.09.028.

91. Bredar, A.R.C.; Chown, A.L.; Burton, A.R.; Farnum, B.H. Electrochemical Impedance Spectroscopy of Metal Oxide Electrodes for Energy Applications. *ACS Appl. Energy Mater.* 2020, *3*.

92. Qiu, Y.; Thomas, S.; Gibson, M.A.; Fraser, H.L.; Pohl, K.; Birbilis, N. Microstructure and Corrosion Properties of the Low-Density Single-Phase Compositionally Complex Alloy AlTiVCr. *Corros. Sci.* **2018**, *133*, doi:10.1016/j.corsci.2018.01.035.

93. Qiu, Y.; Thomas, S.; Fabijanic, D.; Barlow, A.J.; Fraser, H.L.; Birbilis, N. Microstructural Evolution, Electrochemical and Corrosion Properties of Al x CoCrFeNiTi y High Entropy Alloys. *Mater. Des.* **2019**, *170*, doi:10.1016/j.matdes.2019.107698.

94. Koga, G.Y.; Otani, L.B.; Silva, A.M.B.; Roche, V.; Nogueira, R.P.; Jorge, A.M.; Bolfarini, C.; Kiminami, C.S.; Botta, W.J. Materials Characterization and Corrosion Resistance of Boron-Containing-Austenitic Stainless Steels Produced by Rapid Solidification Techniques., doi:10.3390/ma11112189.

95. Masumoto, T.; Hashimoto, K.; Masumoto, T.; Corrosion, K.H.; Of, P.; Metals, A. CORROSION PROPERTIES OF AMORPHOUS METALS To Cite This Version : HAL Id : Jpa-00220328. **1980**.

96. Muangtong, P.; Rodchanarowan, A.; Chaysuwan, D.; Chanlek, N.; Goodall, R. The Corrosion Behaviour of CoCrFeNi-x (X = Cu, Al, Sn) High Entropy Alloy Systems in

Chloride Solution. *Corros. Sci.* **2020**, *172*, doi:10.1016/j.corsci.2020.108740.

97.   Shi, Y.; Yang, B.; Liaw, P.K. Corrosion-Resistant High-Entropy Alloys: A Review. *Metals (Basel).* 2017, *7*.

98.   Hsu, Y.J.; Chiang, W.C.; Wu, J.K. Corrosion Behavior of FeCoNiCrCux High-Entropy Alloys in 3.5% Sodium Chloride Solution. *Mater. Chem. Phys.* **2005**, *92*, doi:10.1016/j.matchemphys.2005.01.001.